NASA CR-72954
DDAD EDR 7034

FINAL REPORT
EXPERIMENTAL EVALUATION OF LOW CYCLE THERMAL FATIGUE IN A TURBINE VANE FABRICATED FROM LAMINATED POROUS MATERIAL

by

D. A. Nealy, R. D. Anderson, and A. A. Hufford

DETROIT DIESEL ALLISON DIVISION OF GENERAL MOTORS
Post Office Box 894
Indianapolis, Indiana 46206

prepared for

NATIONAL AERONAUTICS AND SPACE ADMINISTRATION

15 March 1971

CONTRACT NAS3-12431

NASA Lewis Research Center
Cleveland, Ohio
Edward Warren, Project Manager
Robert Hickel, Research Advisor
Airbreathing Engines Division

FOREWORD

The work described herein was conducted by the Detroit Diesel Allison Division (DDAD) of General Motors under NASA Contract NAS3-12431. The work was done under the management of the NASA Project Manager, Mr. Edward L. Warren, Air-breathing Engines Division, NASA-Lewis Research Center. Dr. D. A. Nealy was the DDAD Technical Director and Mr. J. L. Dillard was the DDAD Program Manager.

The authors wish to acknowledge the contributions of Messrs J. L. Pontius and K. Muszar of the DDAD Materials Engineering Development Laboratory to the posttest metallurgical evaluation. The authors are also indebted to Mr. R. E. Chupp of the DDAD Heat Transfer Section for his able assistance in the performance of the transient thermal response analysis.

ABSTRACT

The results of an experimental evaluation of low cycle thermal fatigue in laminated porous wall turbine vanes are presented. Details of the laminated porous wall vane design are given together with a description of the cascade test facility and associated instrumentation. Three test vanes were exposed to rapid cyclic gas temperature variations over a range from 1150°F (621°C) to 2800°F (1538°C). After 110 cycles of operation, transverse (chordwise) cracks were observed in the leading edge region of all three test vanes. Subsequent metallographic and structural analyses indicated the primary failure mechanism to be low cycle thermal fatigue. Agreement between predicted and observed fatigue life was very good.

TABLE OF CONTENTS

LIST OF ILLUSTRATIONS

LIST OF TABLES

I. SUMMARY

An experimental and analytical evaluation of low cycle thermal fatigue in a variable permeability porous-wall turbine vane was made for operating conditions representative of high temperature turbine engine operation. The vanes were fabricated from a Lamilloy® laminated porous wall structure (Hastelloy X) which was bonded to internal reinforcing sheets to provide structural rigidity. The composite bonded assembly was formed into the desired airfoil shape and welded at the trailing edge to provide a hollow, self-supporting airfoil shell.

Three test vanes were experimentally evaluated in a five-blade cascade facility which was designed to provide rapid cyclic operation between gas temperature levels of approximately 1150°F (621°C) and 2800°F (1538°C). Testing was carried out at a nominal gas pressure level of 140 psia (96.5 N/cm^2), and cooling air was supplied to the test vanes at temperatures ranging from 500°F (259°C) to 900°F (482°C). Surface temperature distributions over the three test vanes were determined with thermocouples, infrared film, and pyrometric measurement techniques. The measurements indicated that during a typical cycle, local airfoil skin temperatures varied from approximately 1700°F (927°C) to 700°F (371°C). After 110 cycles of operation, transverse chordwise surface cracks were observed on the leading edges of all three test vanes, and the vanes were removed from the cascade facility for further analysis.

Posttest metallographic analysis of the test vanes revealed that the primary failure mechanism was low cycle thermal fatigue. A detailed thermal/structural analysis of a typical vane indicated that severe transient excursions in chordwise metal temperature distribution occurred during each cycle. The metal temperature excursions, in turn, produced severe longitudinal strain reversals (compressive to tensile and vice versa) in the leading-edge region. The calculated strain range was found to be large enough to initiate low cycle fatigue (transverse cracks) after approximately 140 cycles of operation, based on the life prediction techniques employed. The structural analysis also indicated that transverse strains were less than 25% of the corresponding longitudinal values because of the much greater airfoil flexibility in the transverse direction (bending about a longitudinal axis).

The relatively good agreement between predicted and observed failure provided a basis for several design recommendations including:

- Redesign of the leading- and trailing-edge regions of the airfoil to reduce chordwise surface temperature gradients

- Reduction in the extent and thickness of side-wall stiffening sheets to reduce thermal inertia and load transfer to the leading edge
- Use of hot creep airfoil forming techniques to eliminate residual stresses and/or surface cracks attributable to the forming operation.

II. INTRODUCTION

While transpiration cooling potentially represents the most thermodynamically efficient approach to turbine cooling, practical implementation of the method has been hampered by the limitations of porous materials. In general, conventional porous-wall structures have not compared favorably with solid-wall (cast) structures in terms of strength or oxidation resistance. Considerable difficulty in predicting or controlling local permeability (flow resistance) has also been encountered, and susceptibility to foreign particle clogging continues to be a problem.

Advances in metal joining techniques over the past five years have led to the development of a multiple-laminate porous structure fabricated from several diffusion-bonded, photoetched metal sheets (Figure 1). This porous material (Lamilloy) shows considerable promise relative to application in the high-temperature turbine environment.

Evaluation to date has revealed that Lamilloy porous material exhibits strength and oxidation characteristics which appear superior to those of other types of porous materials previously used in aircraft gas turbines. Evaluation has also revealed that local permeability can be controlled in a predictable manner. The strength, oxidation, and permeability characteristics of Lamilloy porous material were previously evaluated under Tasks I and II of NASA Contract NAS3-7913.[1] * Heat transfer characteristics of the material were independently investigated in two parallel programs supported by the Air Force.[2,3] More recently, Lamilloy airfoils were designed, fabricated, and evaluated in a high-temperature cascade facility.[4] This program, which was also supported by NASA Contract NAS3-7913, involved:

- The thermal and structural design analysis of a noncompartmented, variable permeability turbine vane featuring a laminated porous shell
- The fabrication and experimental (hot cascade) evaluation of several vanes based on the established design
- Comparison of experimental results with predicted thermal and structural behavior

The laminated porous wall structure used in the latter program revealed no evidence of structural distress, clogging, or oxidation after approximately 88 hr of cascade testing at gas temperatures ranging from 2000 to 3000°F (1093 to 1693°C). In general, the experimentally measured steady-state airfoil surface temperature distributions compared favorably with the predicted values when realistic corrections were made to the indicated gas stream and surface temperature measurements.

The work reported herein represents an extension of the previous program[4] to include a careful examination of the tolerance of the airfoil design to low cycle thermal fatigue. To investigate

*Superscript numbers correspond to the references listed at the end of this report.

this phenomenon, which is felt to be related to the transient thermal response of the airfoil, three airfoils of the same design tested previously were exposed to rapid gas stream temperature excursions in a high-temperature cascade facility. The vane testing was conducted in a five-blade cascade facility which was specially adapted for rapid cyclic operation between gas temperature levels of approximately 1150°F (621°C) and 2800°F (1538°C). Cooling air was supplied to the test vanes at temperatures ranging from 500 to 900°F (259 to 482°C). Surface temperature distributions over the three test vanes were determined by using thermocouples, infrared film, and pyrometric measurement techniques.

The following sections contain detailed descriptions of the vane design, experimental apparatus, test program, and test results, followed by an overview of the program accomplishments and recommendations for future work.

III. GENERAL DESCRIPTION OF VANE DESIGN

The turbine vanes evaluated in this program were essentially identical in design with those previously evaluated.[4] The general arrangement of the vane is shown in Figures 2 and 3. The airfoil coordinates are defined in Figure 4, Table I, and Reference 5. The design is essentially a noncompartmented, variable-permeability Lamilloy shell with end attachments. The porous skin—0.030 in. (0.076 cm) thick—is reinforced by several diffusion-bonded stiffening sheets to provide structural rigidity. Oversize holes are photoetched in the stiffening sheets to connect the airfoil interior (coolant supply plenum) and the various inside surface sheet holes of the laminated porous skin structure. The composite wall structure is first fabricated (bonded) in flat sheet form and then cold formed into airfoil shape. After forming, the trailing edge region of each side wall is joined by welding.

End attachments are provided to facilitate cooling air delivery and assembly of the vanes into the cascade facility. Cooling air is delivered through the tip end fitting which is welded to the airfoil shell and also serves to define the outer flow-path wall. The end fitting at the airfoil hub serves to align the airfoils in the cascade facility and to define the inner flow-path wall. The latter is slip fit over the airfoil shell to allow thermal expansion during cascade operation. The complete vane assembly is shown in Figures 5 and 6. Because of a minor end-wall overheating problem which occurred during the previous test program,[4] the tip end fittings were slightly modified to provide more effective cooling of the tip end wall. This was accomplished very simply by increasing the width of the coolant inlet chamber so that the entire back face of the tip end fitting was exposed to incoming coolant (Figure 7). In addition, the gas side surfaces of both end fittings were flame sprayed with a zirconium oxide coating to protect the end attachments from gas erosion. Figure 8 is a photograph taken of a typical vane assembly after application of the coating.

The various constant-permeability regions of the airfoil are shown schematically in the unfolded view of Figure 9. The nominal geometric characteristics of the Lamilloy structure in these regions are given in Table II. Note that these turbine vanes were not designed to accommodate the specific cascade test conditions of the present program. The particular geometric configurations shown were chosen to satisfy the original design conditions specified by NASA.[6] Specifically, the airfoils were designed to provide an isothermal skin temperature of 1600°F (871°C) subject to the following:

- An average gas temperature of 2500°F (1371°C)
- A coolant supply temperature of 1200°F (649°C)
- A gas stream inlet total pressure of 114 psia (78.6 N/cm^2)
- An external aerodynamic environment as defined in Reference 5

TABLE I. AIRFOIL COORDINATES.

Hub Section (G-G) (See Figure 4 for coordinate system definition)							
Suction surface				Pressure surface			
$\overline{X}$ (in.)	$\overline{X}$ (cm)	$\overline{Y}$ (in.)	$\overline{Y}$ (cm)	$\overline{X}$ (in.)	$\overline{X}$ (cm)	$\overline{Y}$ (in.)	$\overline{Y}$ (cm)
0.085	0.216	3.135	7.963	0.104	0.266	2.856	7.256
0.223	0.566	3.189	8.101	0.181	0.459	2.837	7.207
0.330	0.840	3.210	8.154	0.254	0.645	2.815	7.150
0.422	1.072	3.214	8.163	0.325	0.826	2.790	7.087
0.503	1.279	3.206	8.144	0.394	1.000	2.762	7.017
0.576	1.463	3.188	8.100	0.460	1.169	2.732	6.940
0.642	1.630	3.164	8.038	0.524	1.331	2.700	6.857
0.703	1.787	3.135	7.963	0.585	1.488	2.664	6.768
0.759	1.928	3.099	7.872	0.645	1.639	2.627	6.673
0.812	2.064	3.061	7.776	0.703	1.787	2.588	6.574
0.861	2.188	3.018	7.666	0.759	1.928	2.546	6.468
0.908	2.307	2.972	7.550	0.812	2.064	2.502	6.355
0.952	2.419	2.924	7.428	0.863	2.194	2.455	6.237
0.994	2.524	2.873	7.298	0.913	2.319	2.407	6.114
1.033	2.624	2.819	7.161	0.962	2.443	2.358	5.989
1.071	2.720	2.764	7.021	1.009	2.563	2.306	5.859
1.123	2.854	2.685	6.821	1.054	2.677	2.253	5.723
1.174	2.982	2.604	6.615	1.097	2.788	2.198	5.583
1.222	3.104	2.520	6.403	1.139	2.893	2.141	5.438
1.269	3.223	2.435	6.186	1.180	2.998	2.083	5.292
1.313	3.336	2.348	5.964	1.221	3.101	2.025	5.144
1.356	3.444	2.258	5.736	1.260	3.202	1.965	4.993
1.394	3.541	2.167	5.504	1.300	3.302	1.906	4.842
1.435	3.645	2.073	5.265	1.339	3.401	1.846	4.690
1.472	3.738	1.976	5.020	1.377	3.498	1.785	4.535
1.506	3.826	1.878	4.770	1.415	3.594	1.724	4.379
1.537	3.905	1.775	4.510	1.452	3.689	1.662	4.223
1.567	3.980	1.672	4.246	1.489	3.783	1.600	4.066
1.591	4.043	1.562	3.969	1.527	3.879	1.539	3.910

TABLE I (continued).

Mean Section (C-C)							
Suction surface				Pressure surface			
$\bar{X}$ (in.)	$\bar{X}$ (cm)	$\bar{Y}$ (in.)	$\bar{Y}$ (cm)	$\bar{X}$ (in.)	$\bar{X}$ (cm)	$\bar{Y}$ (in.)	$\bar{Y}$ (cm)
0.078	0.199	3.131	7.955	0.124	0.316	2.852	7.244
0.229	0.581	3.202	8.135	0.203	0.517	2.834	7.199
0.345	0.876	3.233	8.213	0.279	0.709	2.812	7.144
0.441	1.120	3.242	8.234	0.352	0.895	2.788	7.083
0.525	1.334	3.235	8.219	0.422	1.074	2.761	7.013
0.601	1.526	3.220	8.181	0.490	1.244	2.730	6.934
0.669	1.701	3.197	8.122	0.555	1.410	2.696	6.848
0.733	1.864	3.168	8.049	0.617	1.569	2.659	6.755
0.791	2.010	3.132	7.957	0.677	1.720	2.620	6.655
0.845	2.147	3.092	7.855	0.735	1.868	2.578	6.549
0.895	2.275	3.048	7.742	0.792	2.013	2.535	6.439
0.942	2.394	2.999	7.619	0.847	2.152	2.489	6.323
0.986	2.506	2.948	7.488	0.900	2.286	2.441	6.202
1.029	2.614	2.894	7.352	0.951	2.417	2.392	6.077
1.069	2.717	2.838	7.210	1.001	2.544	2.342	5.948
1.108	2.816	2.781	7.063	1.050	2.668	2.289	5.816
1.162	2.951	2.697	6.852	1.098	2.789	2.235	5.678
1.214	3.085	2.614	6.640	1.144	2.907	2.180	5.539
1.265	3.214	2.528	6.422	1.190	3.024	2.125	5.398
1.315	3.341	2.441	6.200	1.235	3.137	2.067	5.252
1.361	3.459	2.350	5.970	1.278	3.247	2.009	5.103
1.407	3.575	2.258	5.737	1.322	3.358	1.950	4.955
1.451	3.686	2.164	5.498	1.365	3.468	1.892	4.806
1.494	3.796	2.070	5.257	1.407	3.575	1.832	4.654
1.534	3.897	1.971	5.008	1.449	3.681	1.771	4.500
1.573	3.995	1.871	4.754	1.490	3.786	1.711	4.346
1.610	4.089	1.770	4.496	1.532	3.891	1.650	4.190
1.645	4.178	1.665	4.231	1.572	3.995	1.588	4.034
1.676	4.257	1.557	3.955	1.613	4.097	1.529	3.884

TABLE I (concluded).

Tip Section (F-F)							
Suction surface				Pressure surface			
$\overline{X}$ (in.)	$\overline{X}$ (cm)	$\overline{Y}$ (in.)	$\overline{Y}$ (cm)	$\overline{X}$ (in.)	$\overline{X}$ (cm)	$\overline{Y}$ (in.)	$\overline{Y}$ (cm)
0.064	0.163	3.123	7.932	0.127	0.323	2.851	7.243
0.241	0.613	3.228	8.200	0.210	0.535	2.837	7.206
0.361	0.917	3.264	8.291	0.289	0.736	2.817	7.156
0.461	1.171	3.276	8.322	0.366	0.930	2.794	7.098
0.545	1.385	3.269	8.305	0.438	1.114	2.766	7.027
0.622	1.579	3.253	8.264	0.509	1.294	2.737	6.952
0.691	1.755	3.228	8.200	0.578	1.468	2.704	6.870
0.753	1.914	3.195	8.117	0.643	1.634	2.668	6.777
0.812	2.064	3.159	8.024	0.705	1.792	2.628	6.676
0.866	2.200	3.115	7.912	0.766	1.948	2.587	6.571
0.916	2.326	3.066	7.789	0.826	2.098	2.543	6.460
0.963	2.446	3.015	7.659	0.882	2.242	2.496	6.341
1.007	2.559	2.960	7.520	0.938	2.383	2.448	6.219
1.049	2.666	2.903	7.374	0.991	2.519	2.398	6.091
1.091	2.772	2.845	7.227	1.044	2.653	2.347	5.961
1.133	2.877	2.787	7.079	1.096	2.784	2.293	5.826
1.189	3.020	2.702	6.863	1.145	2.910	2.238	5.686
1.244	3.162	2.616	6.645	1.194	3.034	2.182	5.543
1.300	3.303	2.530	6.428	1.242	3.155	2.124	5.396
1.352	3.436	2.441	6.200	1.288	3.273	2.065	5.247
1.404	3.566	2.350	5.969	1.334	3.389	2.005	5.094
1.453	3.692	2.257	5.733	1.380	3.506	1.946	4.943
1.502	3.815	2.163	5.494	1.426	3.623	1.886	4.791
1.548	3.934	2.066	5.249	1.472	3.739	1.826	4.640
1.593	4.047	1.967	4.998	1.517	3.853	1.765	4.484
1.637	4.158	1.867	4.744	1.561	3.966	1.704	4.329
1.679	4.266	1.766	4.486	1.606	4.081	1.643	4.175
1.720	4.369	1.662	4.222	1.652	4.196	1.583	4.022
1.758	4.466	1.555	3.951	1.697	4.311	1.523	3.868

TABLE II. DESIGN PROPERTIES OF LAMILLOY POROUS MATERIAL CONFIGURATION USED.

Configuration A at suction surface trailing edge and on pressure surface Configuration B on remainder of suction surface Configuration C at leading edge			
Property *	Configuration A	Configuration B	Configuration C
α, $in.^{-2}(cm^{-2})$	2.067×10^8 (0.3204×10^8)	5.98×10^7 (0.9269×10^7)	3.00×10^7 (0.4650×10^7)
β, $in.^{-1}(cm^{-1})$	1.079×10^6 (0.4248×10^6)	7.24×10^5 (2.85×10^5)	8.67×10^4 (3.413×10^4)
τ_o, in. (cm)	0.0295 (0.07493)	0.0245 (0.0622)	0.0245 (0.0622)
τ, in. (cm)	0.0275 (0.06985)	0.0275 (0.06985)	0.0275 (0.06985)
P	0.22	0.205	0.205
e, in. (cm)	0.004 (0.0102)	0.004 (0.0102)	0.004 (0.0102)
s, in. (cm)	0.096 (0.244)	0.096 (0.244)	0.068 (0.173)
d_i, in. (cm)	0.0145 (0.0368)	0.023 (0.0584)	0.023 (0.0584)
Z', $in.^{-1}$ (cm^{-1})	110 (43.31)	106 (41.73)	110 (43.31)
Number of laminates	3	3	3
Grid spacing (in.) (cm)	0.24 (0.610)	0.24 (0.610)	0.24 (0.610)

*Symbols are defined in List of Symbols, pp 46-47.

The subsequent decision to investigate thermal response behavior—coupled with certain test rig limitations—led to differences between the original design conditions and the actual cascade operating conditions.

All portions of the vane and end fittings are manufactured from Hastelloy X. The original design metal temperature of 1600°F (871°C) was selected on the basis of providing an acceptable oxidation life, reflecting the results of previous oxidation resistance studies.[1]

IV. EXPERIMENTAL APPARATUS

POROUS WALL PERMEABILITY TEST EQUIPMENT

Local permeability measurements were made with the test equipment shown in Figure 10. The transducer component of the flowmeter system is positioned as near the airfoil as practical. Air exiting from a small group of holes—usually four holes—passes through a short length of soft, plastic hose pressed against the vane. The air then passes through the transducer with little or no pressure loss. Hence, local airflow is measured without creating a significant back pressure which could locally redistribute the flow. Important components of the flow measuring system are described in the following paragraphs.

A Hastings mass flowmeter was used to measure airflow rates. This particular unit was a series RKF flowmeter with a type K-1K transducer sized to operate in a range of 100 to 1000 standard cubic centimeters per minute. The measuring circuit consisted of an electrically heated tube instrumented with thermocouples to measure the differential cooling caused by air passing through the tube. Thermoelectric elements generated a d-c voltage proportional to the flow rate and gas specific heat. This system was insensitive to fairly large variations in pressure and temperature. Electrical output of the transducer operated a General Electric 520 mass flow recorder calibrated to give direct readings in SCCM through the use of a high-impedance, self-balancing potentiometer. The system was equipped with a Hastings LC-2 noise input filter and provisions for data recording.

A plastic tube of 0.25-in. (6.35 mm) inside diameter was used to cover four holes in the 0.096-in. (2.44 cm) center-to-center hole spacing regions of the airfoil. A special tube covering only one hole was used on the leading edge because of the sharp contour of the surface and the inability of a larger tube to maintain contact.

As shown in the schematic (Figure 11), the pressures in the vane airfoil cavity and the cooling air supply tube fitting (upstream) were measured with manometers. The airflow-pressure relationship could then be established at various locations around the periphery of the airfoil. With this information plus the air temperature and local barometer, it was possible to deduce the local flow resistance coefficients.

HIGH-TEMPERATURE CASCADE FACILITY

The cyclic test was performed in a high-temperature cascade facility designed to simulate actual engine conditions of pressure, temperature, mass flow, and geometry. The basic system is a multipurpose facility capable of testing blades and vanes of various sizes with minimum system modifications. For the test described herein, a relatively large burner capable of supplying 10.0- to 13.5-lb/sec (4.53 to 6.1 kg/sec) mass flow at 140 psia (96.5 N/cm^2) and 2800°F (1537.8°C) average temperature was used. As shown in Figure 12, the burner was

mounted vertically with the discharge connected to the test section by a 90-degree (1.57 rad) transition section.

The gas temperature distribution at the test section inlet varies spanwise similar to the radial profile of a gas turbine engine. To permit accurate measurement of the gas temperature, the top of the transition section has several openings for mounting traversing-type thermocouples. Remote control equipment is used to position the thermocouples to the desired depth, traversing from 0 to 4 in. (10.16 cm) to cover the entire height of the test section. Additional openings in the rig frame and gas liner provide access for instrumentation to measure gas temperature in the midchord plane of the test section. These temperature data are sufficient to define the temperature distribution at the test section inlet.

The rig openings are also used to obtain gas stream pressure profiles. As in a gas turbine engine, the total pressure does not vary significantly from hub to tip or in the midchord plane. Therefore, the pressure measurements were made primarily to determine if the desired pressure level was being achieved.

The cascade was equipped with sight ports which penetrated the outer walls of the cascade facility and the wall of the transition section. This arrangement is shown schematically in Figure 13. Special ducts with quartz windows were used to contain the gas stream and provide a view of the vanes. The vertical position of the burner allowed a direct line of sight to the leading-edge region of the three test vanes. The vane surface temperatures were obtained through the sight ports with infrared photography and optical pyrometry. The leading edges of the vanes can be viewed through sight port No. 16, shown in Figures 12 and 13. Sight ports No. 4, 9, and 13 (Figure 13) also afford views of the test and slave vanes, which are contoured in a manner that offers a view of the pressure side through sight port No. 4 and the suction side through sight ports No. 9 and 13.

Figures 14 through 16 are photographs of the facility. Figure 14 shows the hot air inlet piping connecting the preheater and the burner. A series of bends and expansion joints are provided in the piping to accommodate the thermal expansion associated with the 300 to 400°F (149 to 204°C) preheated air. Figure 14 also shows the view ports and the electric cooling-air heater.

The exhaust piping shown in Figure 15 is equipped to inject water into the gas stream to cool the exhaust gas before it is discharged to the atmosphere. Sight port No. 9 and the quartz window arrangement typical of all sight ports are also visible in Figure 15. Figure 16 provides a view of the combustion chamber and sight ports No. 4 and 16.

The hot rig components just upstream of the test section are shown in Figure 17. The openings in the top of the transition section are used for traversing thermocouple and pressure probes.

A set of five vanes—three test vanes and two slave vanes—assembled in a fixture constitutes the test section. Leading-edge and trailing-edge views are shown in Figures 18 and 19,

respectively. This test section is bolted into the opening shown in Figure 20. The three center vanes in Figures 18 and 19 are the test vanes, and the outside vanes form the side walls of the cascade. For identification, each vane in the cascade was numbered in sequence, beginning with vane No. 1—the right cascade wall (based on observing the vanes from a position upstream of the test section). Vanes 2, 3, and 4 were the test vanes.

The existing cooling air supply system was redesigned to achieve the following airfoil cooling air temperatures:

- Vane No. 1—steady 600°F (315.6°C)
- Vane No. 2—steady 600°F (315.6°C)
- Vane No. 3—cyclic between 600°F and 1000°F (315.6°C and 537.8°C)
- Vane No. 4—steady 1000°F (537.8°C)
- Vane No. 5—steady 600°F (315.6°C)

In order to attain a temperature of 1000°F (537.8°C) for the center test vane, the 600°F (315.6°C) preconditioned air was passed through a 150-kw electric heater. Cyclic conditions were established in this vane by using a valving arrangement that maintained constant flows of both 600°F (315.6°C) and 1000°F (537.8°C) streams so that the opening or closing of the valve would divert one stream or the other to the airfoil. Therefore, when the 600°F (315.6°C) cooling air stream was passing through the vane, the 1000°F (537.8°C) stream was bypassed to the atmosphere. The flow schematic for the cooling air circuit is shown in Figure 21.

To prevent clogging of the Lamilloy porous material airfoils by contaminants in the cooling air, a 99% efficiency, 5-micron (5×10^{-6} meter) particle size separator was used upstream of barrier-type filters which were also rated at 5 microns (5×10^{-6} meter). An additional 5-micron barrier filter was installed in each vane cooling air line.

INSTRUMENTATION AND CALIBRATION

The following is a summary of the primary measurements obtained in the hot cascade test. All instruments were calibrated within a short time before or after the test to ensure measurement accuracy.

Vane Cooling Airflow Rate

The cooling airflow rates to vanes 2, 3, and 4 were measured independently by sharp-edge, thin-plate orifices installed in standard flow measuring tubes. Flow rates to vanes 1 and 5 (slave vanes) were not measured.

Vane Wall Temperature

Thermocouples as well as infrared photography were used to measure airfoil metal temperature. Thermocouples are suitable for direct readout and continuous monitoring, both of which are required during the test to maintain the metal temperature at the desired level. Infrared photography provides a comprehensive record of the temperature of the entire surface in the field of view and makes it possible to determine isotherms and thermal gradients.

Six thermocouples were installed on each of vanes 2, 3, and 4 just beneath the outer surface of the porous wall at a depth of approximately 0.005 in. (0.127 mm). Because of the laminated, porous nature of the airfoil, a special technique was used in preparing and installing the thermocouples. Chromel-alumel wire of 0.004-in. (0.01 cm) dia was laser welded to form a junction which had a diameter of 0.020 in. (0.508 mm). The airfoil was prepared by drilling 0.022-0.024-in. (0.559 - 0.610 mm) holes through the wall at six locations. Small wires were welded to the 0.020-in. (0.508 mm) dia sheath that enclosed the thermocouple wires (at the end opposite the junction) so that the thermocouples could be drawn through the small, drilled holes and the access hole in the top of the vane. This procedure is demonstrated in Figure 22. With the thermocouple placed near the outer surface of the airfoil, the junction was laser welded to the outer laminate and the drilled hole was sealed with Hastelloy X filler metal by a laser welding process. A spacer was attached to the top of the vane to hold the thermocouple leads in position. These operations are shown in Figure 23. Finally, the instrumentation leads were secured by attaching them to the vane flange and cooling air fitting as shown in Figure 24.

The locations of the six thermocouples on each of the test vanes are shown schematically in Figures 25, 26, and 27 as referenced to grids. These grids were placed on vanes 2, 3, and 4 so that the thermocouples could be accurately located in the infrared photographs. The thermocouples were so positioned that at least two could be seen through each sight port; the fields of view through the sight ports are depicted schematically in Figure 28. Bench marks for identifying the thermocouple positions in the infrared photographs were established by marking vanes 2, 3, and 4 with grid tape. The subsequent photographs, made with panchromatic film, are shown in Figures 29 through 32. They define the field of view of the camera and relate the thermocouple locations to certain physical features of the rig which are also apparent. For example, small pins welded to the pressure surface of vane 1 served as bench marks. These pins extended approximately 0.2 in. (5.08 mm) from the vane surface and, during operation, appeared as local "hot spots" in the infrared photographs taken through sight port No. 4. The preoperation photographs, in conjunction with the thermocouple-grid relationship, provided the locations of the thermocouples with respect to the pins.

Details of the infrared photography technique for measuring vane surface temperature are described in Reference 7.

Gas Flow Rate

The gas stream flow rate was determined by measuring air and fuel flows and adding the two values. Thin-plate orifices installed in calibrated flow-measuring tubes were used to measure airflow. The fuel flow was measured by turbine drive-type frequency flowmeters.

Gas Pressure

Two static pressures were measured on the transition section inner wall approximately 1.25 in. (3.18 cm) upstream of the test section. The gas total pressure was computed from known, measured parameters and measured directly.

Gas Temperature

The average gas temperature was measured with a thermocouple probe that was traversed just upstream of the leading edges of vanes 2, 3, and 4 to obtain spanwise profiles. The average of these data was referenced to two fixed-position thermocouples which were monitored continuously.

Cooling Air Pressure and Temperature

A static pressure probe and a thermocouple were provided in each vane airfoil cavity to measure cooling air inlet conditions.

V. EXPERIMENTAL TEST PROGRAM

The objective of the test program was to determine the low cycle fatigue characteristics of a set of laminated porous material turbine vanes operating in a hot cascade rig. The rig test section, consisting of five vanes (four flow passages), was designed to simulate the aerodynamic, stress, and heat transfer conditions of a gas turbine engine.

LOCAL PERMEABILITY MEASUREMENTS

An important criterion for evaluating airfoil endurance characteristics is the magnitude of the permeability change caused by exposure to high temperature and subsequent oxidation. To determine the change in permeability for the low cycle fatigue vanes, local permeability measurements were made before and after the cascade rig test. In both cases, the test procedure and areas tested were identical.

Permeability measurements were made by pressurizing the airfoil through the cooling air inlet tube fitting and measuring the airflow from groups of four holes. Readings were taken around the entire periphery of the airfoil at three chordwise planes. Figures 33, 34, and 35 show the locations of the holes tested. For each group of holes, the airflow was measured at five pressure levels to completely describe the flow-pressure relationship.

VANE FLOW MEASUREMENTS

The overall flow rate for each test vane was measured prior to hot testing and after 110 cycles. In each case, the tests were made in the cascade rig with the rig inoperative and vented to the atmosphere so that the airfoil discharge side pressure was equal to the local barometric pressure and uniform around the airfoil. The vane cavity pressure was set at 10 psig (6.9×10^4 N/m). The air temperature was measured at the inlet to the airfoil cavity.

CASCADE RIG TEST

A cyclic test was performed on laminated porous material vanes in the hot cascade rig. The gas stream and cooling air temperatures were cycled to generate severe thermal gradients in the airfoil wall. The cycle extremes are identified as the high gas temperature condition and the low gas temperature condition. Nominal cycle data are listed in Table III.

The test cycle is shown graphically in Figure 36. The duration of each cycle was three minutes, divided evenly between the hot and cold gas temperature conditions. During the hot portion of the gas temperature cycle, the actual cooling air temperature to vane 3 was reduced to approximately 570°F (299°C). As fuel flow to the burner was decreased to reduce the gas temperature,

TABLE III. NOMINAL TEST CONDITIONS.

	High gas temperature condition	Low gas temperature condition
Gas temperature, °F (°C)	2800 (1538)	1300 (704)
Gas flow per passage, lb/sec (kg/sec)	3.2 (1.45)	3.2 (1.45)
Gas total pressure, psia (N/cm^2)	140 (96.5)	---
Maximum vane metal temperature, °F (°C)		
Vane No. 2	1700 (927)	
Vane No. 3	1700 (927)	
Vane No. 4	1700 (927)	
Cooling air/gas ratio, %		
Vane No. 2	4	4
Vane No. 3	4	5
Vane No. 4	5	5
Cooling air temperature, °F (°C)		
Vane No. 2	600 (316)	600 (316)
Vane No. 3	600 (316)	1000 (538)
Vane No. 4	1000 (538)	1000 (538)

the actual cooling air temperature to vane 3 was increased to approximately 870°F (466°C), which, because of piping heat losses, was about 130°F (72°C) lower than desired. Vanes 2 and 4 were exposed to the same gas temperature cycle, but the cooling air temperatures were held nearly constant to satisfy the conditions shown in Table III.

The planned duration of the test was 1000 cycles. However, low cycle fatigue of vanes 2, 3, and 4 caused the test to be terminated after 110 cycles. The following measurements were made before the first cycle and at approximately 100 cycles:

1. Static pressure at the test section inlet
2. A single-point measurement of gas temperature (this value was related to the average gas temperature by making a gas stream survey)
3. Cooling air supply pressure at the inlet of each test vane
4. Cooling air temperature at the inlet of each test vane
5. Maximum surface temperature of each test vane as measured by an optical pyrometer
6. Local surface temperature of each test vane as measured with thermocouples
7. Cooling airflow rate for each test vane
8. Gas flow rate

Before the start and following completion of the test, gas temperature and pressure profiles were to have been established with the aid of traversing probes. Because of the early termination, only the pretest profiles were measured.

Detailed airfoil metal temperature surveys were made prior to the first cycle by infrared photographic techniques. Optical pyrometer data were recorded at half-hour intervals for the leading edge midspan region at the high gas temperature condition. The experimental measurements are discussed in more detail in Section VI of this report.

VI. RESULTS AND DISCUSSION

PERMEABILITY TEST RESULTS

As shown previously, flow resistance in Lamilloy porous material comprises both viscous and inertial pressure losses which are functions of the mass flow rates and passage dimensions involved. The method used to account for these losses was originally developed by Green[8] for application to homogeneous, sintered-type porous materials. Although Lamilloy is not homogeneous, Green's equation has been shown to be a good representation of its flow-pressure drop characteristics.[1] The equation contains two constants which must be determined experimentally for each location— α (the viscous loss coefficient) and β (the inertial loss coefficient).* The coefficients are defined as follows:

$$\frac{(P_1^2 - P_2^2)\, g}{\tau \mu^2\, (2\, RT)} = \alpha\left(\frac{G}{\mu}\right) + \beta\left(\frac{G}{\mu}\right)^2 \qquad (1)$$

The purpose of the permeability testing described in these pages was to determine local values of α and β at the mean section and at sections 1 in. above and 1 in. below the mean section. Four holes were included in each measurement, and the exact locations were recorded (Figures 33, 34, and 35) so that the measurements could be duplicated after the cyclic cascade test.

To evaluate α and β, the pressure upstream and downstream of the porous airfoil, the air temperature, and the flow rate were measured. These measurements provide the experimental data for evaluating P_1, P_2, T, and G in Equation (1). Since G is a specific mass flow, it was necessary to divide the mass flow by the surface area associated with four holes, which is equal to four times the square of the hole spacing. The remaining quantities in Equation (1) are:

R—the universal gas constant
g—gravitational constant
μ—the viscosity of air
τ—the wall thickness

Thus, all the terms were accounted for except α and β, the proportionality constants. The test data, therefore, were taken over a range of pressures and flow rates so that reasonably accurate values could be assigned to α and β. An example calculation follows to demonstrate this technique.

The following were the measured data for location 7 on vane No. 2 (pressure surface):

---

*All symbols are defined in the list of symbols which follows the text.

Vane cavity pressure, in. Hg gage (N/m^2)	Airflow rate, SCCM	Air temp, °F (°C)	Barometer, in. Hg (N/m^2)
1.3 (4,400)	203	76 (23)	29.20 (9.86×10^4)
2.4 (8,100)	341	76 (23)	29.20 (9.86×10^4)
3.6 (12,200)	496	76 (23)	29.20 (9.86×10^4)
4.8 (16,200)	605	76 (23)	29.20 (9.86×10^4)
6.0 (20,300)	730	76 (23)	29.20 (9.86×10^4)

The data were plotted in the form $\frac{(P_1^2 - P_2^2)\, g}{2\, \mu RT\, \tau\, G}$ vs $\frac{G}{\mu}$ as shown in Figure 37. Equation (1) is linear; therefore, a least-squares, straight-line fit of the data was made with α the intercept and β the slope of the line.

The data for the three test vanes (positions 2, 3, and 4) are presented in Tables IV through VI for the as-fabricated condition and Tables VII through IX for the after-cyclic-test condition. These data have been reviewed to determine whether the cyclic exposure induced a general flow reduction or increase. The review revealed no particular trends were found in the data but, in certain locations, considerable scatter in the results was noted. This indicates a need to revise the test procedure if this type of test is to be performed in the future to evaluate small changes in permeability.

The permeability data did not show any systematic changes in the airfoil flow-pressure drop characteristics. Where changes in flow rate occurred, they were within the normal data scatter range for this test procedure.

In addition to the local permeability evaluation, the total vane flow rates were measured before and after the cyclic test. The tests were conducted with the vanes installed in the cascade rig and the test chamber vented to the room. The three test vanes were pressurized to approximately 10 psig (6.98×10^4 N/m^2) pressure; pressures, air temperature, and airflow rates were measured as follows:

Vane number	Vane cavity pressure, in. Hg abs (N/m^2)	Vane discharge pressure, in. Hg abs (N/m^2)	Total vane flow rate, lb/sec (kg/sec)	Air temperature, °F (°C)
2 (before)	50.3 (17.0×10^4)	29.2 (9.86×10^4)	0.0653 (0.0296)	60 (15)
2 (after)	51.6 (17.4×10^4)	29.2 (9.86×10^4)	0.082 (0.037)	60 (15)
3 (before)	50.7 (17.1×10^4)	29.2 (9.86×10^4)	0.0687 (0.0310)	60 (15)
3 (after)	54.9 (18.5×10^4)	29.2 (9.86×10^4)	0.0603 (0.0274)	60 (15)
4 (before)	50.3 (17.0×10^4)	29.2 (9.86×10^4)	0.0752 (0.0341)	60 (15)
4 (after)	53.4 (18.0×10^4)	29.2 (9.86×10^4)	0.0759 (0.0344)	60 (15)

TABLE IV. LOCAL PERMEABILITY DATA FOR VANE NO. 2 BEFORE CYCLIC TEST.

Location	α, in.$^{-2}$ (m^{-2})	β, in.$^{-1}$ (m^{-1})
1	108.2×10^7 (16.8×10^{11})	8.557×10^5 (3.37×10^7)
2	108.7 (16.8)	7.669 (3.02)
3	126.7 (19.6)	9.600 (3.78)
4	154.7 (24.0)	9.304 (3.66)
5	177.7 (27.5)	5.252 (2.07)
6	177.4 (27.5)	9.218 (3.63)
7	173.7 (26.9)	12.201 (4.80)
8	123.4 (19.1)	9.945 (3.92)
9	113.7 (17.6)	10.158 (4.00)
10	135.1 (20.9)	9.857 (3.88)
11	184.3 (28.6)	10.189 (4.01)
12	190.6 (29.5)	9.366 (3.69)
13	209.8 (32.5)	10.601 (4.17)
14	230.4 (35.7)	10.014 (3.94)
15	326.2 (50.6)	10.136 (3.99)
16	124.1 (19.2)	8.583 (3.38)
17	119.9 (18.6)	9.688 (3.81)
18	135.5 (21.0)	11.540 (4.54)
19	137.1 (21.3)	11.115 (4.38)
20	129.3 (20.0)	18.579 (2.88)
21	238.4 (37.0)	5.397 (2.12)
22	218.3 (33.8)	9.388 (3.70)
23	230.4 (35.7)	33.652 (13.25)
24	261.9 (33.5)	17.729 (6.98)
25	118.0 (18.3)	12.084 (4.76)
26	92.8 (14.4)	6.988 (2.75)
27	92.3 (14.3)	6.149 (2.42)
28	88.4 (13.7)	7.713 (3.04)
29	80.7 (12.5)	6.374 (2.51)
30	84.0 (13.0)	7.698 (3.03)
31	78.1 (12.1)	5.847 (2.30)
32	85.4 (13.2)	6.159 (2.42)
33	121.1 (18.8)	16.409 (6.46)
34	107.9 (16.7)	10.141 (3.99)
35	83.7 (13.0)	6.754 (2.66)
36	87.1 (13.5)	7.750 (3.05)
37	123.9 (19.2)	11.324 (4.46)
38	106.6 (16.5)	11.834 (4.66)
39	110.9 (17.2)	8.182 (3.22)
40	91.6 (14.2)	5.958 (2.35)
41	218.4 (33.9)	19.338 (7.61)
42	140.4 (21.8)	14.969 (5.89)
43	9.3 (1.4)	8.591 (1.33)
44	81.5 (12.6)	5.355 (2.11)
45	82.7 (12.8)	5.405 (2.13)
46	131.6 (20.4)	11.485 (4.52)
47	82.2 (12.7)	6.080 (2.39)
48	80.9 (12.5)	5.049 (1.99)
49	83.7 (13.0)	4.649 (1.83)

TABLE V. LOCAL PERMEABILITY DATA FOR VANE NO. 3 BEFORE CYCLIC TEST.

Location	α, in.$^{-2}$ (m^{-2})	β, in.$^{-1}$ (m^{-1})
1	133.3×10^7 (20.7×10^{11})	17.554×10^5 (2.72×10^7)
2	125.9 (19.5)	16.878 (6.64)
3	135.1 (20.9)	15.357 (6.05)
4	168.0 (26.0)	10.704 (4.21)
5	155.3 (24.1)	14.271 (5.62)
6	168.7 (26.1)	17.371 (6.84)
7	236.9 (36.7)	23.406 (9.21)
8	128.3 (19.9)	14.501 (5.71)
9	121.7 (18.9)	14.536 (5.72)
10	129.9 (20.1)	15.171 (5.97)
11	135.2 (21.0)	14.804 (5.83)
12	149.8 (23.2)	13.423 (5.28)
13	239.0 (37.0)	27.853 (10.97)
14	202.9 (31.4)	13.079 (5.15)
15	97.2 (15.1)	14.374 (5.66)
16	99.1 (15.4)	11.296 (4.41)
17	116.7 (18.1)	15.674 (6.17)
18	133.1 (20.6)	15.182 (5.98)
19	158.3 (24.5)	13.987 (5.51)
20	175.5 (27.2)	17.109 (2.65)
21	150.9 (23.4)	26.691 (10.51)
22	172.6 (26.8)	20.121 (7.92)
23	287.3 (44.5)	14.012 (5.52)
24	150.9 (23.4)	15.873 (6.25)
25	92.0 (14.3)	8.087 (3.18)
26	76.3 (11.8)	5.956 (2.34)
27	81.8 (12.7)	7.081 (2.79)
28	76.9 (11.9)	7.779 (3.06)
29	93.9 (14.6)	8.919 (3.52)
30	81.8 (12.7)	8.943 (3.52)
31	101.5 (15.7)	9.768 (3.85)
32	244.3 (37.9)	15.808 (6.22)
33	105.2 (16.3)	12.766 (5.03)
34	196.8 (30.5)	31.244 (12.29)
35	68.4 (10.6)	3.587 (1.41)
36	72.6 (11.3)	4.349 (1.71)
37	84.4 (13.1)	5.322 (2.10)
38	86.3 (13.4)	5.402 (2.13)
39	72.1 (11.2)	7.270 (2.86)
40	74.9 (11.6)	6.536 (2.57)
41	280.4 (43.5)	19.100 (7.52)
42	126.5 (19.6)	19.711 (7.76)
43	93.6 (14.5)	10.488 (4.13)
44	75.6 (11.7)	6.387 (2.51)
45	77.0 (11.9)	7.162 (2.82)
46	78.9 (12.2)	7.110 (2.80)
47	77.6 (12.0)	6.280 (2.47)
48	76.3 (11.8)	5.848 (2.30)
49	78.8 (12.2)	6.293 (2.48)

TABLE VI. LOCAL PERMEABILITY DATA FOR VANE NO. 4 BEFORE CYCLIC TEST.

Location	α, in.$^{-2}$ (m^{-2})	β, in.$^{-1}$ (m^{-1})
1	87.1×10^7 (13.5×10^{11})	8.275×10^5 (3.26×10^7)
2	81.0 (12.6)	8.454 (3.33)
3	101.6 (15.7)	11.850 (4.67)
4	112.7 (17.5)	13.501 (5.32)
5	129.4 (20.1)	15.612 (6.15)
6	140.0 (21.7)	15.676 (6.17)
7	149.8 (23.2)	17.524 (6.90)
8	89.8 (13.9)	13.028 (5.13)
9	92.2 (14.3)	11.819 (4.65)
10	104.4 (16.2)	13.236 (5.21)
11	119.8 (18.6)	15.434 (6.08)
12	133.8 (20.7)	15.466 (6.09)
13	173.9 (27.0)	18.352 (7.23)
14	183.5 (28.4)	16.941 (6.67)
15	95.8 (14.8)	12.353 (4.86)
16	93.1 (14.4)	12.720 (5.01)
17	105.4 (16.3)	13.532 (5.33)
18	134.7 (20.9)	15.639 (6.16)
19	131.5 (20.4)	17.022 (6.70)
20	241.4 (37.4)	11.554 (4.55)
21	207.4 (32.1)	16.624 (6.54)
22	194.7 (30.2)	18.297 (7.20)
23	168.0 (26.0)	18.842 (7.42)
24	97.1 (15.1)	9.305 (3.66)
25	88.0 (13.6)	7.467 (2.94)
26	103.5 (16.0)	10.116 (3.98)
27	99.6 (15.4)	8.302 (3.27)
28	105.3 (16.3)	8.533 (3.36)
29	100.1 (15.5)	6.353 (2.50)
30	103.3 (16.0)	8.544 (3.36)
31	106.7 (16.5)	11.488 (4.52)
32	114.8 (17.8)	11.791 (4.64)
33	88.8 (13.8)	7.738 (3.05)
34	97.5 (15.1)	8.407 (3.31)
35	94.6 (14.7)	10.132 (3.99)
36	99.9 (15.5)	10.106 (3.98)
37	95.0 (14.7)	14.582 (5.74)
38	101.2 (15.7)	7.380 (2.91)
39	223.1 (34.6)	19.407 (7.64)
40	139.9 (21.7)	19.179 (7.55)
41	97.7 (15.1)	11.251 (4.43)
42	88.9 (13.8)	9.253 (3.64)
43	92.2 (14.3)	10.250 (4.04)
44	119.0 (18.4)	10.520 (4.14)
45	98.8 (15.3)	13.612 (5.36)
46	92.7 (14.4)	8.661 (3.41)
47	96.5 (15.0)	7.414 (2.92)

TABLE VII. LOCAL PERMEABILITY DATA FOR VANE NO. 2 AFTER CYCLIC TEST.

Location	α, in.$^{-2}$ (m^{-2})		β, in.$^{-1}$ (m^{-1})	
1	247.1×10^7	(38.3×10^{11})	13.458×10^5	(5.30×10^7)
2	119.5	(18.5)	8.552	(3.37)
3	120.1	(18.6)	11.251	(4.43)
4	137.1	(21.3)	9.570	(3.77)
5	152.9	(23.7)	12.854	(5.06)
6	165.7	(25.7)	14.450	(5.69)
7	174.4	(27.0)	13.887	(5.47)
8	113.2	(17.5)	10.164	(4.00)
9	109.9	(17.0)	11.323	(4.46)
10	126.9	(19.7)	9.6800	(1.500)
11	168.3	(26.1)	13.392	(5.27)
12	181.9	(28.2)	16.013	(6.30)
13	157.1	(24.4)	15.229	(6.00)
14	187.2	(29.0)	17.537	(6.90)
15	249.5	(38.7)	23.256	(9.16)
16	123.6	(19.2)	8.563	(3.37)
17	122.6	(19.0)	7.913	(3.12)
18	124.2	(19.3)	11.843	(4.66)
19	125.6	(19.5)	14.223	(5.60)
20	155.3	(24.1)	15.730	(6.19)
21	184.0	(28.5)	11.932	(4.70)
22	175.0	(27.1)	15.881	(6.25)
23	272.7	(42.3)	5.329	(2.10)
24	501.0	(77.7)	24.209	(9.53)
25	149.2	(23.1)	13.786	(5.43)
26	108.8	(16.9)	7.443	(2.93)
27	109.3	(16.9)	8.275	(3.26)
28	104.8	(16.2)	7.401	(2.91)
29	91.3	(14.2)	7.457	(2.94)
30	96.2	(14.9)	7.321	(2.88)
31	91.9	(14.2)	5.949	(2.34)
32	21.6	(13.3)	13.157	(5.18)
33	130.4	(20.2)	13.811	(5.44)
34	113.3	(17.6)	8.324	(1.29)
35	95.4	(14.8)	6.136	(2.42)
36	139.8	(21.7)	10.074	(3.97)
37	382.1	(59.2)	17.265	(6.80)
38	250.3	(38.8)	15.998	(6.30)
39	177.5	(27.5)	13.781	(5.43)
40	68.9	(10.7)	9.879	(3.89)
41	262.3	(40.7)	10.564	(4.16)
42	133.6	(20.7)	15.422	(6.07)
43	87.7	(13.6)	9.043	(3.56)
44	85.4	(13.2)	4.141	(1.63)
45	94.4	(14.6)	5.042	(1.99)
46	154.6	(24.0)	14.541	(2.25)
47	86.9	(13.5)	10.658	(1.65)
48	84.9	(13.2)	5.320	(2.09)
49	71.5	(11.1)	7.471	(2.94)

TABLE VIII. LOCAL PERMEABILITY DATA FOR VANE NO. 3 AFTER CYCLIC TEST.

Location	α, in.$^{-2}$ (m^{-2})		β, in.$^{-1}$ (m^{-1})	
1	216.4×10^7	(33.5×10^{11})	15.576×10^5	(6.13×10^7)
2	161.2	(25.0)	16.046	(6.32)
3	205.7	(31.9)	21.159	(8.33)
4	71.3	(11.1)	41.633	(16.39)
5	206.3	(32.0)	13.141	(5.17)
6	216.5	(33.6)	19.103	(7.52)
7	234.0	(36.3)	6.416	(2.53)
8	141.3	(21.9)	11.904	(4.69)
9	142.6	(22.1)	12.914	(5.08)
10	151.1	(23.4)	15.247	(6.00)
11	192.9	(29.9)	19.006	(7.48)
12	261.3	(40.5)	13.887	(5.47)
13	148.4	(23.0)	26.799	(10.55)
14	193.0	(29.9)	21.355	(8.41)
15	121.9	(18.9)	8.719	(3.43)
16	113.6	(17.6)	6.970	(2.74)
17	130.6	(20.2)	12.440	(4.90)
18	147.8	(22.9)	13.287	(5.23)
19	169.5	(26.3)	16.179	(6.37)
20	295.1	(45.7)	11.217	(4.42)
21	301.9	(46.8)	15.175	(5.97)
22	213.2	(33.0)	18.656	(7.34)
23	396.4	(61.4)	50.701	(19.96)
24	256.6	(39.8)	13.429	(5.29)
25	136.9	(21.2)	9.354	(3.68)
26	153.8	(23.8)	12.328	(4.85)
27	285.6	(44.3)	20.328	(8.00)
28	422.9	(65.5)	53.824	(21.19)
29	---	---	---	---
30	259.8	(40.3)	10.704	(4.21)
31	128.1	(19.9)	6.232	(2.45)
32	222.3	(34.5)	28.738	(11.31)
33	156.5	(24.3)	4.406	(1.73)
34	102.5	(15.9)	7.834	(3.08)
35	73.5	(11.4)	8.500	(3.35)
36	190.0	(29.5)	33.766	(13.29)
37	---	---	---	---
38	---	---	---	---
39	294.4	(45.6)	49.199	(19.37)
40	183.1	(28.4)	20.685	(8.14)
41	299.8	(46.5)	13.401	(5.28)
42	136.7	(21.2)	15.012	(5.91)
43	95.5	(14.8)	8.243	(3.25)
44	---	---	---	---
45	192.9	(29.9)	14.433	(5.68)
46	390.4	(60.5)	34.038	(13.40)
47	190.0	(29.5)	19.999	(7.87)
48	160.7	(24.9)	10.546	(4.15)
49	93.4	(14.5)	8.688	(3.42)

TABLE IX. LOCAL PERMEABILITY DATA FOR VANE NO. 4 AFTER CYCLIC TEST.

Location	α, in.$^{-2}$ (m^{-2})	β, in.$^{-1}$ (m^{-1})
1	56.1×10^7 (8.7×10^{11})	13.893×10^5 (5.47×10^7)
2	79.7 (12.4)	9.506 (3.74)
3	108.4 (16.8)	10.420 (4.10)
4	104.8 (16.2)	14.795 (5.82)
5	134.5 (20.8)	14.237 (5.61)
6	153.4 (23.8)	11.733 (4.62)
7	162.8 (25.2)	13.194 (5.19)
8	109.0 (16.9)	7.876 (3.10)
9	108.8 (16.9)	5.679 (2.24)
10	124.1 (19.2)	8.314 (3.27)
11	129.6 (20.0)	10.109 (3.98)
12	129.0 (20.0)	12.094 (4.76)
13	182.0 (28.2)	10.523 (4.14)
14	202.8 (31.4)	9.729 (3.83)
15	101.8 (15.8)	15.019 (5.91)
16	99.5 (15.4)	15.110 (5.95)
17	104.7 (16.2)	13.173 (5.19)
18	134.1 (20.8)	16.467 (6.48)
19	142.3 (22.1)	16.581 (6.53)
20	211.4 (32.8)	23.915 (9.42)
21	209.9 (32.5)	15.202 (5.99)
22	209.9 (32.5)	13.667 (5.38)
23	165.0 (25.6)	17.423 (6.86)
24	92.6 (14.4)	7.889 (3.11)
25	72.4 (11.2)	7.780 (3.06)
26	103.6 (16.1)	9.473 (3.73)
27	98.6 (15.3)	8.835 (3.47)
28	84.4 (13.1)	10.721 (4.22)
29	77.2 (12.0)	9.976 (3.93)
30	77.2 (12.0)	10.644 (4.19)
31	94.9 (14.7)	10.113 (3.98)
32	104.8 (16.2)	9.045 (3.56)
33	85.7 (13.3)	5.861 (2.31)
34	91.5 (14.2)	6.775 (2.67)
35	106.3 (16.5)	8.990 (3.54)
36	111.0 (17.2)	8.396 (3.31)
37	109.4 (17.0)	7.418 (2.92)
38	94.9 (14.7)	12.322 (4.85)
39	208.1 (32.3)	22.431 (8.83)
40	120.2 (18.6)	20.039 (7.89)
41	95.4 (14.8)	9.777 (3.85)
42	87.5 (13.6)	8.122 (3.20)
43	104.6 (16.2)	9.019 (3.55)
44	118.4 (18.4)	11.659 (4.59)
45	120.9 (18.7)	9.464 (3.73)
46	123.9 (19.2)	4.318 (1.70)
47	83.2 (12.9)	8.258 (3.25)

The data tabulated at the bottom of page 20 were taken to measure flows at 50.3 in. Hg abs (17.0×10^4 N/m^2) and make a direct comparison of the results to determine flow changes. However, the airfoil cavity pressure was not repeated in each case, so it is useful to adjust the flow values to a common pressure level. This can be most easily accomplished by considering that the change in airfoil pressure ratio (P_2/P_1) is small enough to permit the assumption that the corrected coolant flow $\left(\frac{W}{A}\frac{\sqrt{T}}{P_1}\right)$ remains essentially constant. Adjusting the flow rate from the measured cavity pressure (condition 1) to a cavity pressure of 10 psig (6.98×10^4 N/m^2) (condition 2) is then simply a matter of multiplying the measured flow by the ratio of the pressures,

$$W_2 = \frac{(P_1)_2}{(P_1)_1} W_1$$

The results are as follows:

Vane number	Vane cavity pressure, in. Hg abs (N/m^2)	Vane discharge pressure, in. Hg abs (N/m^2)	Total vane flow rate, lb/sec (kg/sec)	Air temperature, °F (°C)
2 (before)	50.3 (17.0×10^4)	29.2 (9.86×10^4)	0.0653 (0.0296)	60 (15)
2 (after)	50.3 (17.0×10^4)	29.2 (9.86×10^4)	0.080 (0.0363)	60 (15)
3 (before)	50.3 (17.0×10^4)	29.2 (9.86×10^4)	0.0681 (0.0309)	60 (15)
3 (after)	50.3 (17.0×10^4)	29.2 (9.86×10^4)	0.0552 (0.0250)	60 (15)
4 (before)	50.3 (17.0×10^4)	29.2 (9.86×10^4)	0.0752 (0.0341)	60 (15)
4 (after)	50.3 (17.0×10^4)	29.2 (9.86×10^4)	0.0716 (0.0325)	60 (15)

These data show that vane No. 2 increased 22% in flow during the cyclic test period. A severe crack found in the leading edge of this vane after the cyclic test tends to explain this flow increase.

Vane No. 3 decreased 19% in flow. This change may be the result of oxidation or foreign material collected in the porous airfoil. An interesting comparison between the local permeability data and the total flow data could be made by using the local values to compute total vane flow for a cavity pressure of 50.3 in. Hg abs (17.0×10^4 N/m^2). This calculation would be only approximate, however, because less than half the local permeability values were measured for the airfoil.

The flow for vane No. 4 changed less than 5%, which is of the order of magnitude of the measurement error. Therefore, this flow change is not considered significant.

CASCADE TEST RESULTS

After rig checkout and preliminary adjustment of the cascade controls, the cyclic endurance test was begun. It continued without interruption through 110 cycles when, as indicated in Section V, the test was terminated because of observed fatigue failure (crack initiation) in all three test vanes.

Prior to the start of the automatic cyclic operation, a reasonably complete log of pertinent operational data was obtained. Several of the more significant experimental measurements for the initial (0) cycle are listed in Table X. The indicated peak gas temperature of 2660°F (1460°C) was measured with an open-tip probe and is not corrected for radiation losses. Based on a radiant loss analysis,[4] the true peak gas temperature should be 150°F (83°C) to 200°F (111°C) higher than the indicated reading from a probe of this design. This would imply that the true peak gas temperature was probably above 2800°F (1538°C) and thus consistent with the desired level.

TABLE X. CASCADE OPERATING CONDITIONS DURING INITIAL CYCLE.

	Low gas temperature condition	High gas temperature condition
Gas flow per passage, lb_m/sec (kg/sec)	3.214 (1.458)	3.242 (1.471)
Gas stream total pressure, in. Hg (N/cm^2)	201.4 (68.20)	281.0 (95.16)
Gas stream static pressure, in. Hg (N/cm^2)	193.9 (65.66)	273.5 (92.62)
Gas stream peak temperature, °F (°C)	1140 (616)	2660 (1460)
Cooling airflow, %		
Vane No. 2	5.12	4.61
Vane No. 3	4.71	3.39
Vane No. 4	4.50	4.27
Cavity pressure, in. Hg (N/cm^2)		
Vane No. 2	214.4 (72.60)	281.4 (95.29)
Vane No. 3	249.9 (84.63)	285.0 (96.51)
Vane No. 4	216.0 (73.15)	283.8 (96.10)
Coolant temperature in inlet elbow, °F (°C)		
Vane No. 2	557 (292)	527 (275)
Vane No. 3	867 (464)	570 (299)
Vane No. 4	840 (449)	900 (482)
Coolant temperature in cavity, °F (°C)		
Vane No. 2	520 (271)	630 (332)
Vane No. 3	810 (432)	695 (368)
Vane No. 4	782 (417)	960 (516)

The change in gas stream total pressure (corresponding to the change in gas stream total temperature level) is consistent with the anticipated operational characteristics of the cascade. Since it was desired to maintain a constant corrected gas flow (constant cascade inlet Mach No.) as well as a constant physical mass flow, it follows that the gas stream total pressure level should be proportional to the square root of the gas stream total temperature level. The changes in coolant cavity supply pressure in test vanes No. 2 and 4 are a natural consequence of the changes in gas stream pressure level because each airfoil cavity is supplied with air which is bled from the main air supply upstream of the test section. Hence, with no changes in valve setting during a given cycle, the cavity supply pressures (and hence coolant flows) will simply adjust to the main stream pressure level changes. The cooling airflow to vane No. 3 was purposely increased during the low temperature portion of the cycle to minimize coolant temperature changes caused by heat losses. This resulted in a more pronounced cyclic coolant flow change for vane No. 3 than for vanes No. 2 and 4.

A review of the measured coolant supply temperatures to the three vanes will show that the desired levels (refer to Section IV, page 13) were only approximated. In general, the coolant supply temperature levels were lower than desired because of heat losses from the delivery piping. A comparison of temperatures measured in the inlet elbow (upstream of vane cavity) with those measured in the airfoil cavity will show that the coolant loses heat at low gas temperatures and gains heat at high gas temperature levels. The coolant flow to vane No. 3 was increased during the low gas temperature portion of the cycle in an effort to minimize the coolant supply temperature drop. However, this procedure was only moderately successful.

The gas temperature profiles measured during the initial cycle are shown in Figure 38. This illustration reveals that circumferential gas temperature variation (at a given radial location) is modest. In the radial direction, the gas temperature levels are highest at about the 3/4 vane span position. The measured vane surface temperature distributions (Figures 39, 40, and 41) generally reflect the gas temperature profiles in that peak metal temperatures are observed near the 3/4-span position. The vane surface temperature profiles shown in these illustrations were obtained with infrared film. Calibration (film density level versus temperature) of the film density patterns was based on the indicated readings of the skin temperature thermocouples. Because of certain equipment limitations, infrared photographs through sight port No. 9 (see Figure 32) were not obtained during the test. Also, infrared photographs taken during the low gas temperature portion of the cycle did not provide useful data because radiant energy levels were too low to produce discernible film density changes.

The surface temperature data for test vane No. 2 have been replotted to provide an indication of the chordwise temperature distributions. These results, which were obtained from cross-plots of Figures 39 through 41, are shown in Figures 42, 43, and 44 for the 1/4-, 1/2-, and 3/4-span positions, respectively. The dashed portions of the curves represent regions for

which no infrared data were available. The solid portions of each curve were faired through individual infrared data points identified by sight port number. These results, which appear to be typical, show that the airfoil becomes more nearly isothermal (chordwise) near the hub region. Also, peak leading-edge temperatures occur near the 3/4-span position as observed previously.

In addition to the data logged during the initial cycle, selected measurements were made after 20, 40, 60, 80, and 100 cycles of operation. These data are summarized in Table XI; the zero cycle results are included for completeness. After the initial (zero) cycle, gas temperature, gas stream total pressure, gas flow, and cooling air cavity temperature were not measured directly. However, because the cascade cyclic operation was automated, the assumption is reasonable that these variables changed very little during the course of the test. For example, the cooling air temperature measured in the inlet elbow of vane No. 3 remained essentially constant (at a given gas temperature level) throughout the test.

The airfoil skin temperatures, measured with imbedded thermocouples, are also included in Table XI. The thermocouple numbers identify the measurement locations as defined in Figure 25. Although a number of the thermocouples failed during the test, the available readings show that surface temperatures (at a given gas temperature level) remained relatively constant. The available data also indicate that the test vanes were nearly isothermal during the low gas temperature portion of each cycle. This is consistent with predictions which show that small differences between gas and cooling air temperature will produce only modest chordwise surface temperature variations. It is noteworthy that the indicated leading edge surface temperatures on test vane No. 3 (thermocouples No. 1 and 4) are essentially equal to the coolant supply temperature during the low gas temperature portion of the cycle. These data imply that the normal temperature gradient (across the wall) was essentially zero during that portion of the cycle—a desirable condition from the standpoint of achieving the largest possible cyclic variation in normal temperature gradient.

The measured skin temperature response during a typical cycle is shown in Figure 45. The data were recorded during cycle No. 8 shortly after initiation of the automatic cycling operation. The indicated skin temperature at thermocouple location No. 4 on test vane No. 3 was recorded together with the vane cooling air supply temperature and the local peak gas temperature. Note, however, that the radial location of the peak gas temperature did not coincide with the (radial) location of skin temperature thermocouple No. 4. Consequently, the indicated skin temperature level is somewhat lower than that which occurred at the radial location corresponding to the peak gas temperature. The data shown in Figure 45 do indicate that (1) the gas temperature change was very rapid, occurring over a time span of approximately 1.8 seconds; (2) the vane leading-edge skin temperature response was almost instantaneous; (3) the cooling air supply temperature did not reach the desired level of 1000°F (538°C) during the low gas temperature portion of the cycle because of piping heat losses. The very rapid skin temperature response shown in Figure 45 is consistent with predictions which were made following the test to support the structural analysis of the vane fatigue failure. This work is discussed in detail in the following subsection.

TABLE XI. CASCADE

Cycle number	0		20	
Gas temperature level	Low	High	Low	
Gas stream inlet static pressure, in. Hg (N/cm^2)	193.9 (65.66)	273.5 (92.62)	204.0 (69.08)	274
Cooling airflow, %				
Vane No. 2	5.12	4.61	4.88	4.6
Vane No. 3	4.71	3.39	4.58	3.8
Vane No. 4	4.50	4.27	4.70	4.3
Cavity pressure, in. Hg (N/cm^2)				
Vane No. 2	214.4 (72.60)	281.4 (95.29)	217.6 (73.69)	282
Vane No. 3	249.9 (84.63)	285.0 (96.51)	---	286
Vane No. 4	216.0 (73.15)	283.8 (96.10)	243.5 (82.46)	285
Coolant temperature in inlet elbow—vane No. 3, °F (°C)	867 (464)	570 (299)	873 (467)	572
Skin temperatures—vane No. 2, °F (°C)				
Thermocouple No. 1	730 (388)	1535 (835)	740 (393)	154
Thermocouple No. 2	715 (379)	1490 (810)	725 (385)	151
Thermocouple No. 3	---	---	---	
Thermocouple No. 4	690 (366)	1375 (746)	700 (371)	136
Thermocouple No. 5	695 (368)	1425 (774)	700 (371)	142
Thermocouple No. 6	620 (327)	---	---	
Skin temperatures—vane No. 3, °F (°C)				
Thermocouple No. 1	865 (463)	1400 (760)	855 (457)	135
Thermocouple No. 2	---	---	---	
Thermocouple No. 3	---	---	---	
Thermocouple No. 4	860 (460)	1350 (732)	860 (460)	129
Thermocouple No. 5	---	---	---	
Thermocouple No. 6	---	---	---	
Skin temperatures—vane No. 4, °F (°C)				
Thermocouple No. 1	850 (454)	1490 (810)	880 (471)	149
Thermocouple No. 2	865 (463)	1610 (877)	885 (474)	160
Thermocouple No. 3	---	1515 (824)	880 (471)	161
Thermocouple No. 4	840 (449)	1480 (804)	870 (466)	147
Thermocouple No. 5	850 (454)	1580 (860)	875 (468)	157
Thermocouple No. 6	845 (452)	---	---	

PERATING CONDITIONS DURING CYCLIC OPERATION.

	40		60		80		100	
igh	Low	High	Low	High	Low	High	Low	High
(93.09)	206.0 (69.76)	272.5 (92.28)	204.6 (69.28)	274.0 (92.79)	197.0 (66.71)	271.6 (91.97)	206.0 (69.76)	273.5 (92.62)
	5.02	4.77	4.95	4.69	4.88	4.69	5.18	4.78
	4.67	3.79	4.67	3.79	4.58	3.76	4.55	3.73
	4.63	4.40	4.62	4.29	4.50	4.29	4.86	4.45
(95.50)	218.8 (74.09)	282.5 (95.66)	218.0 (73.82)	280.0 (94.82)	214.5 (72.64)	279.0 (94.48)	218.5 (73.99)	281.0 (95.16)
(96.85)	248.2 (84.05)	285.0 (96.51)	249.0 (84.32)	287.0 (97.19)	---	284.0 (96.17)	237.0 (80.26)	287.4 (97.32)
(96.51)	223.0 (75.52)	287.0 (97.19)	223.0 (75.52)	283.5 (96.00)	220.0 (74.50)	282.0 (95.50)	229.0 (77.55)	292.0 (98.88)
00)	872 (467)	565 (296)	872 (467)	568 (298)	867 (464)	566 (297)	866 (463)	569 (298)
841)	735 (391)	1540 (838)	730 (388)	1510 (821)	785 (418)	1520 (827)	735 (391)	1385 (752)
821)	720 (382)	1510 (821)	725 (385)	1480 (804)	780 (416)	1490 (810)	725 (385)	1330 (721)
---	---	---	---	---	---	---	---	---
738)	700 (371)	1370 (743)	700 (371)	1340 (727)	700 (371)	1375 (746)	700 (371)	1225 (663)
774)	700 (371)	1440 (782)	710 (377)	1390 (754)	710 (377)	1450 (788)	700 (371)	1260 (682)
---	---	---	---	---	---	---	---	---
732)	865 (463)	1430 (777)	860 (460)	1310 (710)	865 (463)	1360 (738)	860 (460)	1305 (707)
---	---	---	---	---	---	---	---	---
---	---	---	---	---	---	---	---	---
702)	865 (463)	1360 (738)	865 (463)	1250 (677)	855 (457)	1265 (685)	915 (491)	1230 (666)
---	---	---	---	---	---	---	---	---
---	---	---	---	---	---	---	---	---
810)	880 (471)	1500 (816)	880 (471)	1500 (816)	880 (471)	1510 (821)	---	---
871)	885 (474)	1625 (885)	885 (474)	1670 (910)	885 (474)	1660 (904)	905 (485)	1520 (827)
877)	880 (471)	1420 (771)	910 (488)	1190 (643)	895 (479)	1160 (627)	895 (479)	1130 (610)
799)	870 (466)	1490 (810)	860 (460)	1470 (799)	870 (466)	1500 (816)	885 (474)	1430 (777)
854)	865 (463)	1575 (857)	865 (463)	1570 (854)	860 (460)	1585 (863)	895 (479)	1430 (777)
---	---	---	---	---	---	---	---	---

The cascade facility was shut down after 110 cycles for rig maintenance. The test section was then routinely opened for a visual inspection of the vanes, which had shown no previous signs of distress. This inspection, however, revealed longitudinal as well as transverse cracks on test vane No. 2. Consequently, the vanes were removed from the cascade facility and the test was considered terminated. Photographs of the test vanes taken immediately after removal are shown in Figures 46 through 51. These photographs give evidence of transverse surface cracks in all three test vanes. In all cases, the primary damage area was the upper 1/3 (tip section) of the leading edge region. Test vane No. 2 was the most severely damaged unit, exhibiting a pronounced longitudinal crack along the leading edge (Figure 47). Numerous transverse cracks are also evident. Highly magnified views of the transverse cracks revealed strong evidence of thermal fatigue, so the airfoils were sectioned and submitted for detailed metallographical examination. Results of the posttest metallurgical and structural evaluations are discussed in the following subsection.

THERMAL/STRUCTURAL VANE ANALYSIS

As discussed under the previous heading, preliminary visual examination of the damaged test vanes indicated the strong possibility of low cycle thermal fatigue. A detailed metallurgical analysis later confirmed that low cycle thermal fatigue was the principal cause of failure (refer to the subsequent discussion under "Metallurgical Evaluation"). To explain the fatigue failure in terms of vane design deficiencies and/or the severity of the operating conditions, an airfoil life prediction analysis was made. The analysis was limited to test vane No. 2 with particular emphasis on the structural behavior of the badly damaged 3/4-span position. Test vane No. 2 was selected for analysis because the particular cyclic combination of gas stream and coolant temperature extremes resulted in the most pronounced excursions in chordwise metal temperature distribution.

Thermal Analysis

Low cycle thermal fatigue is strongly influenced by variations in chordwise surface temperature distribution; therefore, the transient surface temperature response to a typical gas temperature cycle was first predicted. Relevant test data were used in the analysis wherever possible to ensure consistency between predictions and actual operating conditions.

The thermal analysis was formulated in terms of a local energy conservation equation written for any arbitrary porous wall segment:

$$h_g (T_g - T_w) = G_c C_{p_c} (T_w - T_c) \eta + q_c + \rho_m C_{p_m} \frac{\partial T_m}{\partial t} \qquad (2)$$

The left hand term in Equation (2) represents the local heat transfer rate (per unit surface area) from the external gas stream to the airfoil surface. The first term on the right side of Equation

(2) represents the coolant energy absorption within and upstream of the porous wall. The wall conduction term, q_c, accounts for the net heat flow conducted out of an elemental wall section in the spanwise and chordwise directions. Thus,

$$q_c = k_m \tau \left(\frac{\partial^2 T_m}{\partial x^2} + \frac{\partial^2 T_m}{\partial y^2} \right) \tag{3}$$

The last term in Equation (2) represents the change in internal energy of an elemental volume of the porous wall.

For specified time-dependent fluid boundary conditions (h_g, G_c, T_g, T_c) and appropriate physical parameters (Cp_c, Cp_m, k_m, ρ_m, τ, η), Equation (2) can be solved to yield the time-dependent airfoil temperature distribution, T_m (x, y, t). The actual solution of Equation (2) was accomplished by representing the airfoil as a two-dimensional (spanwise and chordwise) surface unfolded around the leading edge as shown in Figure 52. With the surface conceptually divided into n nodal points, Equation (2) was written in finite difference form for each node point. The resulting system of equations was then numerically solved by using an alternating direction implicit (ADI) procedure.[9,10] With reference to the node pattern shown in Figure 53, the general finite difference formulation for any node (i, j) at any time, t, becomes

$$k_1 A_1 \frac{(T_{i,j-1} - T_{i,j})}{\Delta x} + k_2 A_2 \frac{(T_{i,j+1} - T_{i,j})}{\Delta x} + k_3 A_3 \frac{(T_{i-1,j} - T_{i,j})}{\Delta y}$$

$$+ k_4 A_4 \frac{(T_{i+1,j} - T_{i,j})}{\Delta y} + h_g \Delta x \Delta y \, (T_g - T_{i,j}) + G_c Cp_c \eta \, \Delta x \, \Delta y \, (T_c - T_{i,j})$$

$$+ \rho_m Cp_m \, (\Delta x \, \Delta y \, \tau) \frac{(T'_{i,j} - T_{i,j})}{\Delta t} = 0 \tag{4}$$

In Equation (4), $T'_{i,j}$ represents the temperature of the (i, j) node at a point in time equal to $(t - \Delta t)$. The conduction areas A_1 and A_2 are equal to the product $(\Delta y \cdot \tau)$; A_3 and A_4 are equal to the product $(\Delta x \cdot \tau)$. The parameters k_1, k_2, k_3, and k_4 represent effective porous wall thermal conductivity (k_m) values in the various (x-y) conduction directions (1 through 4 in Figure 52). When written in terms of Equation (4), the node temperature, $T_{i,j}$, effectively represents the wall surface temperature, T_w, so that the solution yields T_w as a function of time at any x, y location on the airfoil. The matrix temperature distribution in the normal (z) direction was estimated independently with a simpler, one-dimensional energy balance formulation.

The transient response analysis was applied to a model of test vane No. 2 (3/4-span section) which consisted of 41 nodes in the chordwise direction (trailing edge to trailing edge) plus three spanwise nodes at each chordwise location. Because spanwise heat flow is small relative to that in the other directions, this component of heat transfer was neglected in the analysis. The

predicted temperature distributions therefore reflect transient heat transfer in a convectively heated porous wall with axial (chordwise) conduction. In establishing the fluid boundary conditions for the analysis, the external film coefficient distribution (h_g) was assumed to be the same as predicted previously for test run No. 504 (reported in Reference 4). Because the airfoil profile, injection rates, and fluid temperatures and pressures in the cyclic cascade test were essentially identical with those of the earlier test,[4] no significant difference in the external film coefficient would be expected. The film coefficient prediction technique is described in detail in References 4 and 11. Another assumption made was that the predicted external film coefficient distribution (Figure 54) was invariant with time during any given cycle. This is a reasonable assumption because the cascade was operated at a constant physical mass flow throughout the cyclic test, and coolant injection rates did not change significantly during a given cycle.

The injection rate distribution (G_c) was established through a simple, steady-state energy balance to ensure compatibility of the measured and predicted steady-state temperature distributions at the high temperature end of the cycle. In other words, the injection rate distribution was determined from the relationship

$$h_g(T_g - T_w) = G_c Cp_c (T_w - T_c)\eta \qquad (5)$$

where the film coefficient distribution (h_g) was taken from Figure 54 and the surface temperature distribution (T_w) from Figure 44. This approach essentially "forces" the predicted surface temperature distribution to be equal to the measured steady-state distribution at the elevated temperature portion of the cycle. The alternate approach would have been to predict the G_c distribution based on the measured resistance coefficients (α, β) and the predicted static pressure distributions around the airfoil. However, the local measurements of α and β were highly unreliable and led to extreme variations in the local values of G_c predicted from Equation (1). Therefore, the simple energy balance approach [Equation (5)] was thought to provide internal boundary conditions more consistent with the observed steady-state temperature distributions. Although the effect of axial conduction is neglected in using Equation (5), little error was introduced by this simplifying assumption as will be shown later. The injection rate distribution determined from Equation (5) is shown as the solid curve in Figure 55, which h_i is defined as $G_c Cp_c \eta$ (Cp_c and η constant). Except in the leading-edge region, the local injection rates were assumed to be invariant with time during a given cycle. The levels of h_i in the leading-edge region, however, were adjusted upward to account for the larger local injection rates in this region during the low gas temperature portion of the cycle. The increased <u>local</u> injection rates (represented by the dashed curve in Figure 55) reflect the relatively large <u>local</u> increase in coolant-to-free-stream pressure difference during the low gas temperature portion of the cycle (refer to Table X).

The variations in gas temperature and coolant temperature during a typical cycle were based on the experimentally measured trends discussed previously. The initial surface temperature distribution (just before the gas temperature decrease) was considered to be the measured distribution given in Figure 44. The initial surface temperature distribution at the low gas temperature

end of the cycle was not directly measured. It was therefore assumed to be uniform (750°F), which appears reasonable based on available thermocouple readings. A summary of all appropriate boundary condition data used in the transient response analysis is provided in Table XII.

TABLE XII. BOUNDARY AND PROPERTY DATA FOR TRANSIENT RESPONSE ANALYSIS.

	High gas temperature condition	Low gas temperature condition
Gas temperature (T_g), °F (°C)	2750 (1510)	1150 (621)
Coolant temperature (T_c), °F (°C)	630 (332)	530 (277)
External film coefficient (h_g)	Figure 54	Figure 54
Injection distribution (internal film coefficient, h_i)	Figure 55 (solid curve)	Figure 55 (solid & dashed curves)
Initial surface temperature distribution	Figure 56 (top curve)	Figure 57 (bottom curve)
Wall thickness distribution (τ)	Figure 2	Figure 2
Porosity (P)	0.30	0.30
Thermal conductivity (k_m)*	Published Hastelloy X data	Published Hastelloy X data
Specific heat (Cp_m)*	Published Hastelloy X data	Published Hastelloy X data
Density (ρ_m)*	Published Hastelloy X data	Published Hastelloy X data
Thermal effectiveness (η)	0.75	0.75

Note: All variations in T_g, T_c, and h_i (between high and low gas temperature conditions) assumed to occur linearly over a time interval of 1.8 sec.

*Temperature dependence of all properties accounted for in analysis. These properties all multiplied by factor (1-P) to account for void volume effect.

The predicted transient response characteristics of test vane No. 2 (3/4-span section) are shown in Figures 56 and 57. The results clearly indicate that the leading-edge response rates are significantly greater than those of the side walls. This behavior primarily reflects the relatively large leading-edge film coefficients (Figure 54) but is also indicative of the greater thermal inertia of the thicker side walls. During the rapid gas temperature decrease (Figure 56), the leading-edge-to-side-wall temperature difference reverses, causing a reversal in leading-edge radial loading (compressive to tensile). During the rapid gas temperature increase (Figure 57), the compressive loading of the leading edge is reimposed. It can also be observed

that the leading-edge-to-side-wall temperature differences during the transient increase are much greater than those at steady state. For example, the maximum chordwise temperature difference is almost 500°F (260°C), occurring 2.4 sec after initiation of the gas temperature increase (Figure 57). The maximum chordwise temperature difference during the decreasing temperature portion of the cycle is approximately 400°F (204°C) (at 2.2 sec). The extreme chordwise temperature differences cited here are very significant because the relationship of the temperature levels (leading edge versus sidewall) reverses during a complete cycle.

The results shown in Figure 57 indicate that the predicted final steady-state temperature distribution (upper solid curve) closely approximates the measured distribution (dashed curve). The latter curve is identical with the measured distribution (Figure 44) from which the local injection rates were determined by use of Equation (5). The small differences between the two distributions reflect the error introduced by neglecting axial conduction in Equation (5). As stated previously, the effect of this simplifying assumption is indeed small.

The airfoil wall temperature gradients in the normal (z) direction were determined independently of the surface temperature analysis. For the initial condition (corresponding to the upper distribution in Figure 56), the normal temperature gradients were assumed to be equal to those previously reported.[4] During the transient, the relationship between the inside and outside wall temperatures was established by assuming that the parameter $\theta = \frac{T_o - T_c}{T_w - T_c}$ remained equal to the initial (steady state) value. Since it can be shown[2] that θ is largely dependent on wall geometry and injection rate, it is reasonable to assume that it would not vary significantly with time under the conditions of this test. With the benefit of this assumption, the inside surface temperature (T_o) may be estimated from the relationship

$$T_o = T_c + \theta (T_w - T_c) \qquad (6)$$

where θ is dependent only on the steady-state values of T_w, T_o, and T_c at any given chordwise location.

The time-dependent airfoil temperature distributions presented herein were subsequently used in the structural analysis of the test vane. A detailed discussion of this analysis follows.

Structural Analysis

Two computer programs were used to determine the stresses and strains in the airfoil. The first was used to determine the stress-strain history (longitudinal direction only) of each material fiber in a given cross section. The second was used to determine the relationship between the transverse and longitudinal strains in the critical area—the leading edge.

The stresses and strains at the leading edge were induced by (1) thermal gradients in the longitudinal, transverse, and normal (z) directions and (2) pressure differences across the wall.

When the cascade rig changes from the low to the high gas temperature operating condition, the thermal gradients near the leading edge become very large, as shown in Figure 57. A small region of the airfoil (leading edge) is much hotter than the much larger mass (sidewalls) a short distance away. The cooler material prevents the hotter material from expanding, thus forcing the leading edge into compression. On the other hand, when the rig changes from the high to the low gas temperature condition, the thermal gradients reverse—i.e., the leading edge becomes much cooler than the surrounding material (see Figure 56). Consequently, large tensile strains are induced in the leading edge.

Because the curvature at the leading edge produces a high section modulus to resist bending, and because the pressure drop across the leading edge is small, the longitudinal stresses induced by the internal pressure are small. The pressure distribution also induces bending about the principal axes of the cross section. Although these moments are included as input to the computer programs, they have virtually no effect at the leading edge because the thermal gradients dominate and the leading edge is too near the neutral axis.

The finite element model of the airfoil cross section is shown in Figure 58. The area of each of the elements was corrected for the etched patterns by weighing each sheet and establishing a ratio of metal-to-total volume. This ratio then was used to establish an "equivalent" area representing the area actually available to carry loads. For analytical purposes, a typical operating cycle was considered to comprise four temperature distributions: (1) a transient start-up distribution (Figure 57, 2.4 sec after leaving the low gas temperature condition) which is held for a very short duration, (2) a steady-state distribution at the high gas temperature condition (Figure 57) held for 90 sec, (3) a transient shutdown distribution (Figure 56, 2.2 sec after leaving the high gas temperature condition) held for a very short duration, and (4) a steady-state distribution at the low gas temperature condition held for 90 sec. The <u>average</u> temperature of each finite element in the model was determined from the local <u>surface</u> temperature (Figures 56 and 57) and the predicted inner surface temperature [from Equation (6)]. The normal (z direction) temperature distribution was assumed to be linear, so internal element temperatures were obtained by simple interpolation.

Associated with each of the operating conditions is a pressure distribution around the airfoil which produces a gas bending moment across the cross section under investigation. The pressure distributions, represented as local pressure differences across the airfoil wall, are plotted in Figure 59. By integrating pressure around the airfoil, the forces per unit length (axial and circumferential components) were obtained along the longitudinal axis. The gas bending moments at the critical section were obtained by integrating these distributed forces along the airfoil, which was treated as a beam fixed at the tip and simply supported at the hub with no longitudinal restraints. The moments (axial and circumferential components) associated with the high gas temperatures were used with the first two thermal distributions and the moments associated with the low gas temperatures were used with the remaining two thermal distributions.

The program output provides the total strain of each element at each loading condition. Usually, the element which must withstand the greatest change in strain during each cycle will be the one most likely to fail.* As the airfoil is cycled, the strains quickly stabilize to a fixed value at each loading condition. From experience, it is known that there is little variation in strain range after three cycles. In Figure 60, the total strains—plastic plus elastic—are plotted for the inside and outside laminates near the leading edge. The strains for all four thermal distributions are shown as they existed during the fifth cycle. Inspection revealed the outside laminate at element 46 to have the largest strain excursion during the cycle, the two transient temperature conditions causing the extremes. Figure 61 is a plot of strain versus stress for this element. Considerable yielding and a slight amount of creeping are evident.

The calculated maximum strain range in the leading edge region was 0.008 in./in. (cm/cm) as shown in Figure 61. The predicted life, or number of loading cycles before transverse cracking occurs, was obtained by entering Figure 62 with this strain range. The relationship between life and strain range shown in Figure 62 was based on DDAD test data for Lamilloy specimens subjected to strain cycling under isothermal conditions. The two strain-cycle curves shown in Figure 62 represent data projections** for the two temperatures which correspond to the extremes of the strain range. In compression, the greatest strain occurs at a metal temperature level of 1500°F (816°C); in tension, the corresponding temperature level is 800°F (427°C). The predicted lives are therefore 142 and 260 cycles, respectively (Figure 62).

A second finite element computer program was used to determine whether transverse strains were sufficiently large to open a fatigue crack in the longitudinal direction. The analysis, which accommodates variable pressure loading and variable transverse and longitudinal temperatures, solves for displacements, stresses, and strains in structures idealized by triangular plate elements. The program does not consider thermal gradients through the wall (z direction). However, these effects were estimated and assessed independently of the finite element calculation.

Figure 63 shows the airfoil conceptually divided into triangular plates. Three coordinates plus temperature and pressure must be designated at each node. As boundary conditions, the nodal displacements at the hub and tip were specified as the thermal growths of the apparatus retaining the airfoil.

A solution was obtained for the measured steady-state temperatures at the elevated gas temperature condition (see Figures 42 through 44). At the leading edge, the solution indicates the transverse strains and stresses to be less than 25% of the corresponding longitudinal values.

---

*It is possible, in some cases, for an element to have the greatest strain range but not be the most critical element because of a higher allowable strain range. This, however, was not the case in the test under discussion.

**Refer to appendix (page 107) for the method of projecting the low cycle fatigue test data for the conditions existing during the cascade testing.

This is consistent with what was expected, because the airfoil is much more flexible in bending about a longitudinal axis than about a transverse axis. The program computes only elastic stresses (no yielding), so that the transient temperature conditions (which produce considerable yielding) were not analyzed by this method. However, no reason exists to expect a different trend at the other temperatures; the longitudinal stresses and strains should remain larger than the transverse values.

In summary, it can be concluded that the leading edge of test vane No. 2 was severely loaded by thermal gradients which occurred during a given cycle. The cyclic variation in gas temperature produced severe excursions in chordwise metal temperature distribution. The transient metal temperature excursions, in turn, induced alternating longitudinal compressive and tensile strains in the leading-edge region. Based on typical material properties and the predictive techniques used herein, these strains should result in the initiation of a transverse crack after 142 cycles.*

Because the airfoil is more flexible in the transverse direction (bending about a longitudinal axis), the transverse strains are only about 25% of those which occur in the longitudinal direction. Consequently, in thermal (low cycle) fatigue, transverse cracks are the primary failures. Longitudinal cracks are either secondary fatigue failures or result from other damage, such as flaws introduced during fabrication. This is discussed in detail in the following subsection.

METALLURGICAL EVALUATION

After termination of the cyclic fatigue test, the three test vanes were removed from the cascade facility so that the type and mode of failure could be determined. The airfoils were sectioned in the relevant failure areas and the failure patterns were photographically recorded. Specifically, the metallurgical failure analysis consisted of:

- Spectrographic analysis to verify conformance of the material (Hastelloy X) to established Engineering Materials Specifications
- Photomacrographs of the internal, external, and sectioned airfoil surfaces to establish the general nature and location(s) of failure
- Photomicrographs of etched, transverse sections in the failure area(s) to establish the nature of failure progression—e.g., transgranular versus intergranular
- Electron scanning micrographs of the failure surfaces to reveal the topography of the failed area(s)

A photograph of the leading edge of test vane No. 2 is shown in Figure 64. As indicated previously, leading-edge cracks in this vane appear in both the longitudinal and transverse directions. The photomacrograph in Figure 65 shows a magnified external view of the leading-edge

*On the basis that the entire strain range is being experienced at T_m = 1500°F (816°C). If the entire strain range were experienced at 800°F (427°C), the predicted life would be 260 cycles.

cracks in vane No. 2; internal views of the same vane are displayed in Figure 66. The sheathed leading-edge thermocouple wires are clearly visible in the latter photograph. It is obvious from Figure 66 that the cracks are relatively straight (hole to hole) and that the holes have become somewhat diamond shaped. This indicates that the material had been strained beyond the elastic limit in this area. This distortion, which was unique to test vane No. 2, is felt to be a result of the airfoil cold forming operation and not directly related to the cyclic cascade test. It is therefore highly probable that the yielding which occurred during the forming operation was the primary contributing factor to the longitudinal crack in test vane No. 2.

Transverse cracks in the leading edge of test vane No. 3 are illustrated by photomacrographs (Figure 67) which show that some distortion of the inner metal surface occurred during forming. However, the hole elongation is modest when compared with test vane No. 2.

An internal view of the leading edge of test vane No. 4, revealing the transverse cracks between cooling air holes, is shown in Figure 68. The distortions and crack patterns in this vane are similar to those observed in test vane No. 3.

The photomacrograph in Figure 69 shows the failure surfaces of the bonded Hastelloy X sheets along the longitudinal crack in the leading edge of test vane No. 2. A photomacrograph of the failure surfaces along a transverse crack in the leading edge of test vane No. 3 is shown in Figure 70. The failure surface shown in this illustration is typical of other transverse leading-edge cracks found in the three test vanes.

Photomicrographs of etched transverse sections through the longitudinal cracks in test vane No. 2 revealed transgranular failure typical of fatigue (Figure 71). FeCl-HCl-CH_3OH was used as etchant for preparing the surfaces. Similar photomicrographs of sections through the leading-edge transverse cracks in test vanes No. 2 and 4 revealed failure which was partially intergranular and partially transgranular, indicating thermal fatigue. This is shown in Figure 72; $FECl_3$-HCl-CH_3OH was used as the failure surface etchant. Note the absence of any indication of delamination (bond failure) in the areas shown. This was true for all failure areas examined on test vanes No. 2 and 4. Photomicrographs of test vane No. 3 were essentially identical with those shown in Figure 72 and similarly revealed no evidence of delamination.

Electron scanning micrographs of the failure surfaces along the longitudinal crack in the leading edge of test vane No. 2 are shown in Figure 73. The two lower micrographs reveal fatigue striations which originated on the outer surface of the outer sheet (see identification in upper micrograph) and progressed completely through the sheet. Electron scanning micrographs of the failure surfaces along a transverse leading-edge crack in test vane No. 3 are shown in Figure 74. These micrographs reveal fatigue striations which progressed from the edge of a cooling-air hole (internal air passage side) toward the inner surface of the leading edge inner sheet. A thinning of the inner sheet in an area adjacent to the cooling-air hole is also evident. Scanning electron fractographs of a section through the outer sheet of test vane No. 4 are shown in Figure 75. These photographs are representative of a section at the end of a transverse

leading-edge crack and reveal fatigue striations which progressed from the internal cooling air passage to the outer surface of the outer sheet. Note that the electron scanning micrographs of the various transverse failure regions reveal striations which progress from an interior coolant passage toward the inner radius in one case (test vane No. 3) and toward the outer radius in another (test vane No. 4). This bidirectional failure propagation provides substantial evidence of alternate tensile and compressive loading which, in turn, are related to the transient chordwise temperature gradient reversals discussed previously.

In summary, the following are the salient points of the metallographic examination of the three test vanes.

- Each of the failure surfaces examined revealed progressive fatigue failure.
- Ductile tension abetted by intermittent areas of fatigue was the primary cause of the longitudinal crack failure along the leading edge of test vane No. 2.
- The transverse cracks in all three test vanes were partially transgranular and partially intergranular, indicative of thermal fatigue.
- No indications of delamination (bond failure) of the bonded Hastelloy X sheets of the airfoil were evident.
- Spectrographic analysis verified conformance of the material to EMS-70799 (Hastelloy X) as required by the engineering drawing.
- No metallurgical causes for failure were noted.

VII. GENERAL OBSERVATIONS AND RECOMMENDATIONS

The results of the present program have clearly demonstrated that severe transient excursions in gas temperature can significantly shorten the operating life of a laminated porous turbine vane. The test vanes were identical in design with vanes which had previously shown no signs of distress after 88 hr of steady-state operation at elevated gas temperatures. However, after approximately 6 hr of exposure to repeated cyclic variations in gas temperature, the present test vanes failed in low cycle thermal fatigue.

Several observations relative to the vane design, cyclic test, and the posttest analysis are pertinent:

- The turbine vanes tested reflected a number of design features which were imposed by operating requirements specified in an earlier program.[4] In particular, the porous-wall permeability distributions and the highly reinforced side-wall sections would be expected to adversely affect tolerance to low cycle thermal fatigue.
- The predicted thermal response of the airfoil skin (to the cyclic variation in gas temperature) indicated that severe transient excursions in chordwise metal temperature distribution occurred. The transient metal temperature excursions, in turn, would be expected to induce alternating longitudinal compressive and tensile strains in the leading-edge region. The quantitative evaluation of these effects resulted in a predicted low cycle fatigue failure (initiation of a transverse crack) after approximately 140 cycles of operation. This is in good agreement with the observed failures, which were first noted after 110 cycles of operation.
- Based on detailed metallographic analysis, the principal failure mechanism was determined to be low cycle thermal fatigue. This is consistent with the thermal/structural analysis which indicated that transverse strains were less than 25% of the corresponding longitudinal values. This behavior is attributed primarily to the fact that the airfoil is much more flexible in the transverse direction (bending about a longitudinal axis). Consequently, the longitudinal strains (induced by chordwise temperature excursions) would be expected to initiate failure (transverse cracks). The observed longitudinal cracks (in test vane No. 2 only) are considered to be either secondary failures or the result of damage incurred during fabrication.
- Significantly, the posttest inspection and metallographic analysis revealed no evidence of delamination (bond failure) in any of the test vanes. This is an important finding, because one of the test objectives was the evaluation of structural (bond) integrity in vanes subjected to severe cyclic excursions in normal (z direction) temperature gradients. Normal temperature gradients in test vane No. 3, for example, varied from approximately zero to 250°F (139°C) during a typical cycle. Although these conditions would be expected to produce very large thermally induced shear loads at the bond surfaces, no evidence of bond failure was observed.
- The severity of the gas temperature transient excursions contributed significantly to early low cycle fatigue failure of the vanes. The gas temperature change during a typical cycle extended over a range of some 1600°F (889°C) and occurred at a rate of almost 900°F

(500°C) per second. While this rate of gas temperature change is comparable with that experienced in current production engines (e.g., T56-A-15), the range over which the change occurred is two to four times greater. This is, of course, directly reflected in the extreme excursions in airfoil chordwise temperature distribution shown in Figures 56 and 57.

- Temperature gradients through the airfoil wall in the surface normal (z) direction were found to have only a modest influence on low cycle fatigue life. In the leading-edge region, normal temperature gradients tend to reduce the large compressive strains induced by surface temperature nonuniformity during the high gas temperature portion of the cycle. Furthermore, normal temperature gradients result in lower metal temperature levels at the inner laminates, thus increasing the strength of these elements of the wall. During the low temperature portion of the cycle, the magnitude of the normal temperature gradient was found to be negligibly small.
- Although a number of improvements could be made, the cascade test apparatus and associated instrumentation provided a good quantitative measure of the actual operating conditions. The availability of reasonably accurate gas stream and airfoil temperature data, together with transient operational data, permitted a credible posttest analysis of the airfoil structural behavior. The latter analysis should be emphasized because the ability to predict airfoil life is essential to the realistic design of high temperature turbine components.

Several recommendations related to future design and evaluation of laminated porous wall airfoils are based on the foregoing observations. Because the tolerance of any airfoil to low cycle thermal fatigue is largely influenced by thermomechanical design, the following design modifications are indicated.

- Jet impingement combined with chordwise finned channel cooling in the leading edge/suction surface region could potentially reduce the severe chordwise surface temperature variation typical in this region on transpiration-cooled vanes. This behavior in transpiration-cooled vanes is attributable to an inability to vary wall permeability continuously in a region where external static pressures are changing very rapidly. Any reduction in chordwise thermal gradient in this region will have a favorable effect on low cycle thermal fatigue life. Furthermore, an impermeable impingement-cooled leading edge is consistent with high-temperature engine design practice. In an engine, the use of transpiration cooling on the leading edges of the first-stage vanes is usually precluded by the very small driving pressure difference available at that point on the airfoil. In this respect, a modified design of the type proposed represents a more logical candidate for practical engine hardware.
- The use of channel cooling with trailing-edge discharge in the rear portion of the airfoil would permit more effective trailing-edge cooling as well as a more aerodynamically effective coolant discharge pattern. The flow of coolant directly through trailing-edge channels should eliminate the increase in trailing-edge temperatures evident in transpiration-cooled airfoils with welded trailing edges.

- The application of porous-wall cooling with near-tangential surface injection would help reduce aerodynamic penalties associated with normal coolant injection. Porous-wall cooling can be most effectively applied along the side wall region because the external static pressure variation is smallest there. Combined with the nearly isothermal convection cooling of the leading and trailing edges, a hybrid convection/transpiration cooling design should therefore result in a reasonably isothermal surface. Surface temperature uniformity, in turn, will be manifested in improved low cycle thermal fatigue life.
- By making the extent and thickness of internal stiffening sheets consistent with operational rather than test rig emergency* requirements, a more equitable distribution of wall stiffness will be achieved. This should reduce the effects of side-wall load transfer to the thinner leading-edge region considerably. In addition, reduced overall wall thickness in the side-wall regions will reduce the thermal inertia of this wall section. Consequently, the transient thermal "lag" of the side walls relative to the leading edge could be significantly reduced. The net effect of this modification would again be improved airfoil low cycle thermal fatigue life.
- Utilization of proved hot creep forming techniques during fabrication should help eliminate residual stresses and/or surface cracks attributable to the forming operation.

In future designs of porous-wall airfoils, the transient thermal response (and resultant induced strain range) should be predicted for any anticipated transient operation. Although analytical life prediction techniques still require considerable development, the results reported herein are encouraging enough to justify the use of such tools in engineering design analysis. These techniques can also be utilized to establish the relative effects of changes in gas temperature level (both rate and range). In some cases, a combination of design modifications with control of gas temperature excursion may be necessary to achieve acceptable low cycle fatigue life.

Finally, improvements to temperature measurement systems would enhance future experimental evaluation efforts. More extensive use of airfoil thermocouples is indicated, particularly in light of the short life of such instrumentation. Also, additional thermocouples would permit better experimental definition of chordwise metal temperature distribution. Since thermocouple output can be readily monitored on strip chart recorders, it should be possible to directly measure the transient chordwise temperature response during a cascade test. Attempts should also be made to extend the range of the infrared photographic techniques used in this program. For example, at metal temperature levels below 1000°F (538°C), variations in film density were not discernible because of the low radiant energy levels. With appropriate changes in film, camera setting, and exposure time, low temperature measurements should be possible.

*The sidewall reinforcement of the present vanes was based on survival of an emergency cascade rig shutdown. This condition, unique to the cascade facility, is considerably more severe (in terms of pressure excursions) than in engine operation.

LIST OF SYMBOLS

A_1, A_2, A_3, A_4	Effective thermal conduction areas in the spanwise/chordwise directions
Cp_c	Mean coolant specific heat within porous wall
Cp_m	Specific heat of porous wall material at temperature T_m
d_i	Hole diameter
e	Etch depth
G, G_c	Coolant flow rate per unit surface area; also referred to as injection rate
g	Gravitational constant
h_g	Local external airfoil surface film coefficient
h_i	Effective internal airfoil surface film coefficient, defined as $G_c\ Cp_c\ \eta$
k_m	Thermal conductivity of porous wall material
k_1, k_2, k_3, k_4	Effective porous wall thermal conductivities in directions 1 through 4 as defined in Figure 52
P	Porosity (void volume/total volume) of porous wall
P_1	Coolant static pressure inside vane cavity (upstream of porous wall)
P_2	Static pressure at porous wall external surface (downstream of porous wall)
q_c	Net conduction heat transfer rate, defined in Equation (3)
R	Gas constant
s	Hole spacing in outer laminate
T	Mean temperature of coolant inside porous wall; refer to Equation (1)
T_c	Coolant plenum (supply) temperature
ΔT_c	Coolant temperature rise in passing through porous wall
T_g	Local gas stream recovery temperature
$T_{i,j}$	Wall surface temperature at any node (i, j) of finite difference network (see Figure 53)
T_m	Mean airfoil wall temperature at any x, y location
T_o	Wall temperature at inside (coolant) surface
T_w	Local airfoil surface temperature

t	Time
Δt	Time increment for finite difference thermal response calculation
W	Mass flow
x	Axial (chordwise) distance coordinate*
y	Radial (spanwise) distance coordinate*
$\Delta x, \Delta y$	Chordwise/spanwise node dimensions as defined in Figure 53
Z'	Average heat transfer area-to-volume ratio of porous wall
z	Distance coordinate in direction normal to airfoil surface*
α	Viscous resistance coefficient
β	Inertial resistance coefficient
η	Porous wall thermal effectiveness, defined as $\Delta T_c/(T_w-T_c)$
μ	Coolant mean viscosity inside porous wall
ρ_m	Density of porous wall material at temperature T_m
τ	Porous wall thickness
τ_o	Wall thickness on which α and β are based

*Except as used in Figure 63.

REFERENCES

1. Anderson, R. D. and Nealy, D. A. Evaluation of Laminated Porous Material for High Temperature Air-Cooled Turbine Blades—Final Report, Tasks I and II. NASA CR-72281. January 1967. (Unclassified)

2. Nealy, D. A. and Anderson, R. D. Heat Transfer Characteristics of Laminated Porous Materials. (U) Air Force Systems Command. AFAPL-TR-68-98. August 1968. (Confidential)

3. Anderson, R. D., Davis, W. C., McLoed, R. N., and Nealy, D. A. High Temperature Air-Cooled Turbine Blades. (U) Air Force Systems Command. AFAPL-TR-69-41 (1969). (Confidential)

4. Nealy, D. A., Anderson, R. D., and Hufford, A. A. Design and Experimental Evaluation of a Turbine Vane Fabricated From Laminated Porous Material. NASA CR-72649. July 1969. (Unclassified)

5. Whitney, W. J., Szanca, E. M., Moffitt, T. P., and Monroe, D. E. Cold-Air Investigation of a Turbine For High-Temperature Engine Application. NASA TN-D-3751. January 1967. (Unclassified)

6. NASA Contract NAS3-7913. (Unclassified)

7. Goodbar, W. L. An Improved Method for Measuring Turbine Vane Temperature in Hot Cascade Rigs. AIAA Paper No. 66-642, AIAA 2nd Propulsion Joint Specialist Conference. June 1966. (Unclassified)

8. Green, L. Jr. and Duwez, P. "Fluid Flow Through Porous Metal." Journal of Applied Mechanics (ASME). Vol 18, No. 1 (1951), pp 39-45. (Unclassified)

9. Peaceman, D. W. and Rachford, H. H., "The Numerical Solution of Parabolic and Elliptic Differential Equations." Journal of Industrial and Applied Mathematics. Vol 3 (1955), p 28. (Unclassified)

10. Douglas, J. Jr. and Peaceman, D. W. "Numerical Solution of Two-Dimensional Heat Flow Problems." AIChE Journal. Vol 1, No. 4 (1955), p 505. (Unclassified)

11. Nealy, D. A. and Anderson, R. D. Design of a Strut Supported Turbine Vane With a Wire-Form Porous Shell. NASA CR-72508. July 1968. (Unclassified)

12. Peterson, R. E. Stress Concentration Design Factors. New York: John Wiley and Sons, 1953. (Unclassified)

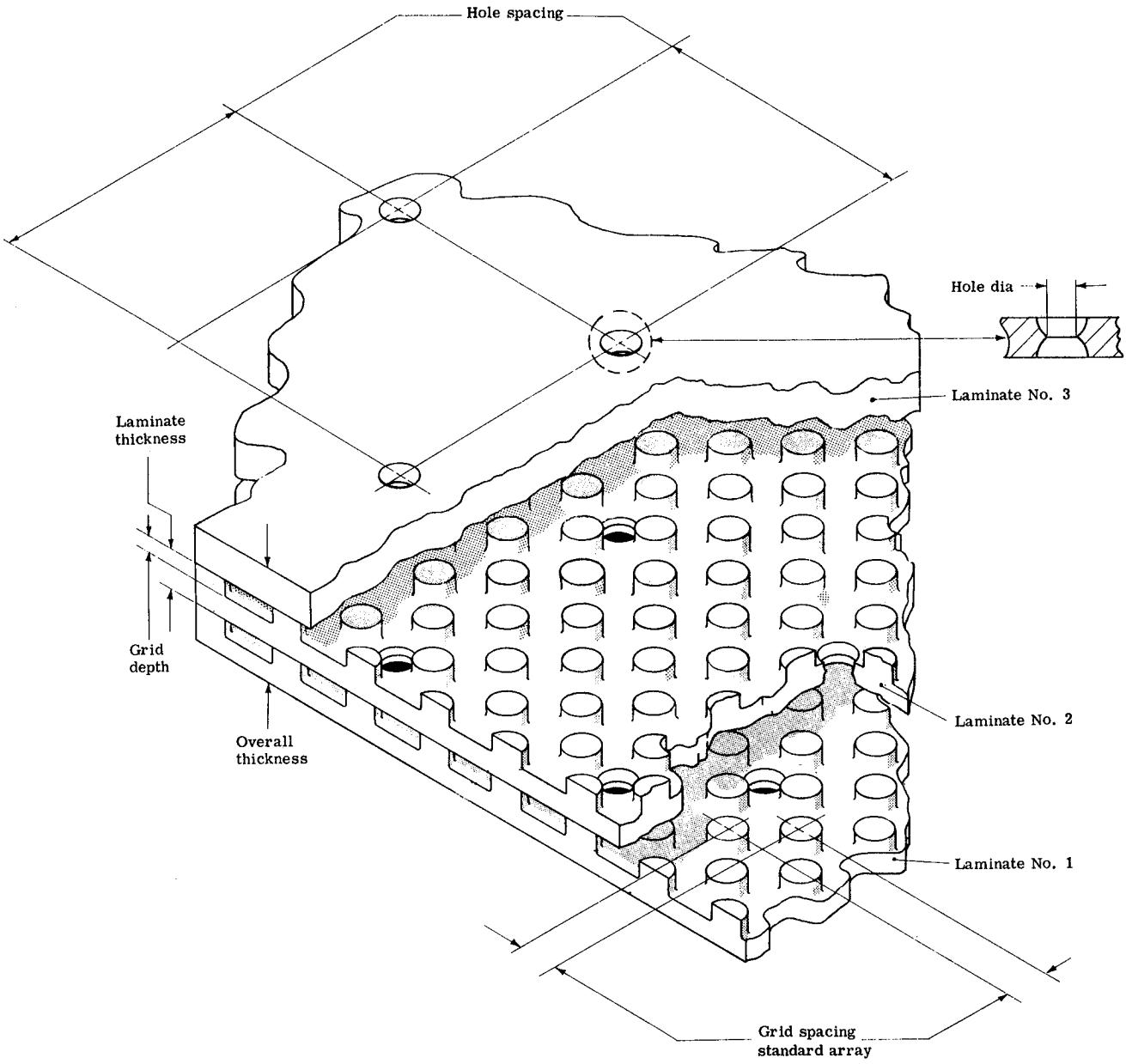

Figure 1. Schematic of typical Lamilloy porous material configuration.

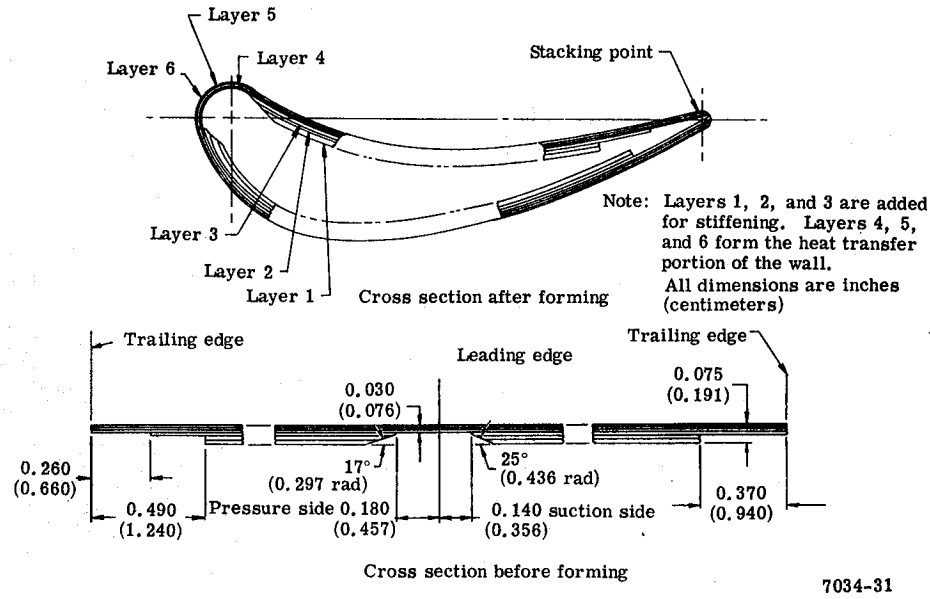

Figure 2. Cross section of Lamilloy porous material vane.

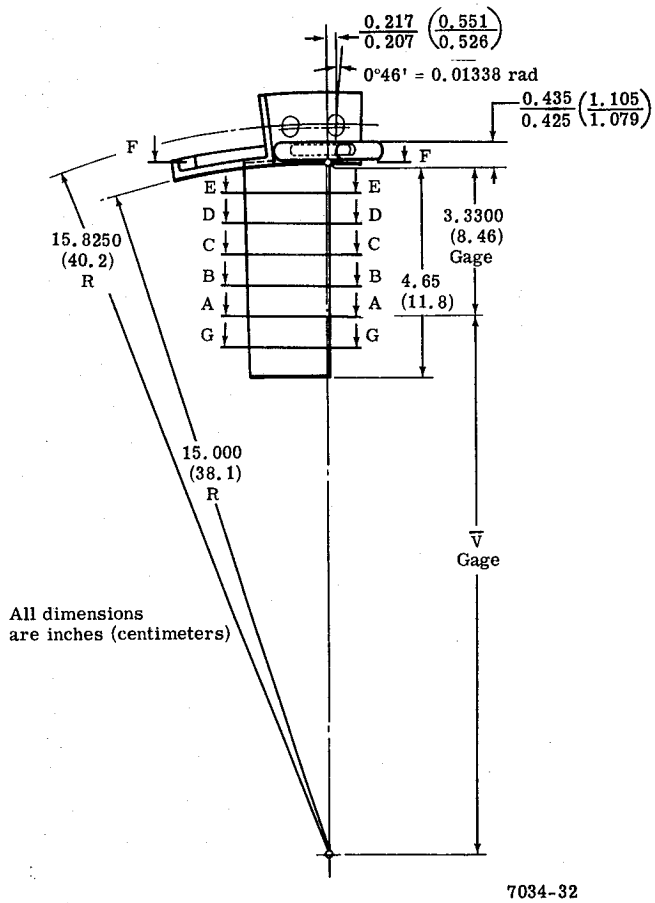

Figure 3. Lamilloy porous material vane dimensions and location of sections used in Table I to define airfoil shape. (See Figure 4 for dimensions.)

Section*	A-A	B-B	C-C	D-D	E-E	F-F	G-G
Z ± 0.010 (in.)	2.222	2.244	2.266	2.288	2.309		
± 0.03 (cm)	5.64	5.70	5.76	5.81	5.86		
γ	45°12'	44°42'	44°12'	43°42'	43°13'	42°44'	45°42'
(rad)	0.789	0.780	0.771	0.762	0.754	0.746	0.798
$\overline{V}$ (in.)	11.67	12.33	13.00	13.67	14.33	15.00	11.00
(cm)	29.6	31.3	33.0	34.7	36.4	38.1	27.9
L ± 0.005 (in.)	0.482	0.492	0.502	0.509	0.515		
± 0.01 (cm)	1.22	1.25	1.28	1.29	1.31		
Q ± 0.005 (in.)	0.334	0.335	0.337	0.340	0.342		
± 0.01 (cm)	0.85	0.85	0.86	0.86	0.87		
R (in.)	0.175	0.175	0.175	0.175	0.175		
(cm)	0.45	0.45	0.45	0.45	0.45		
U (in.)	0.076	0.076	0.076	0.076	0.076		
(cm)	0.19	0.19	0.19	0.19	0.19		
S (in.)	0.050	0.050	0.050	0.050	0.050		
(cm)	0.13	0.13	0.13	0.13	0.13		

*From Figure 3

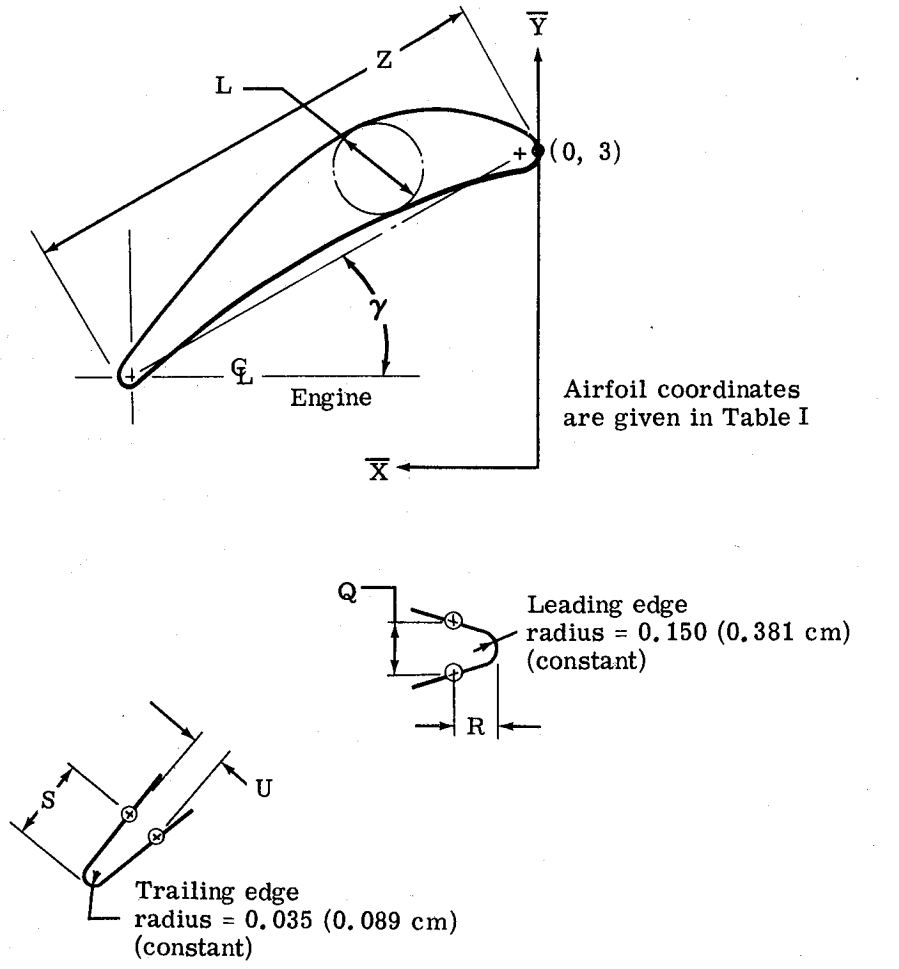

Figure 4. Airfoil dimensions and coordinate system definition.

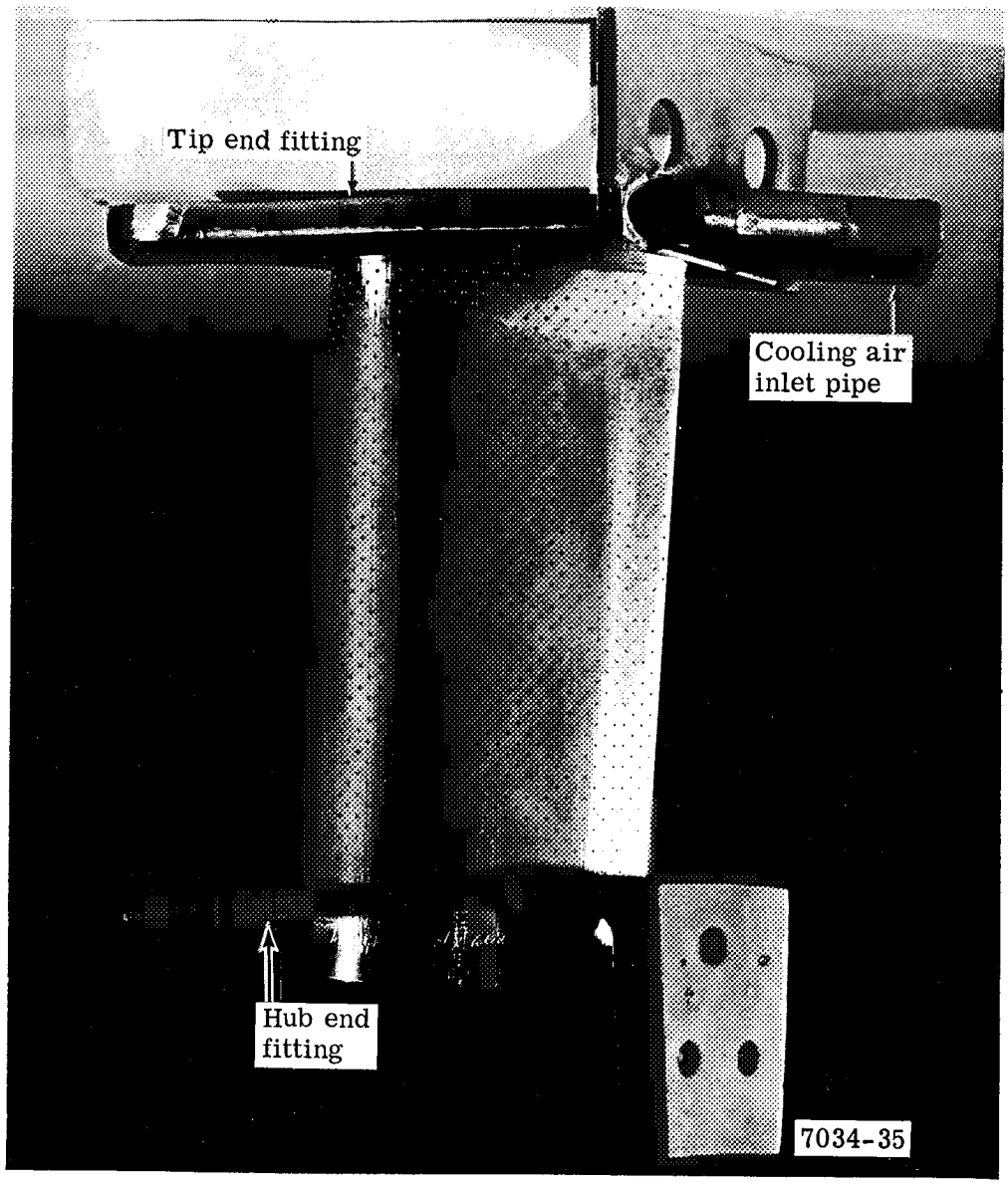

Figure 5. Lamilloy porous material vane—suction side.

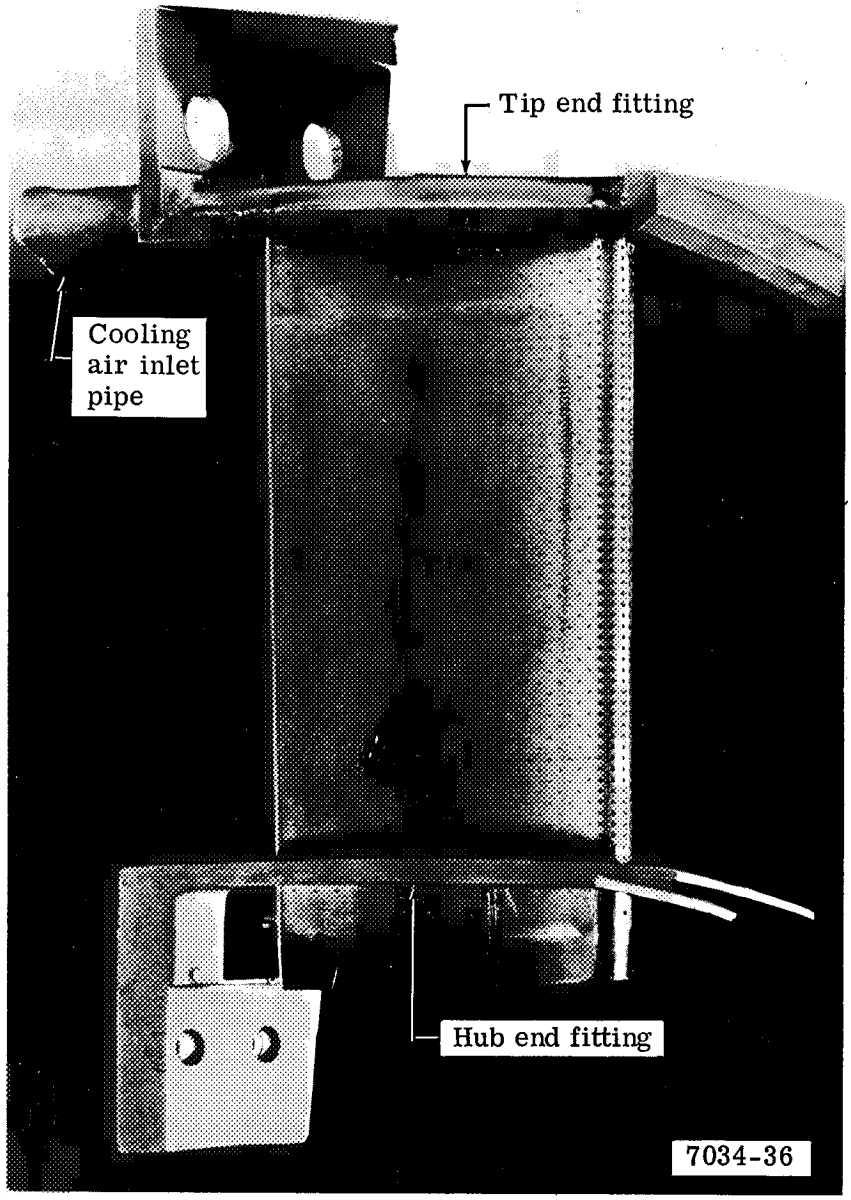

Figure 6. Lamilloy porous material vane—pressure side.

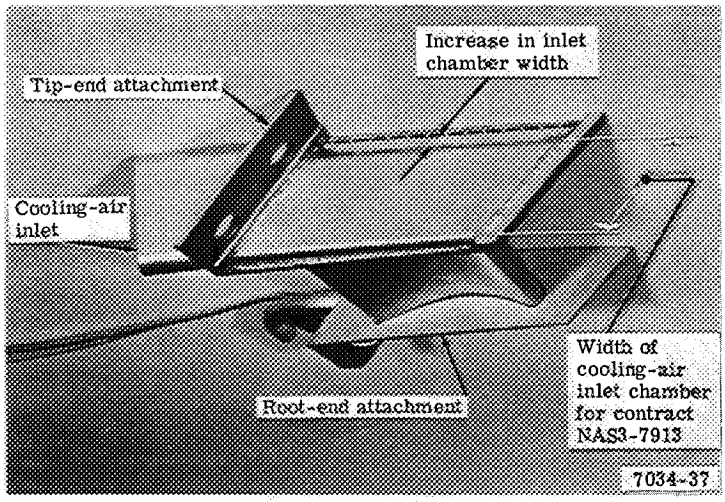

Figure 7. Cooling air plenum modification.

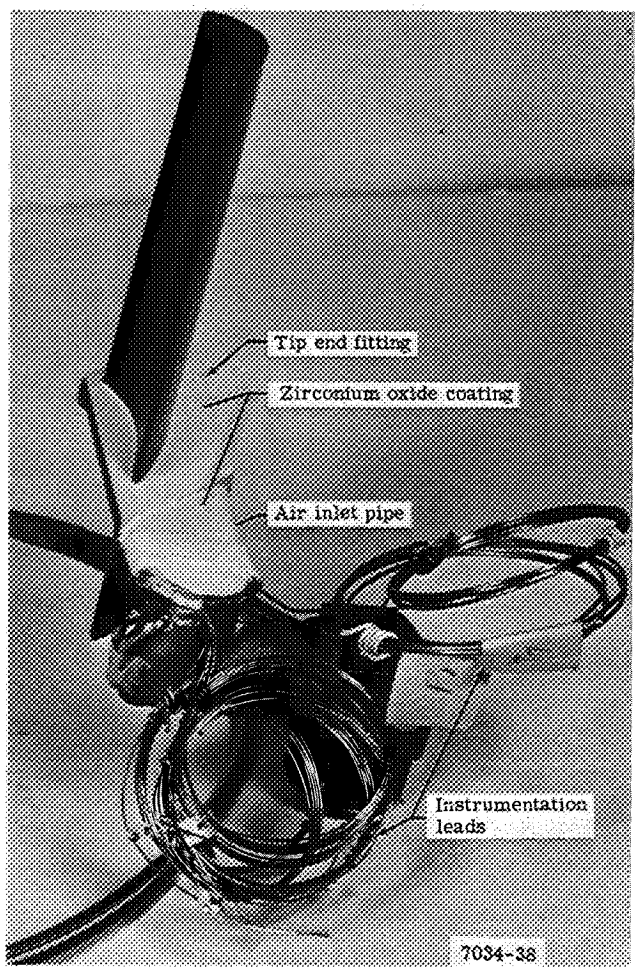

Figure 8. Vane end attachments coated with zirconium oxide.

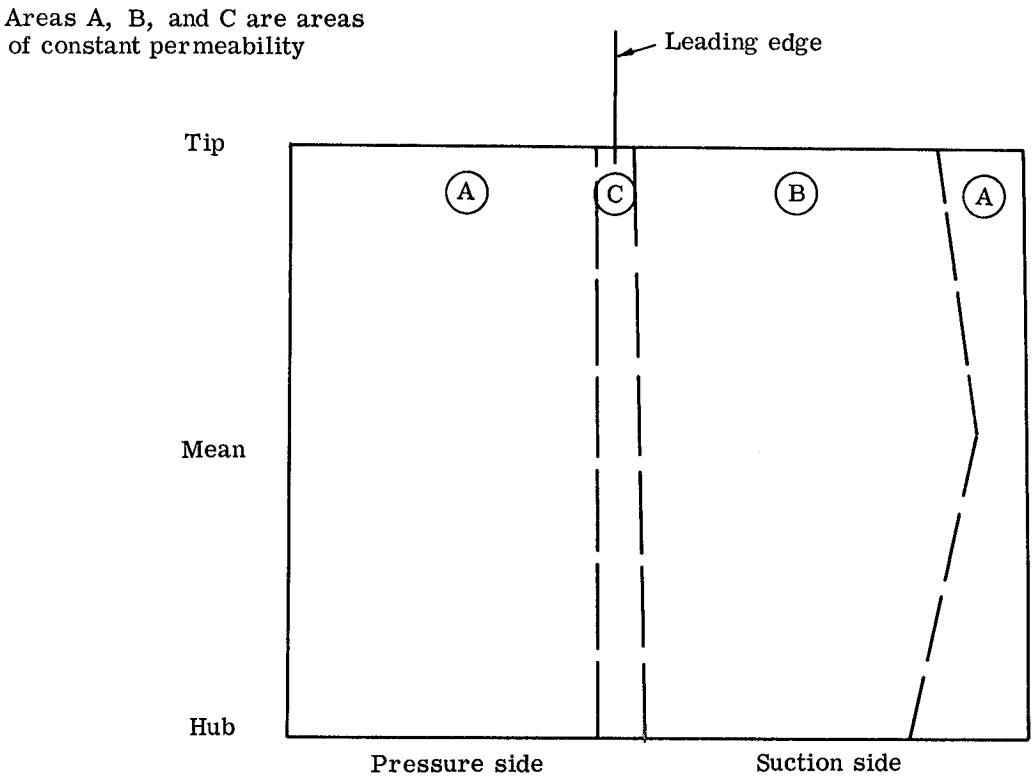

Figure 9. Developed view of airfoil showing permeability variations.

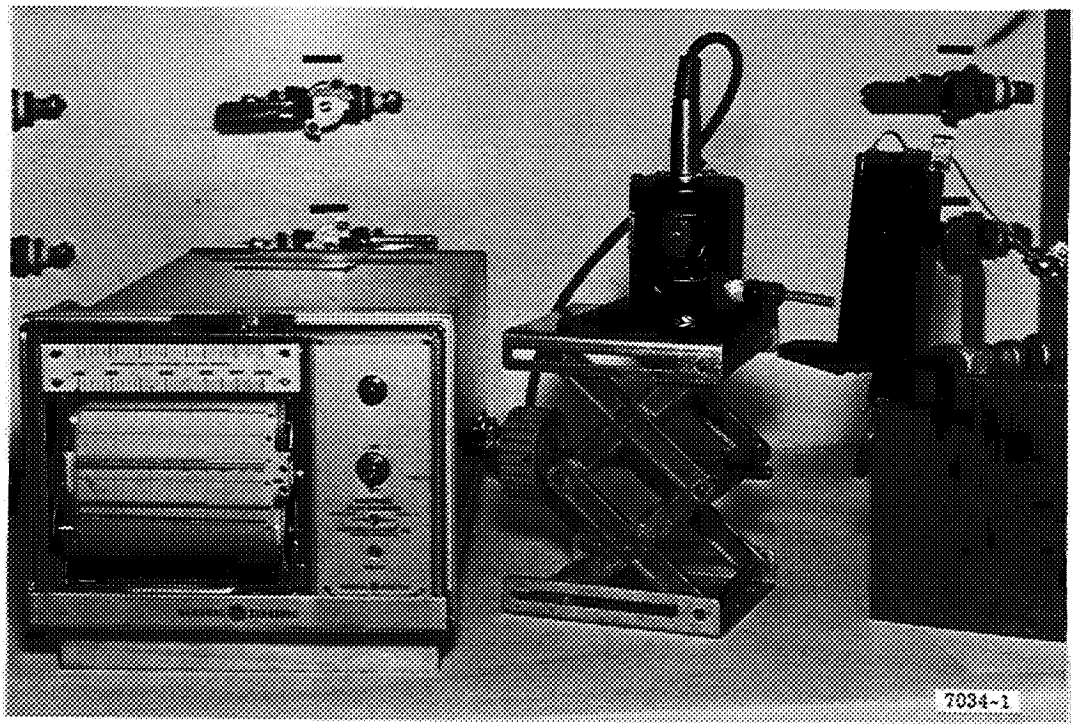

Figure 10. Permeability test apparatus used for measuring local flow.

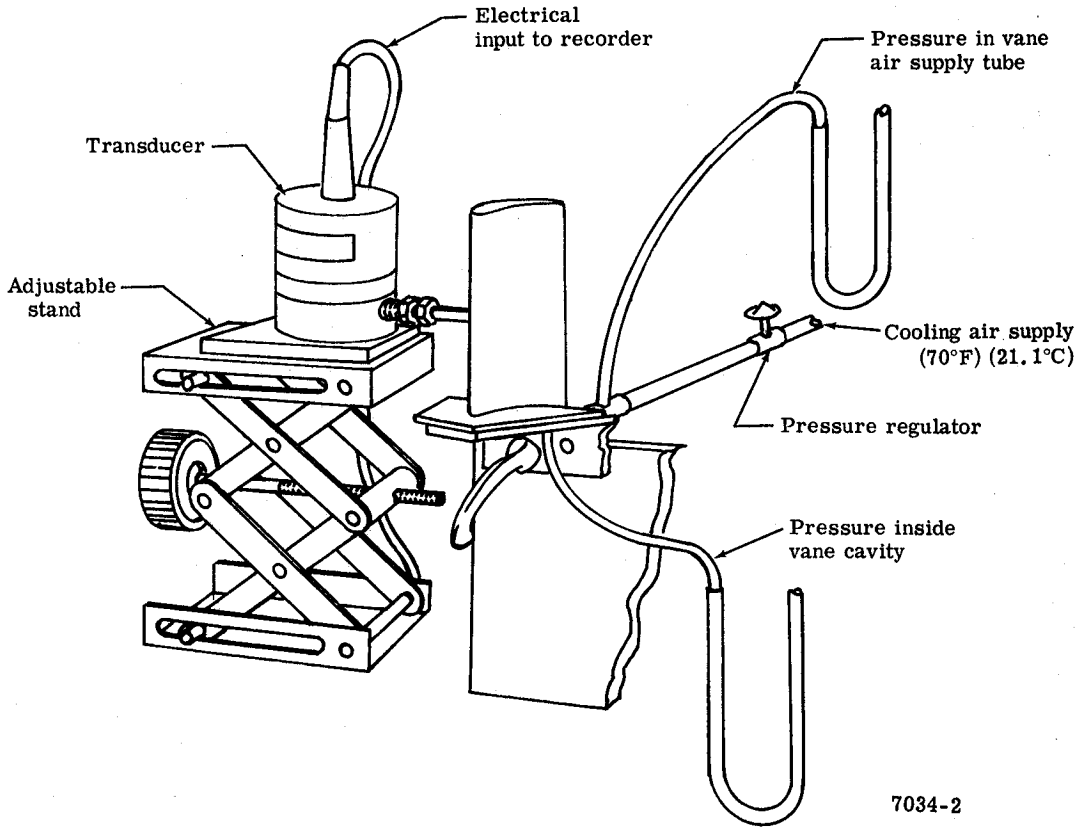

Figure 11. Schematic of permeability test equipment.

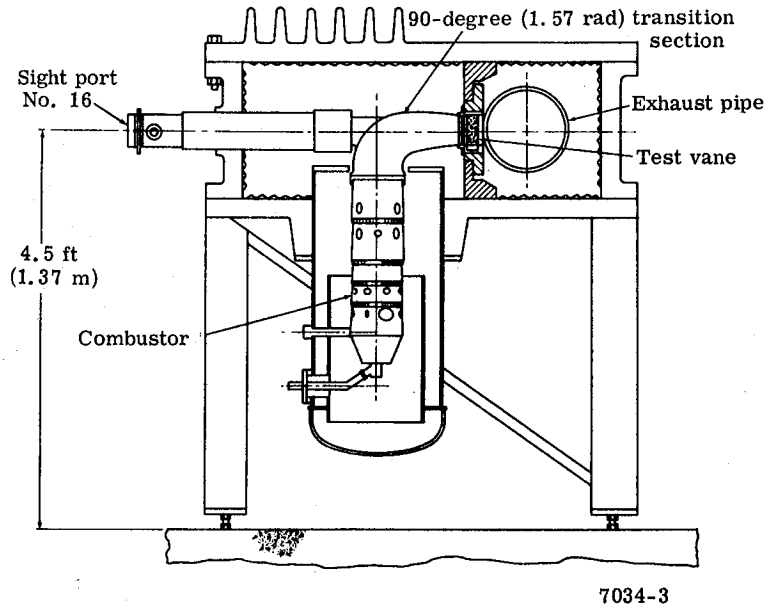

Figure 12. Schematic of hot cascade test facility—side view.

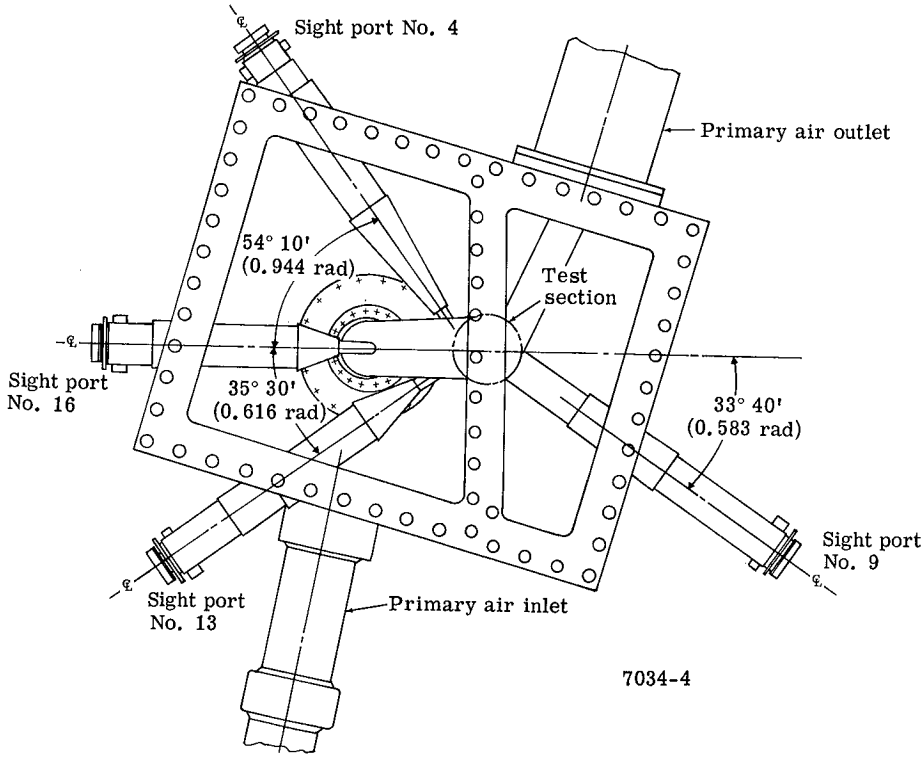

Figure 13. Schematic of hot cascade test facility—top view.

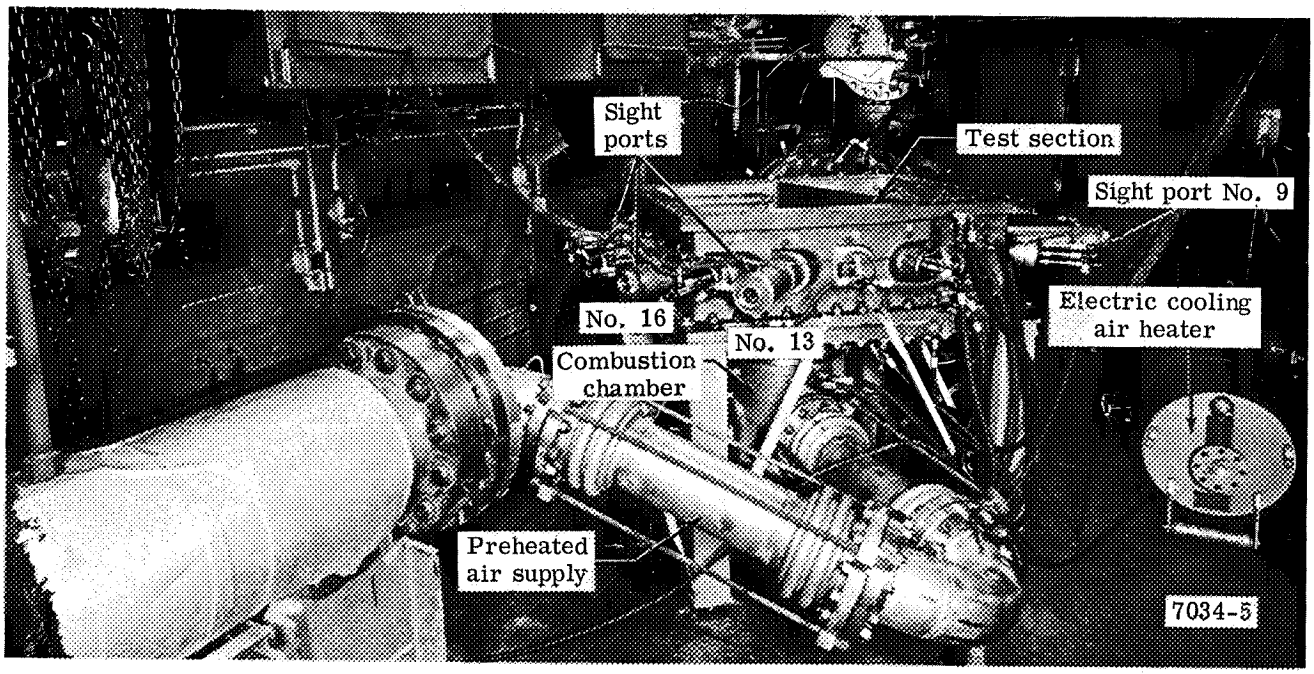

Figure 14. Hot cascade test facility.

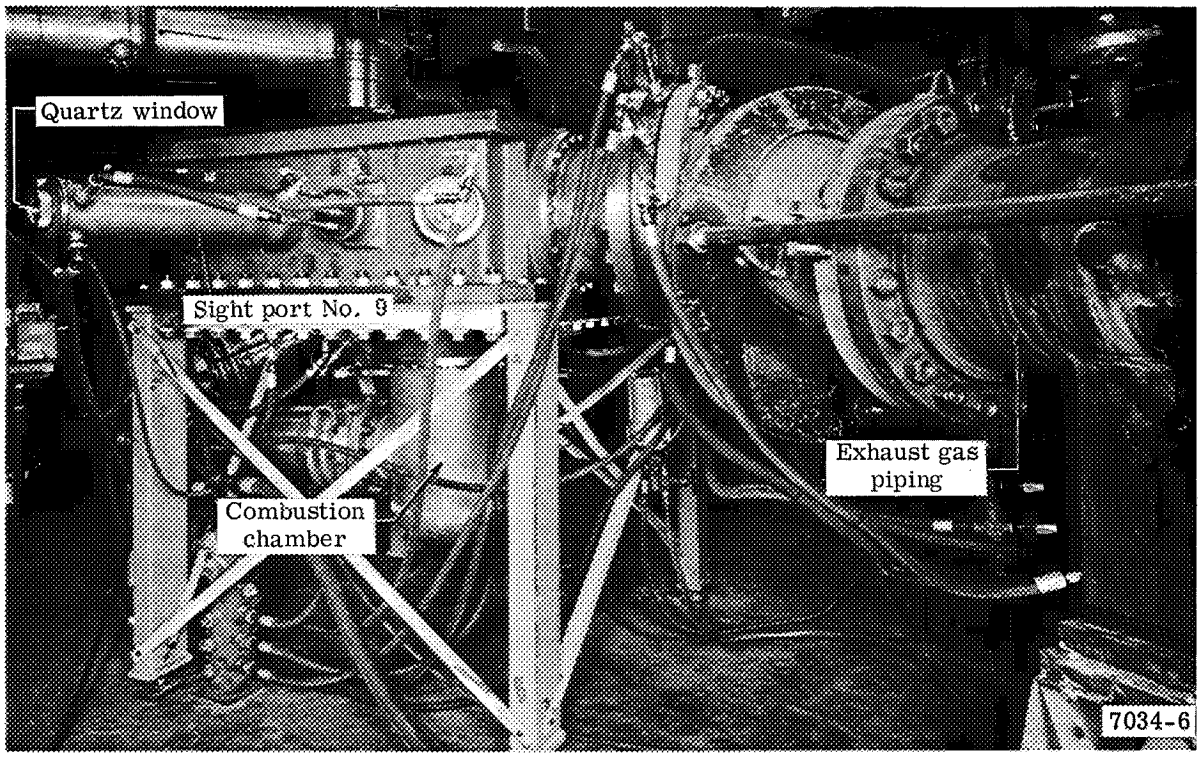

Figure 15. Hot cascade test facility.

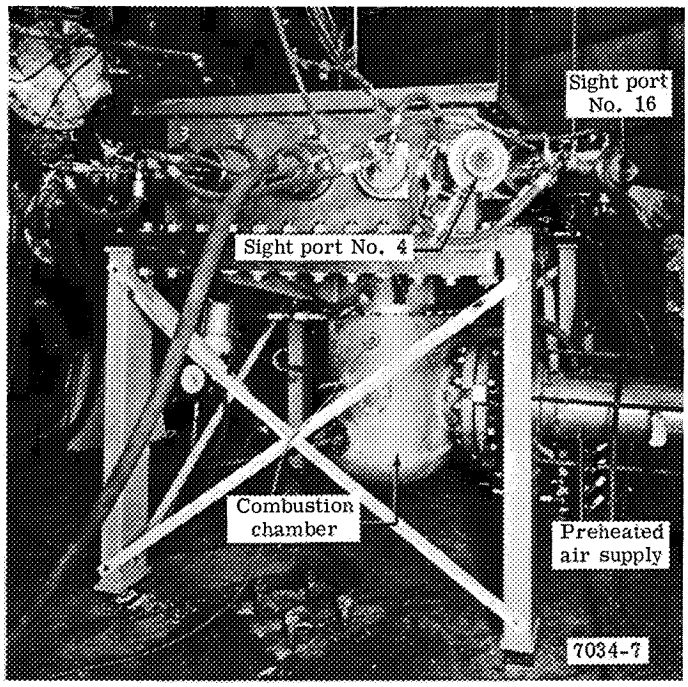

Figure 16. Hot cascade test facility.

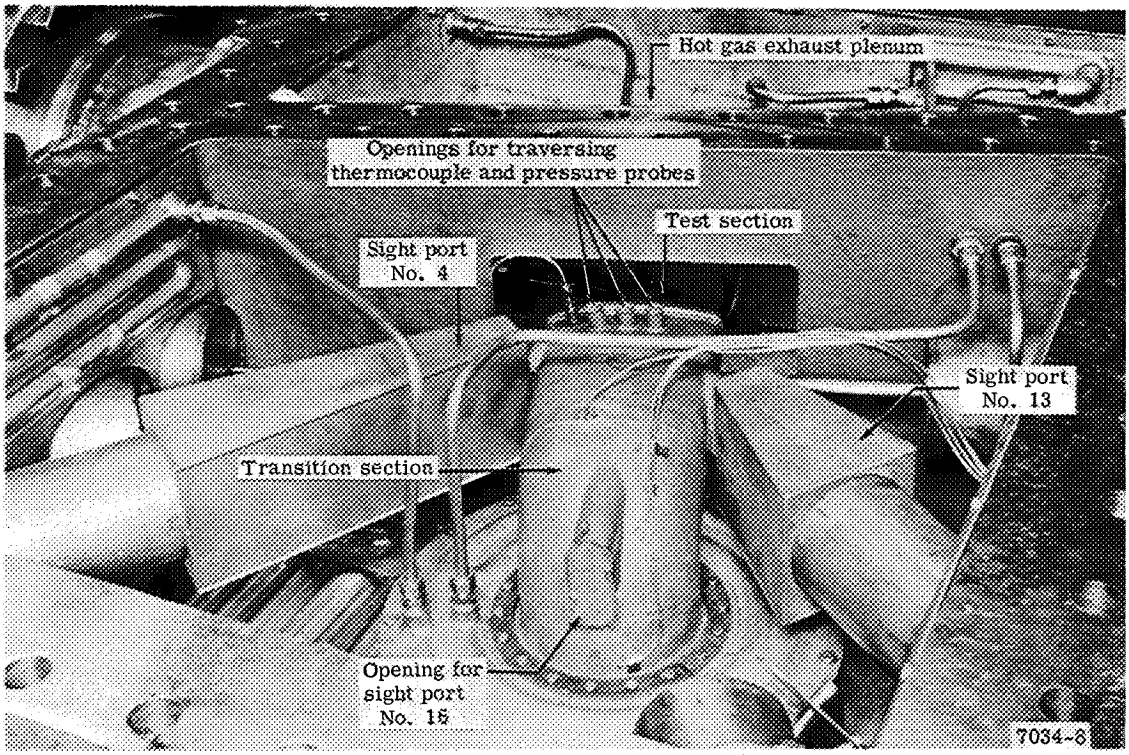

Figure 17. Hot cascade test facility with top removed to expose sheet metal gas transition section and sight port ducts.

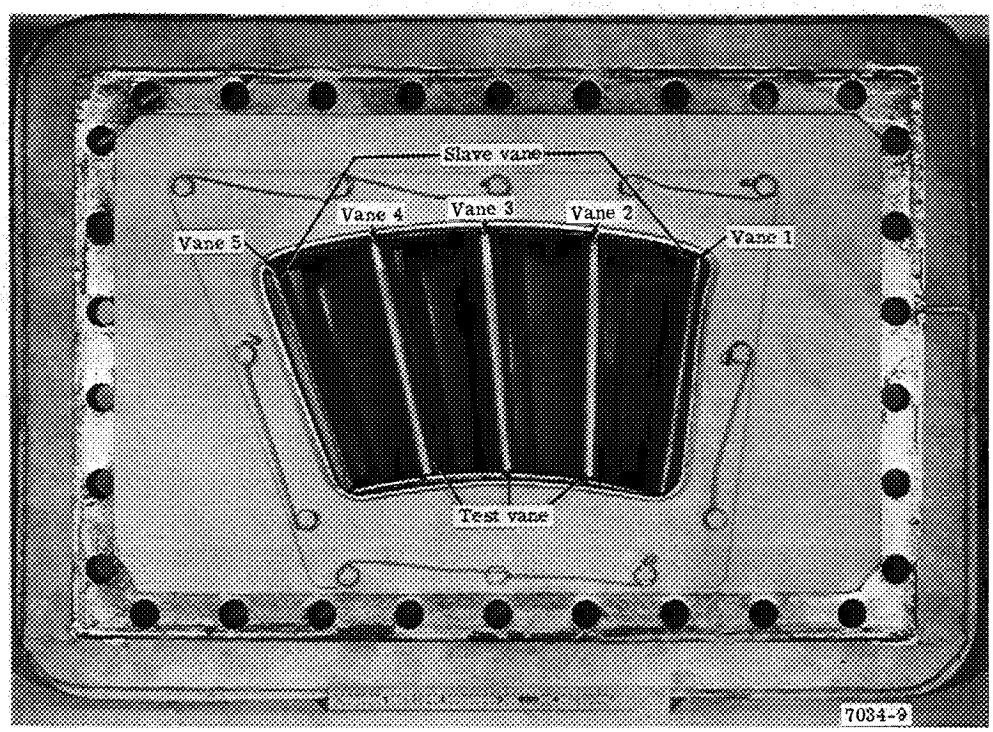

Figure 18. Test section leading edge view.

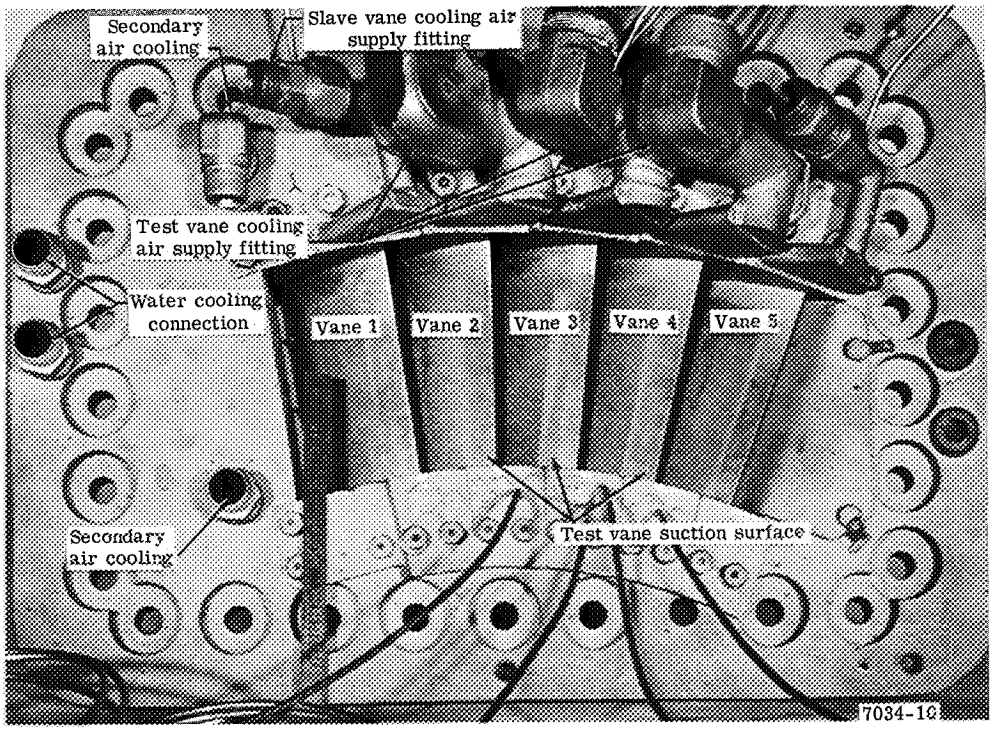

Figure 19. Test section trailing edge view.

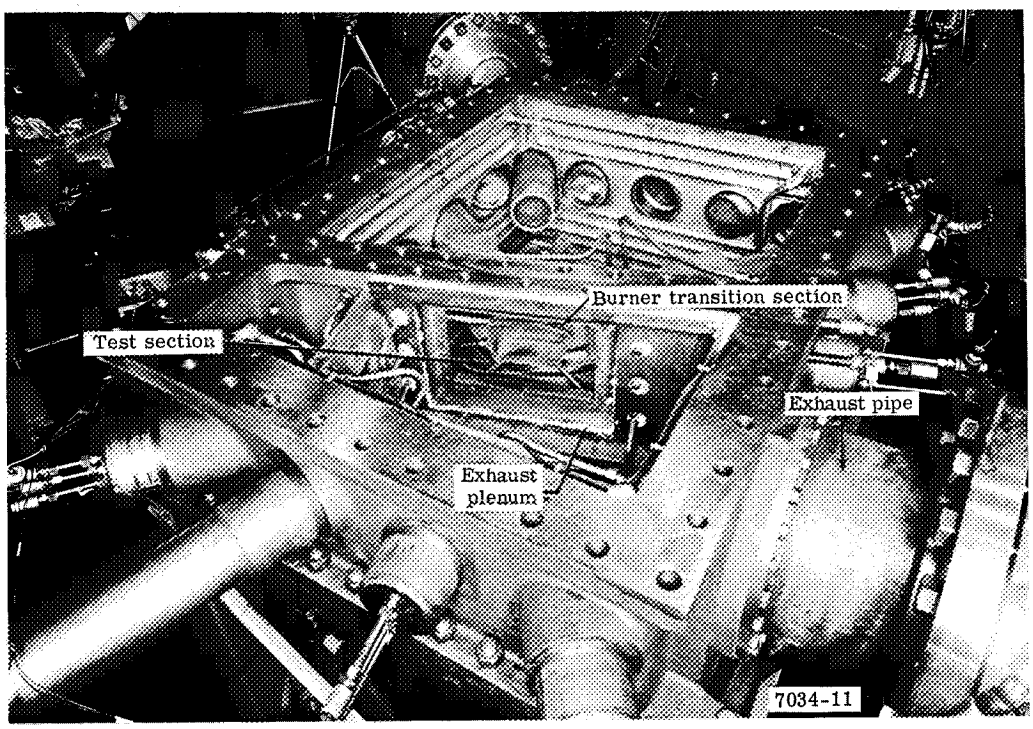

Figure 20. Hot cascade test facility with top frame and test section removed.

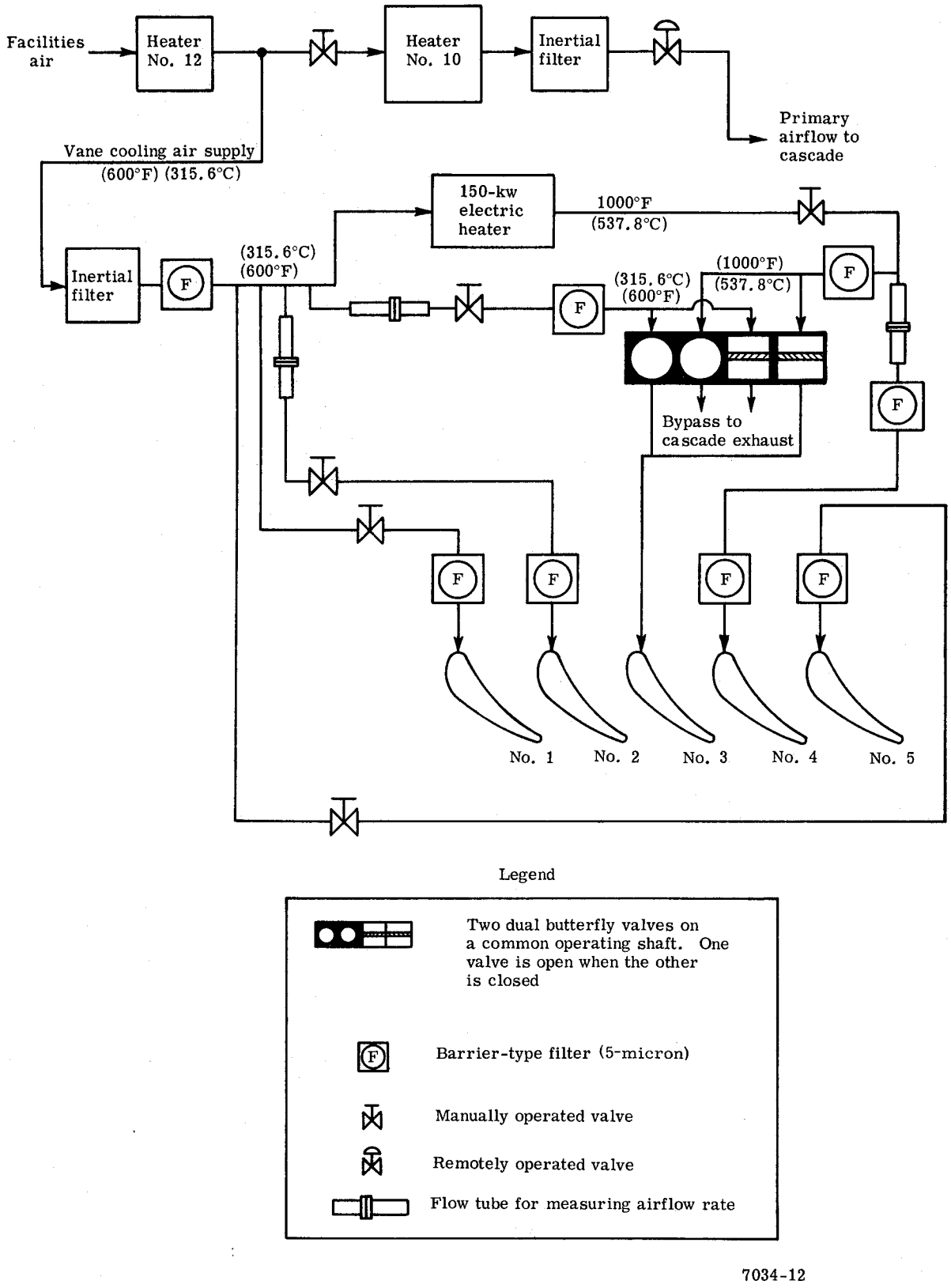

Figure 21. Schematic of vane cooling air system.

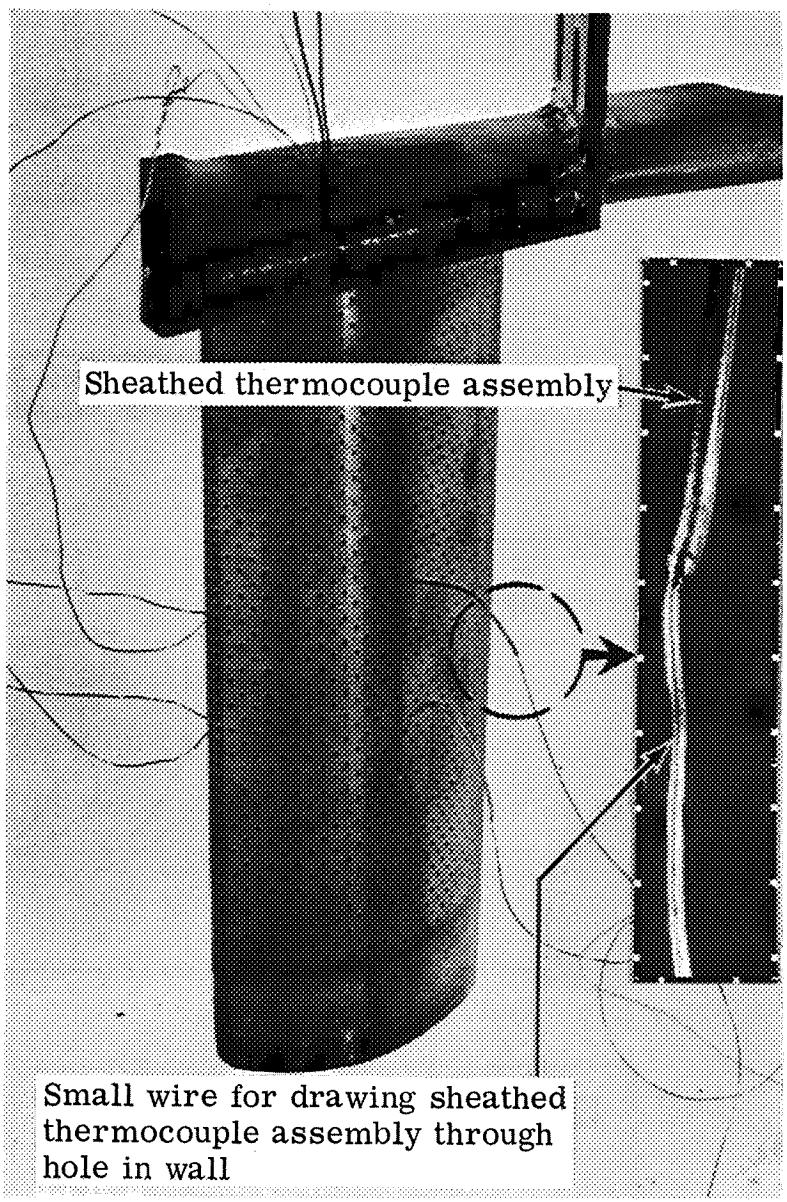

Figure 22. Thermocouple wires strung through vane cavity.

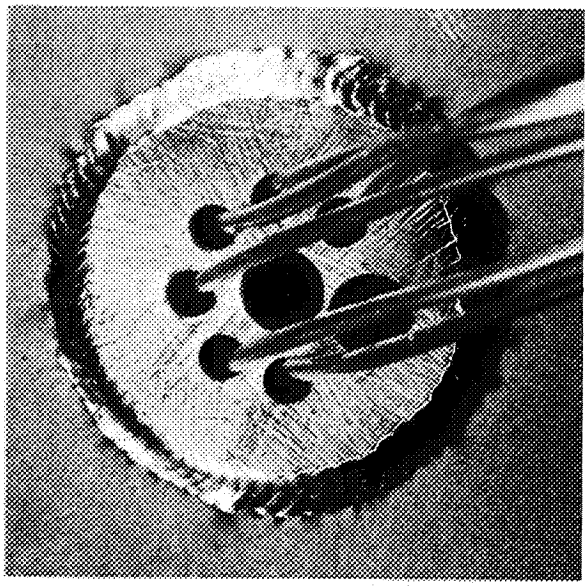

Enlarged view of laser-welded spacer (large holes provided for cooling air pressure and temperature probes)

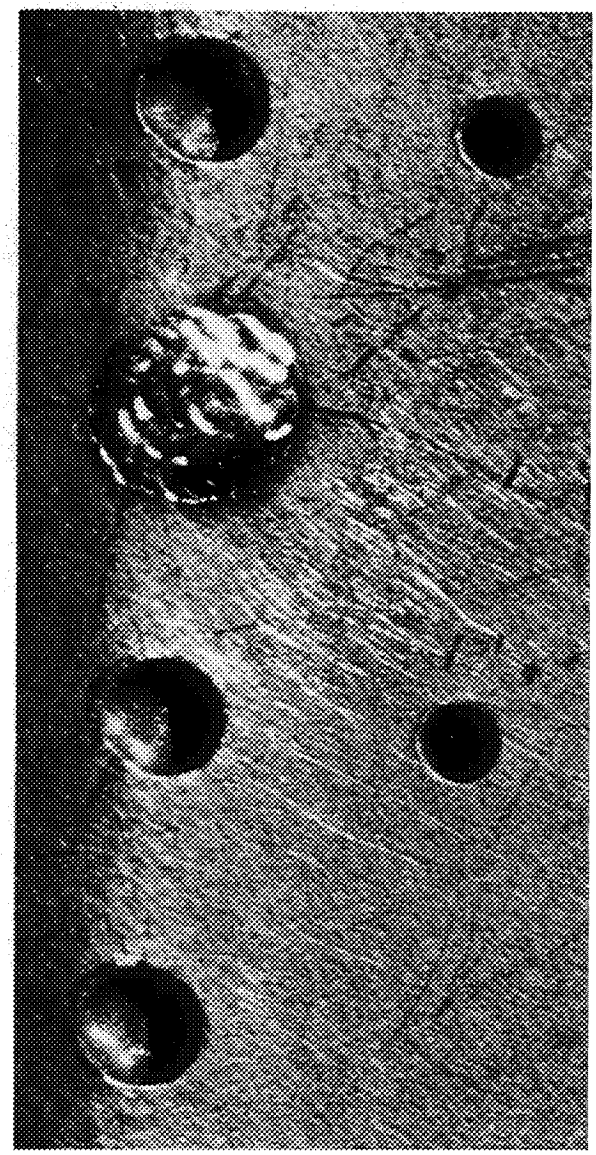

Enlarged view of thermocouple junction

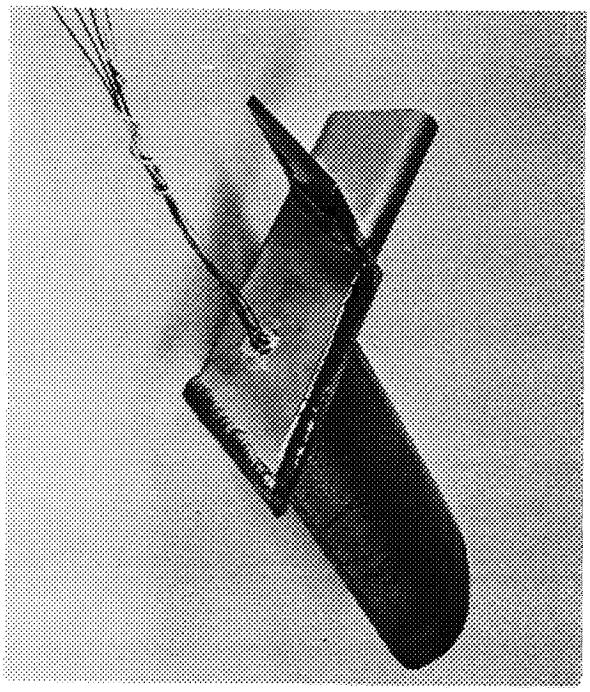

Thermocouple leads exit from top of vane

7034-14

Figure 23. Airfoil thermocouple details.

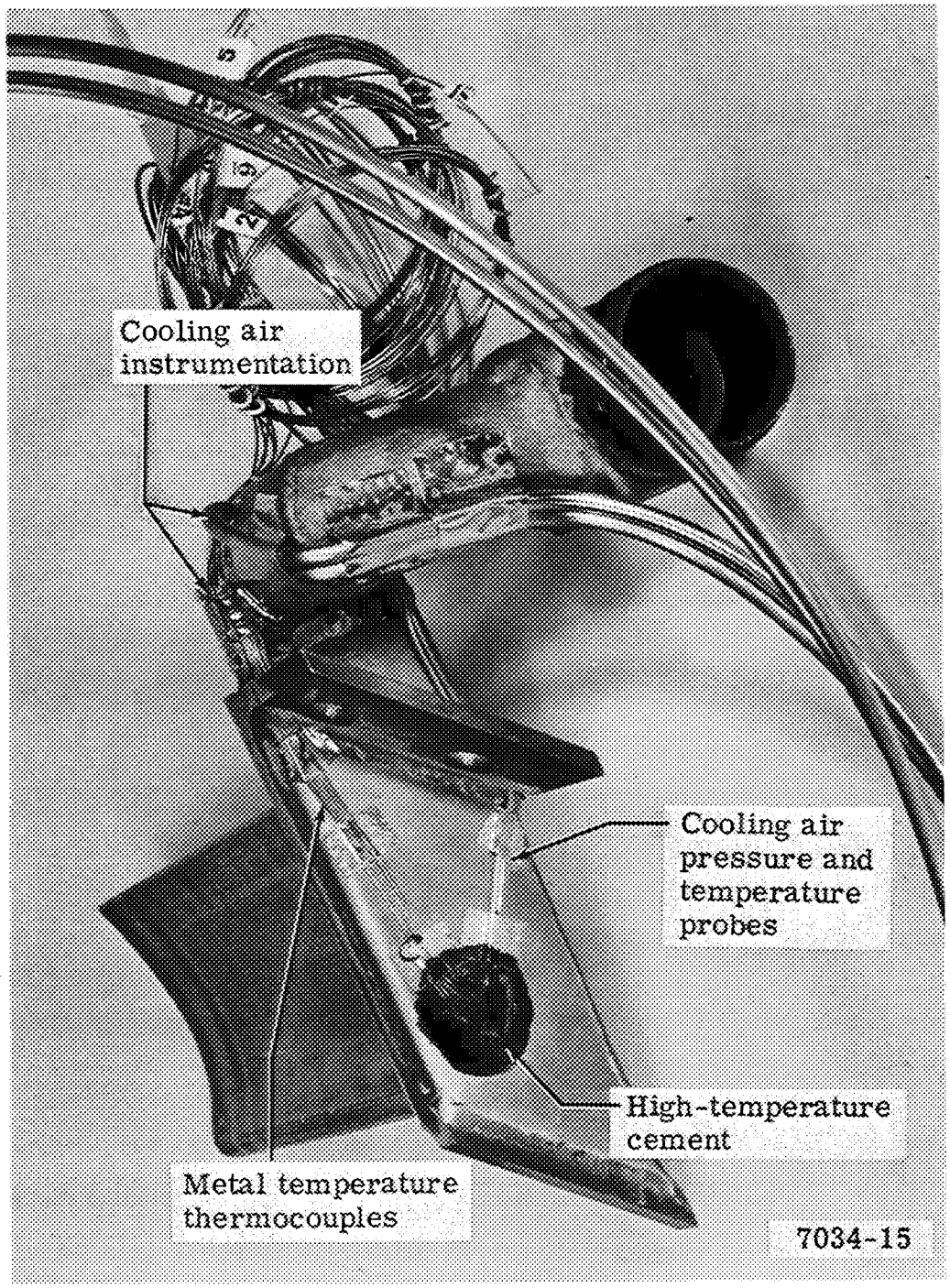

Figure 24. Instrumentation leads secured to vane flange and cooling air fitting.

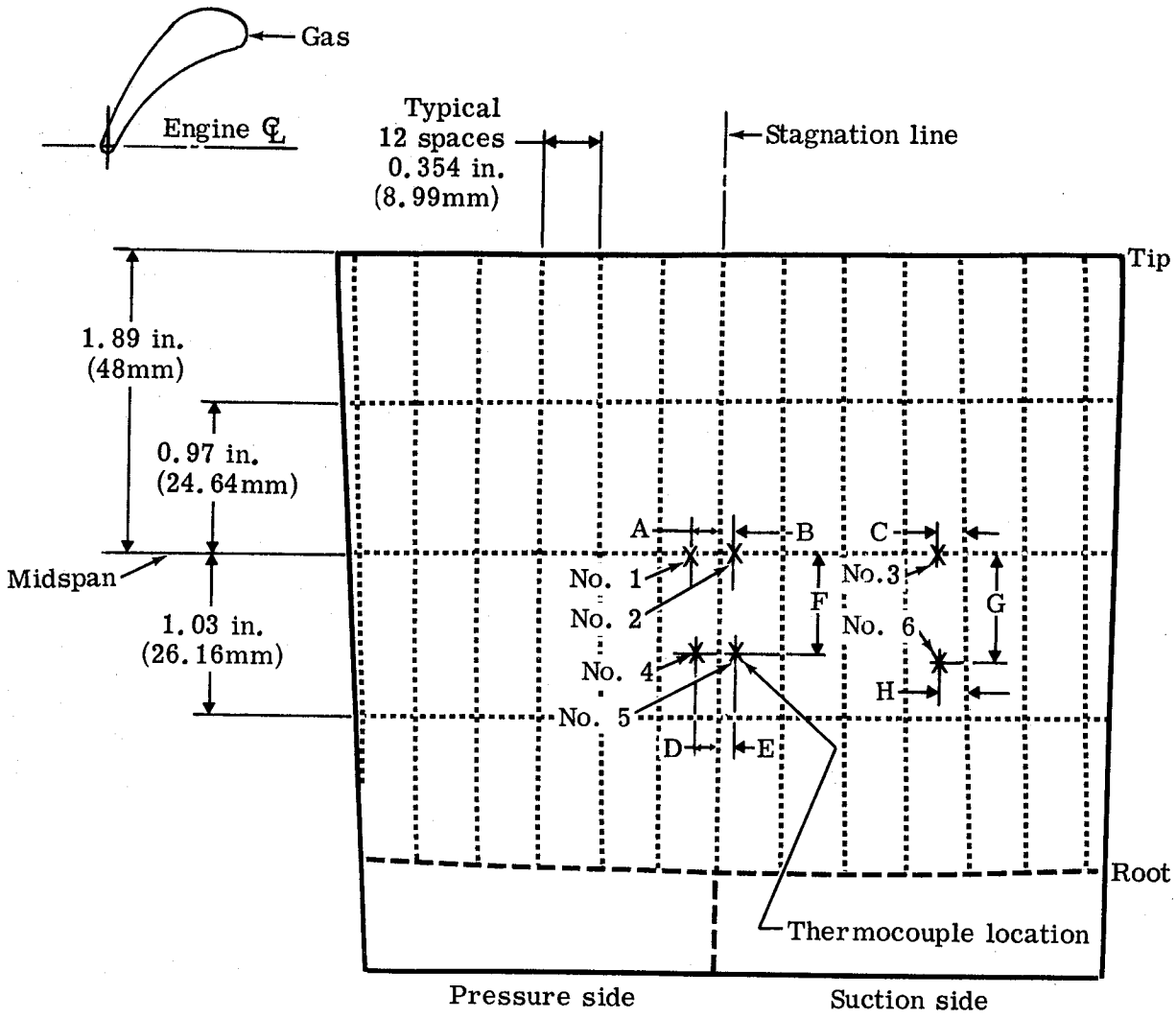

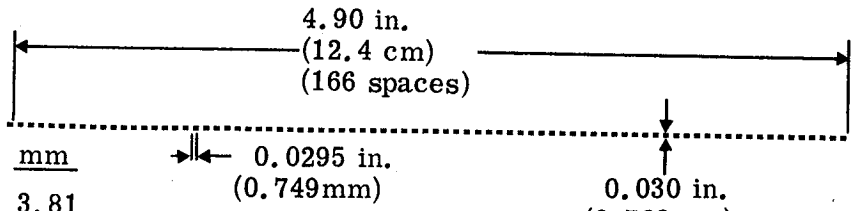

Dimension	in.	mm
A	0.15	3.81
B	0.10	2.54
C	0.18	4.57
D	0.14	3.56
E	0.11	2.79
F	0.61	15.49
G	0.67	17.02
H	0.17	4.32

7034-20

Figure 25. Grid and thermocouple locations on test vane No. 2.

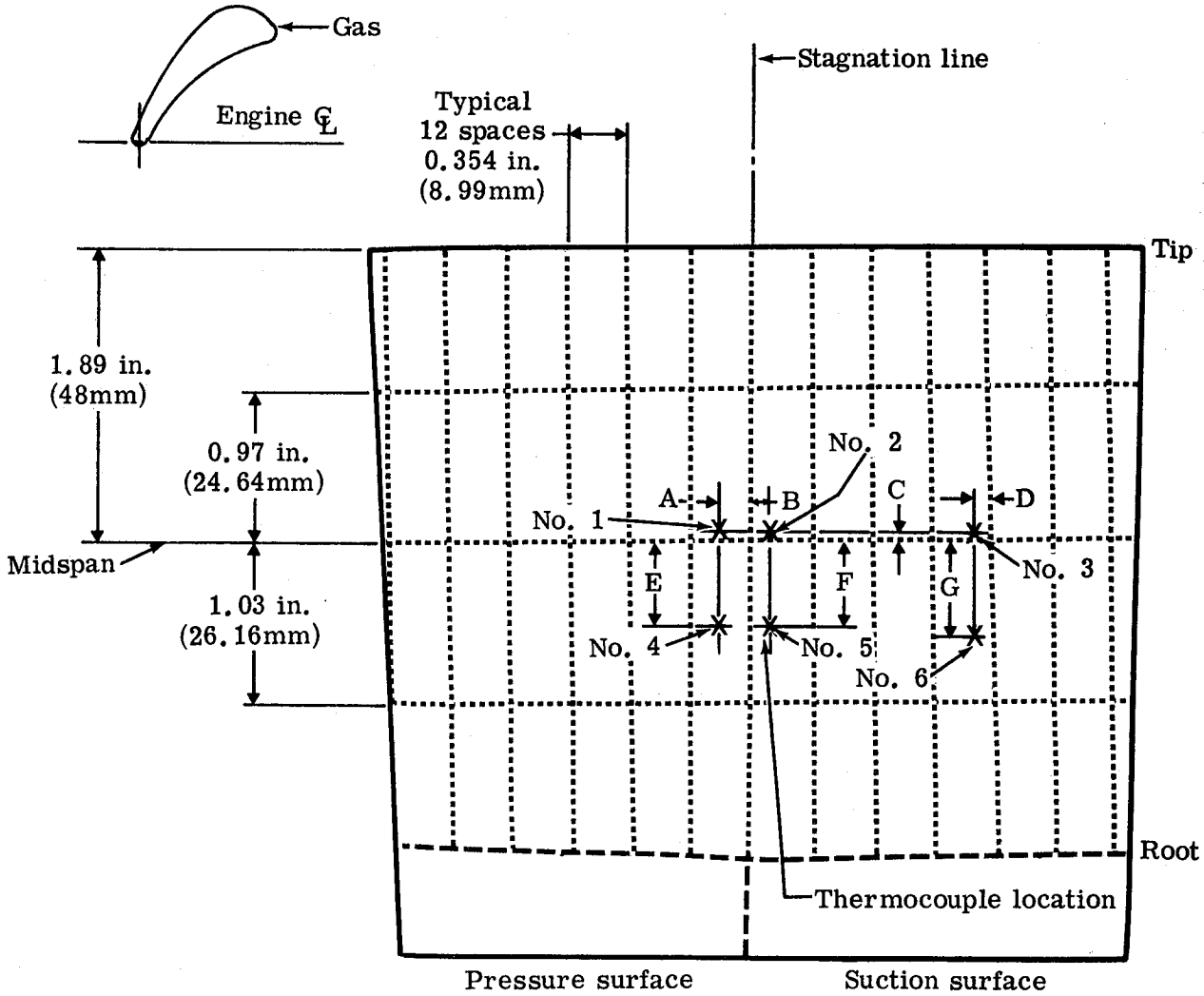

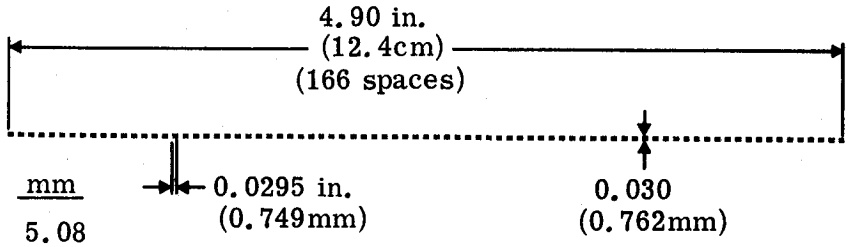

Dimension	in.	mm
A	0.20	5.08
B	0.12	3.05
C	0.06	1.52
D	0.13	3.30
E	0.51	13.0
F	0.53	13.5
G	0.60	15.2

7034-21

Figure 26. Grid and thermocouple locations on test vane No. 3.

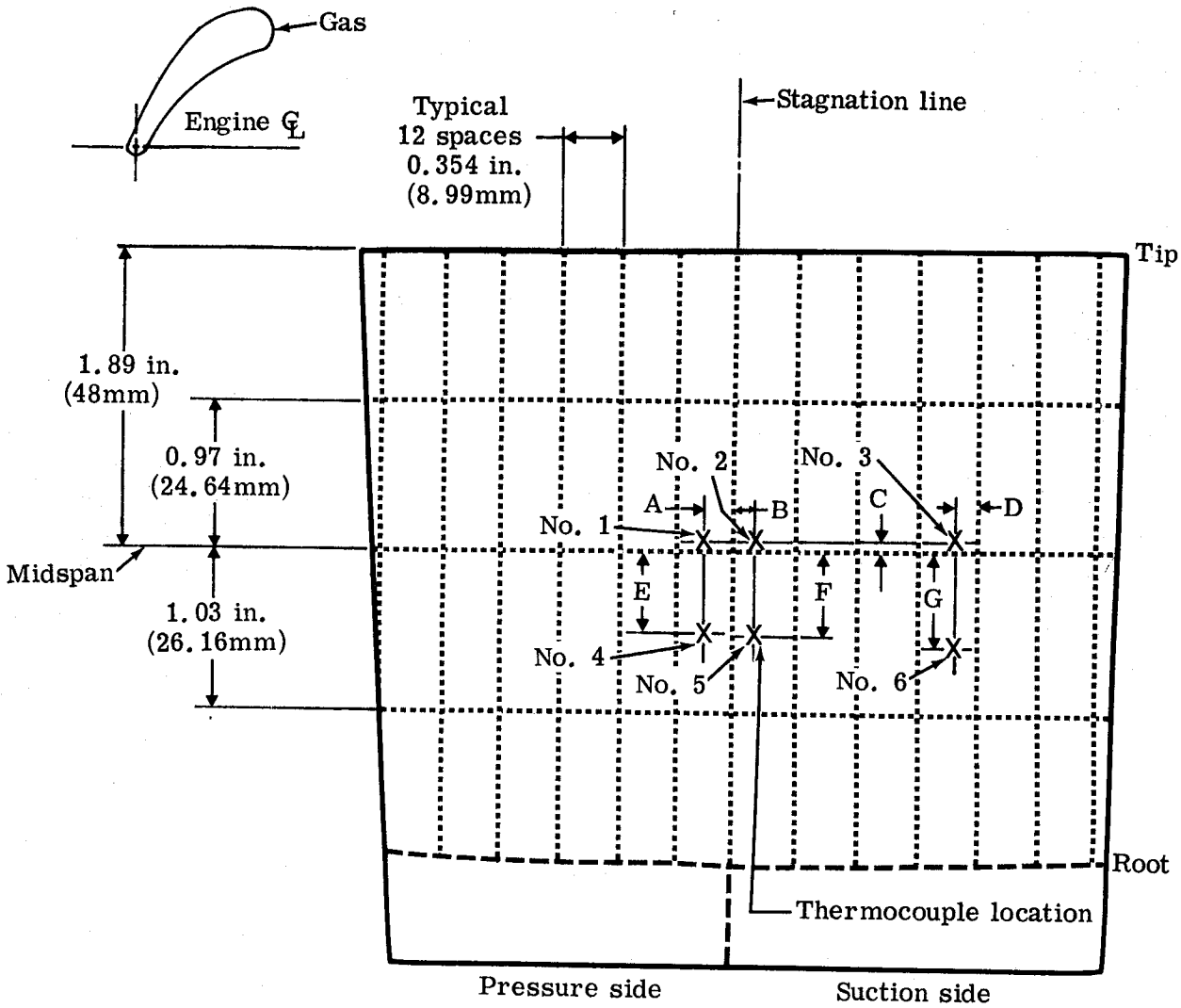

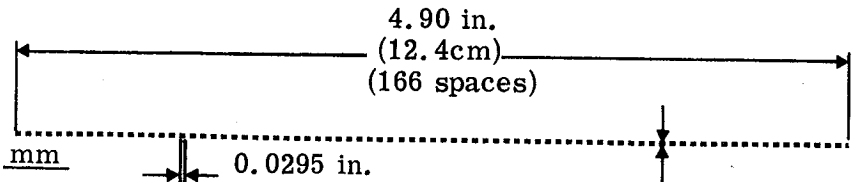

Dimension	in.	mm
A	0.20	5.08
B	0.12	3.05
C	0.06	1.52
D	0.13	3.30
E	0.51	12.9
F	0.53	13.5
G	0.60	15.2

7034-22

Figure 27. Grid and thermocouple locations on test vane No. 4.

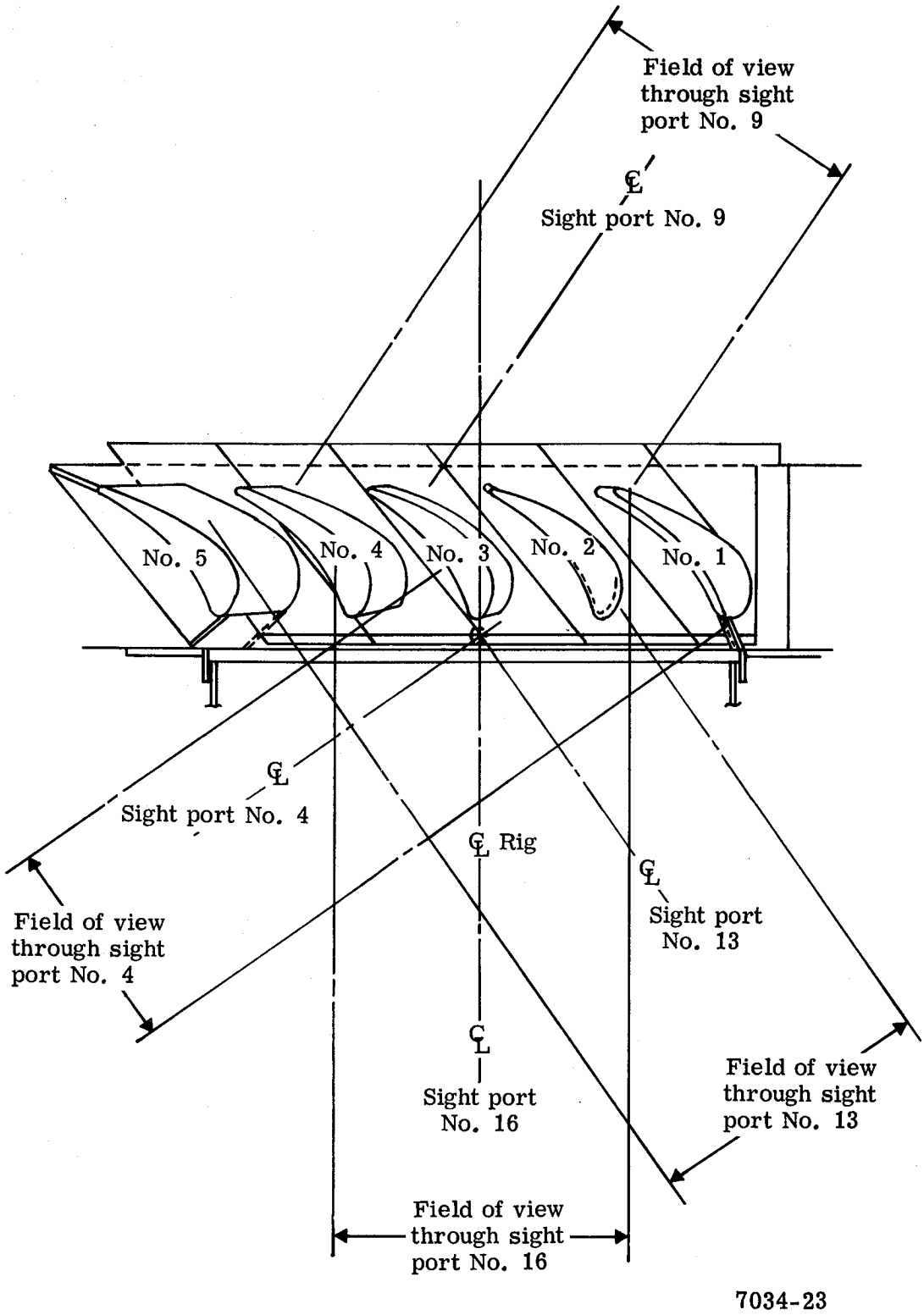

Figure 28. Fields of view through sight port windows.

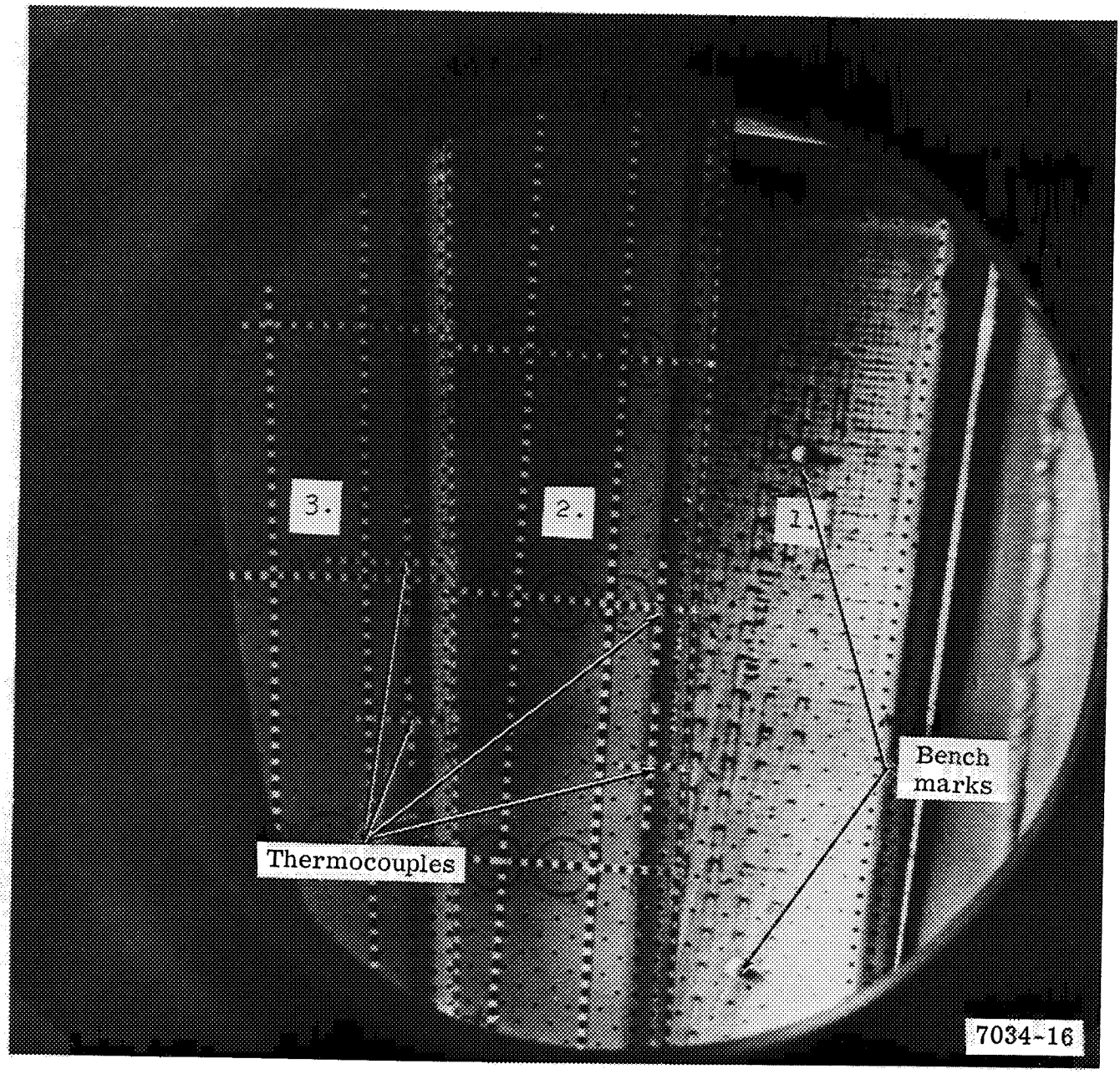

Figure 29. Photograph through sight port No. 4.

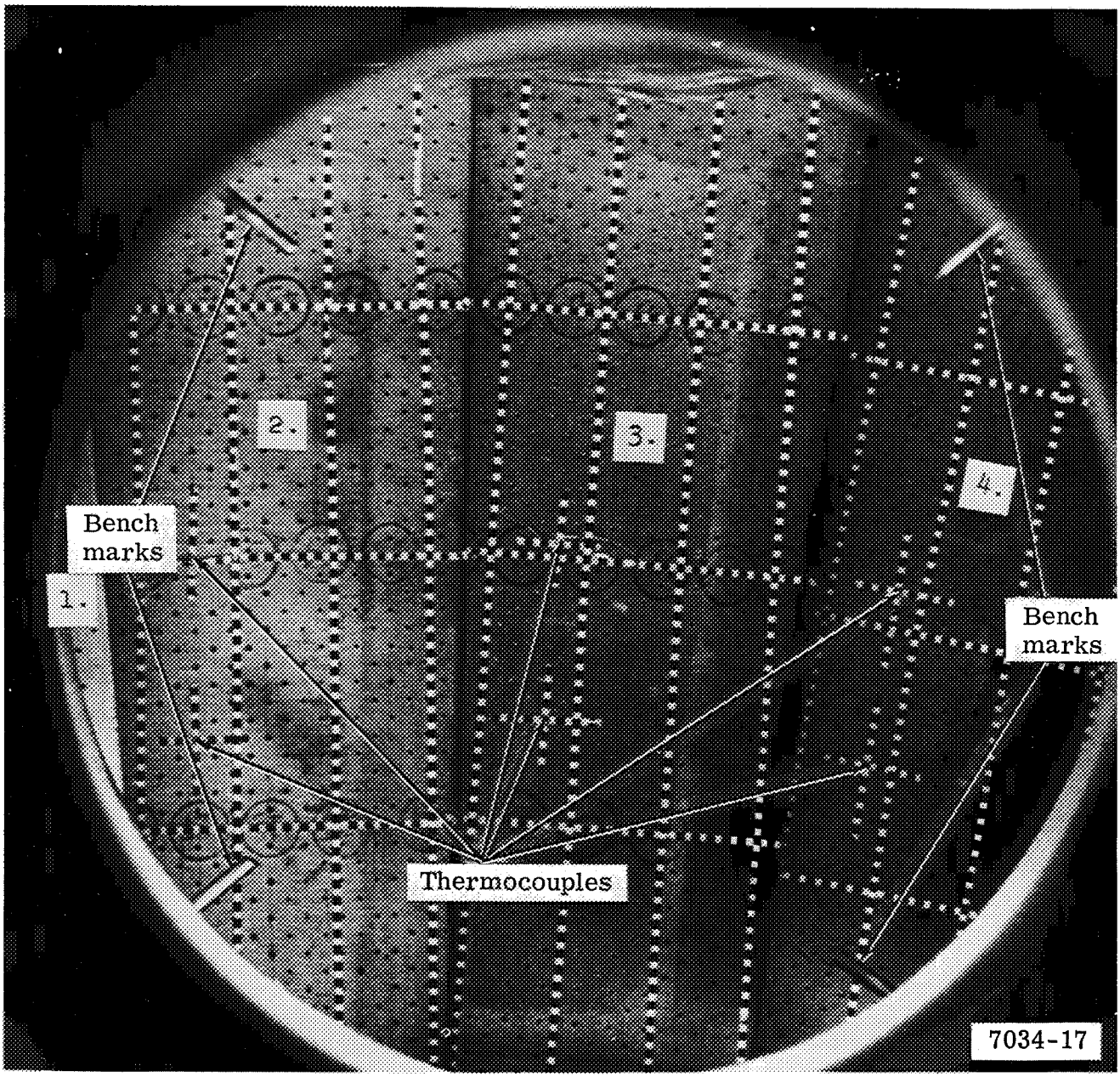

Figure 30. Photograph through sight port No. 9.

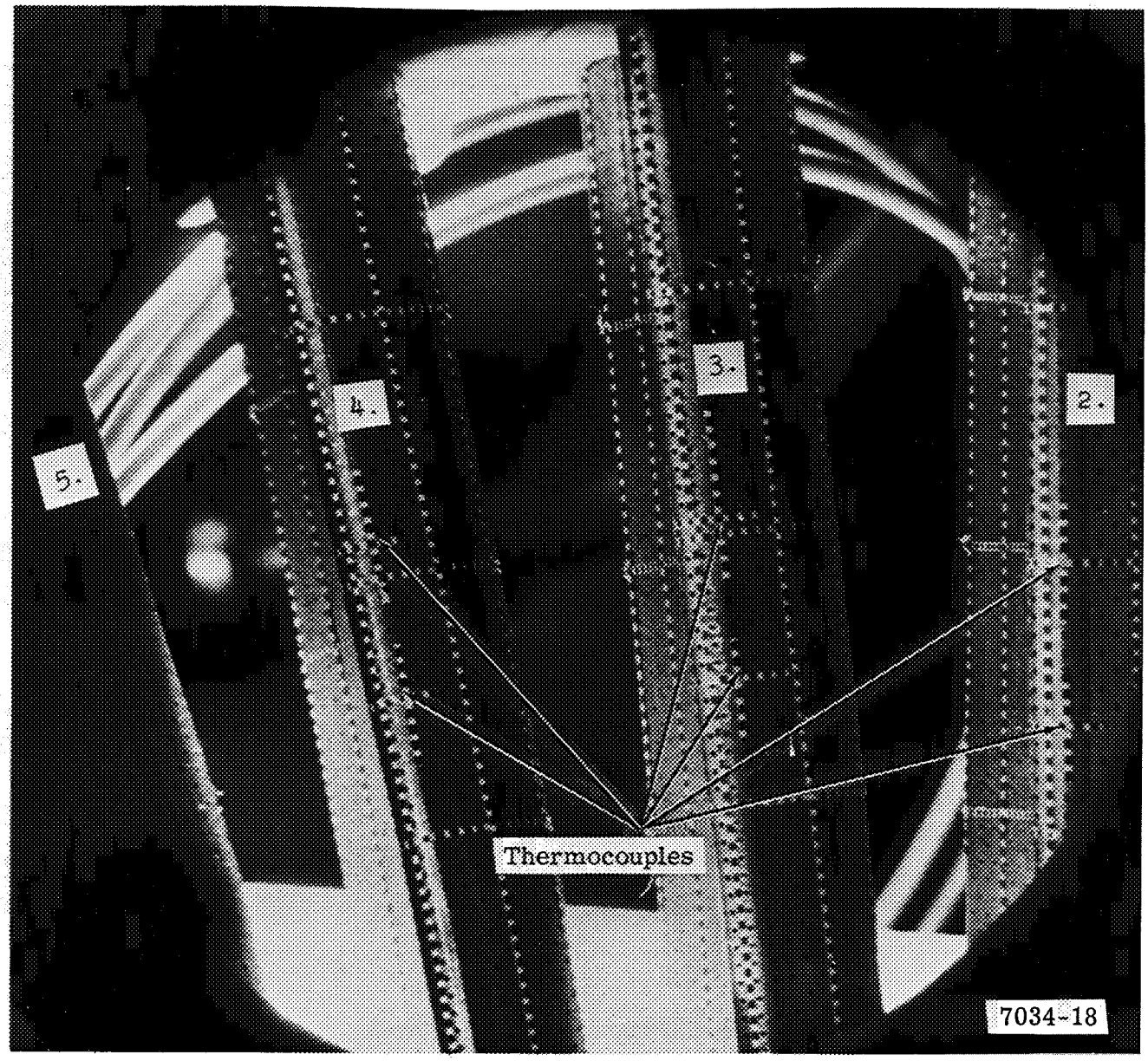

Figure 31. Photograph through sight port No. 13.

Figure 32. Photograph through sight port No. 16.

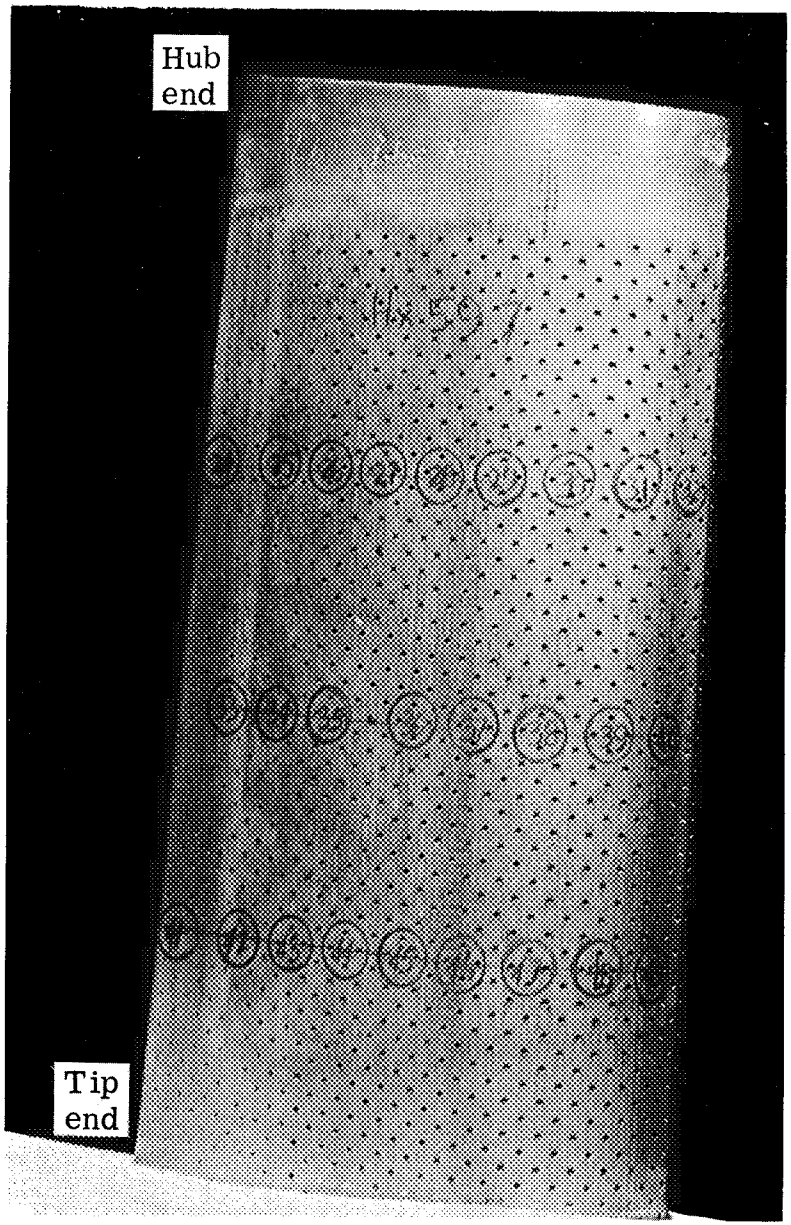

Suction side

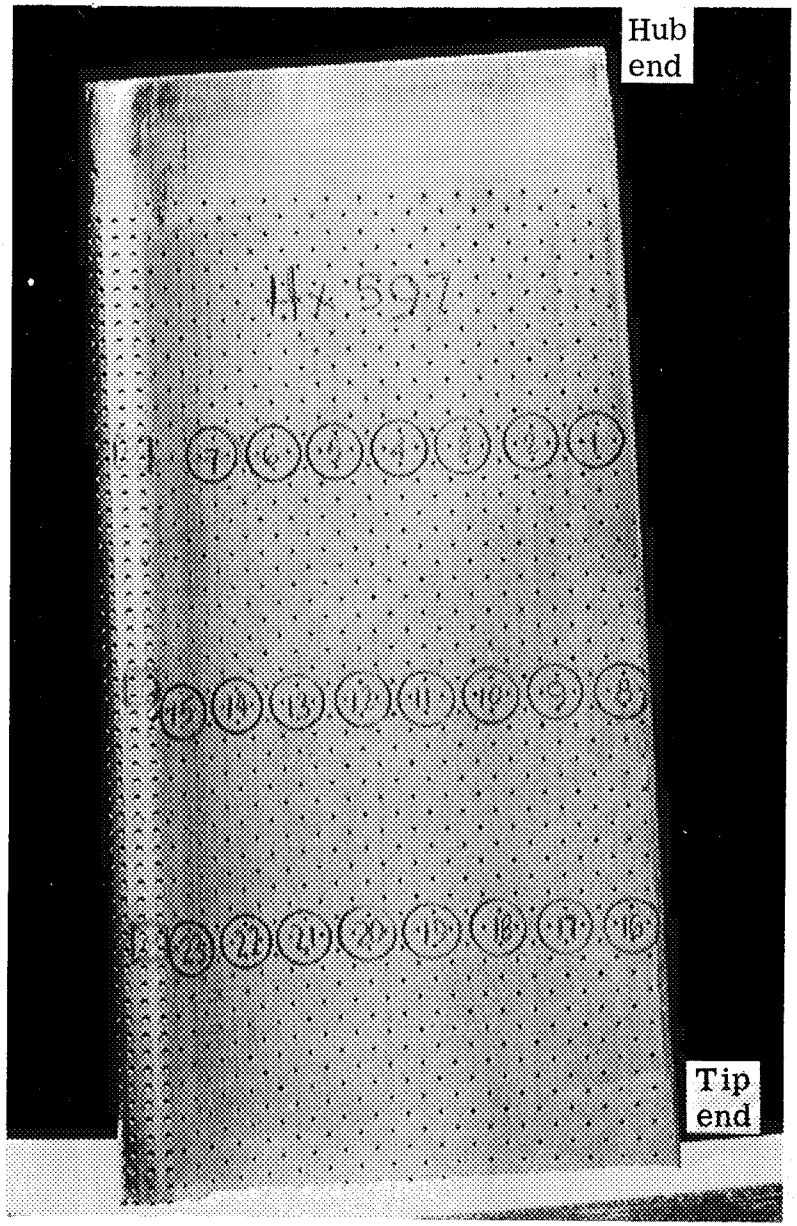

Pressure side

7034-24

Figure 33. Permeability measurement locations for test vane No. 2.

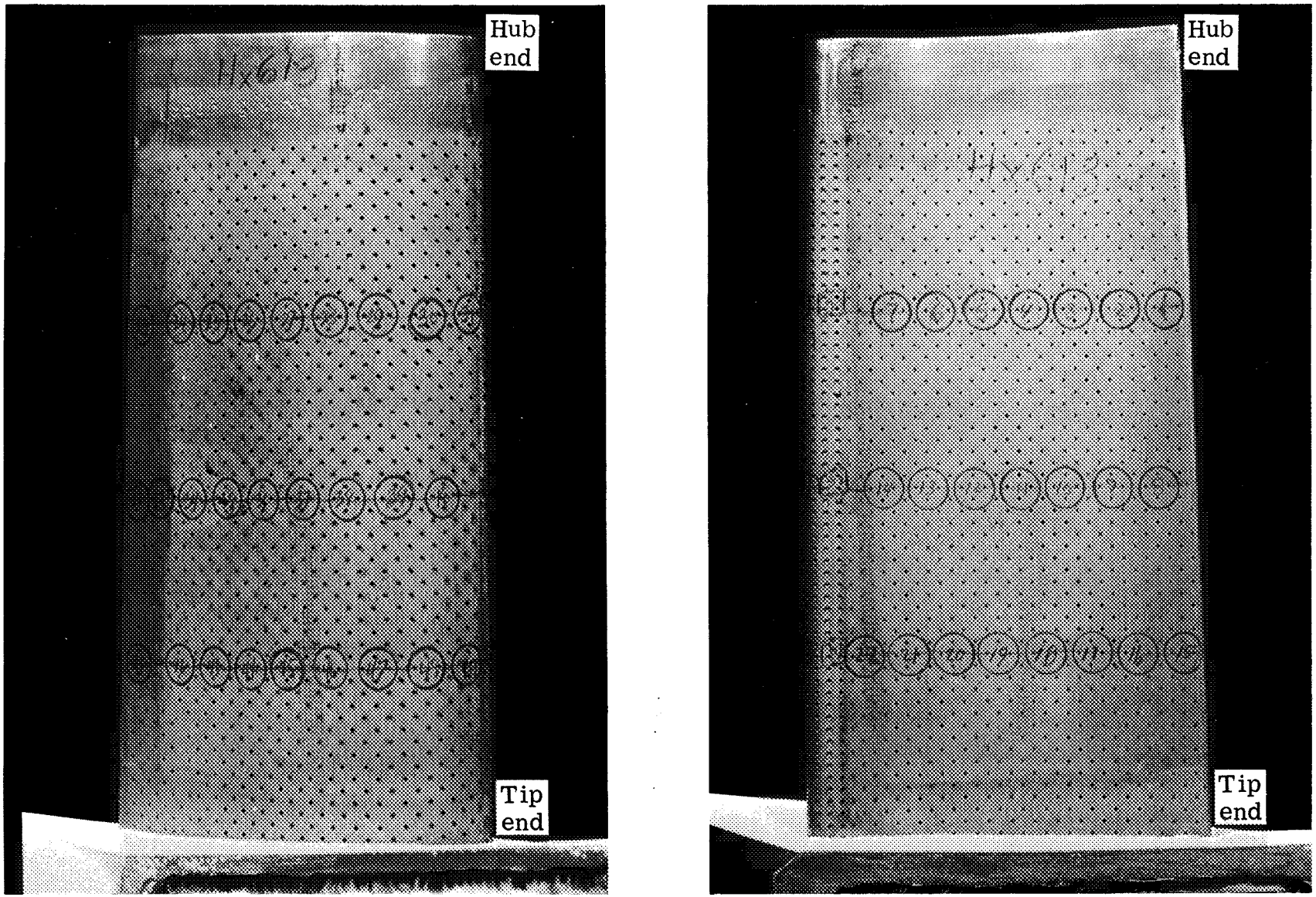

Suction side

Pressure side

7034-25

Figure 34. Permeability measurement locations for test vane No. 3.

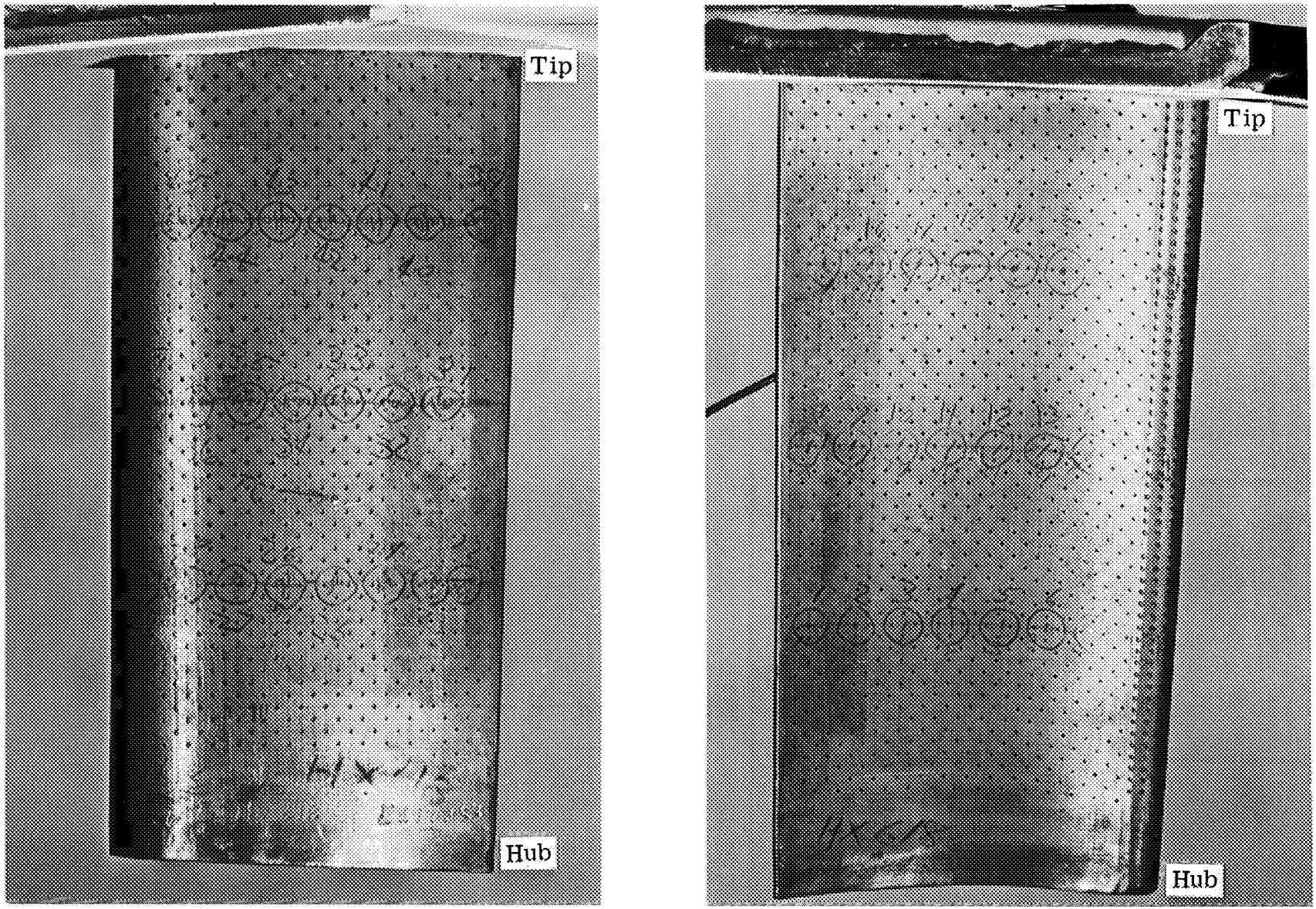

Suction side

Pressure side

7034-26

Figure 35. Permeability measurement locations for test vane No. 4.

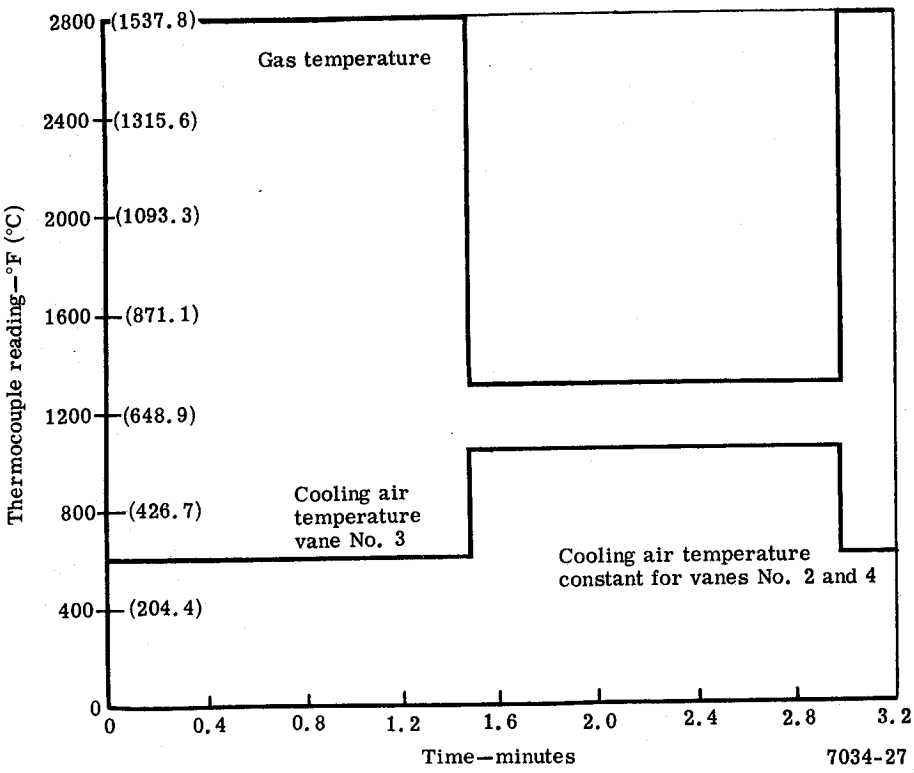

Figure 36. Nominal test conditions.

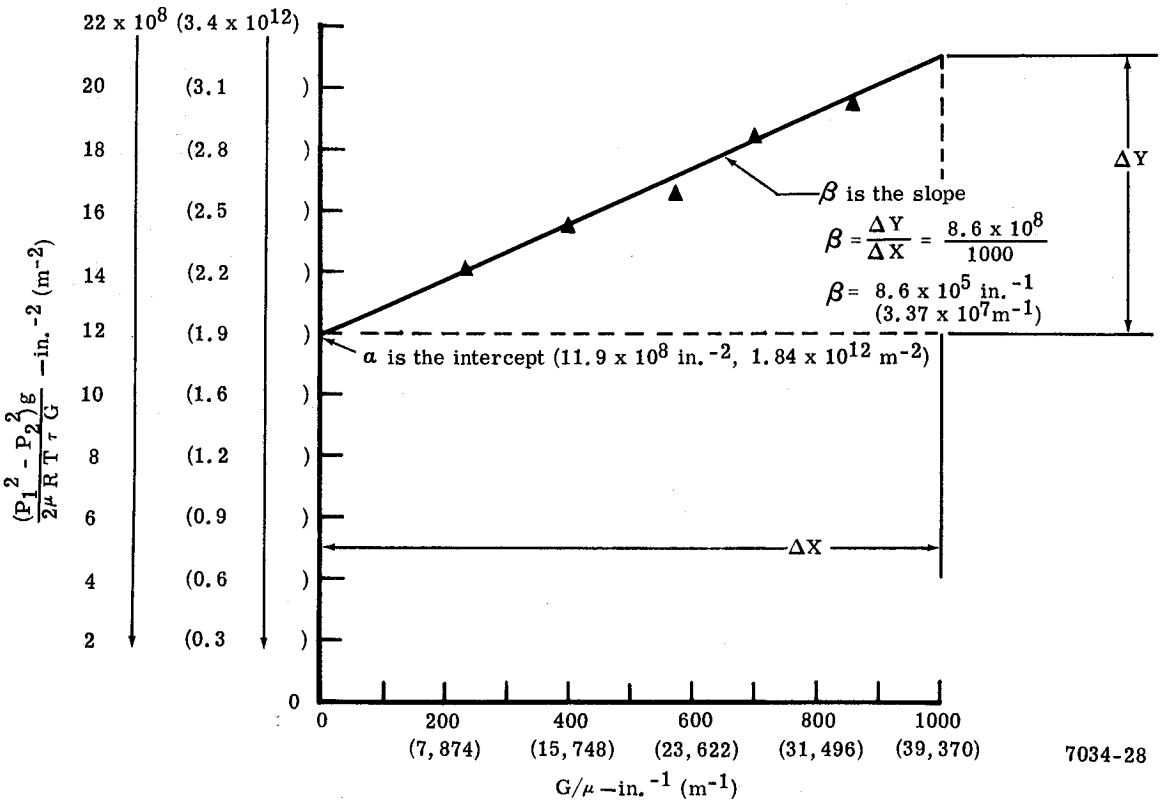

Figure 37. Permeability data for location 2 on test vane No. 2.

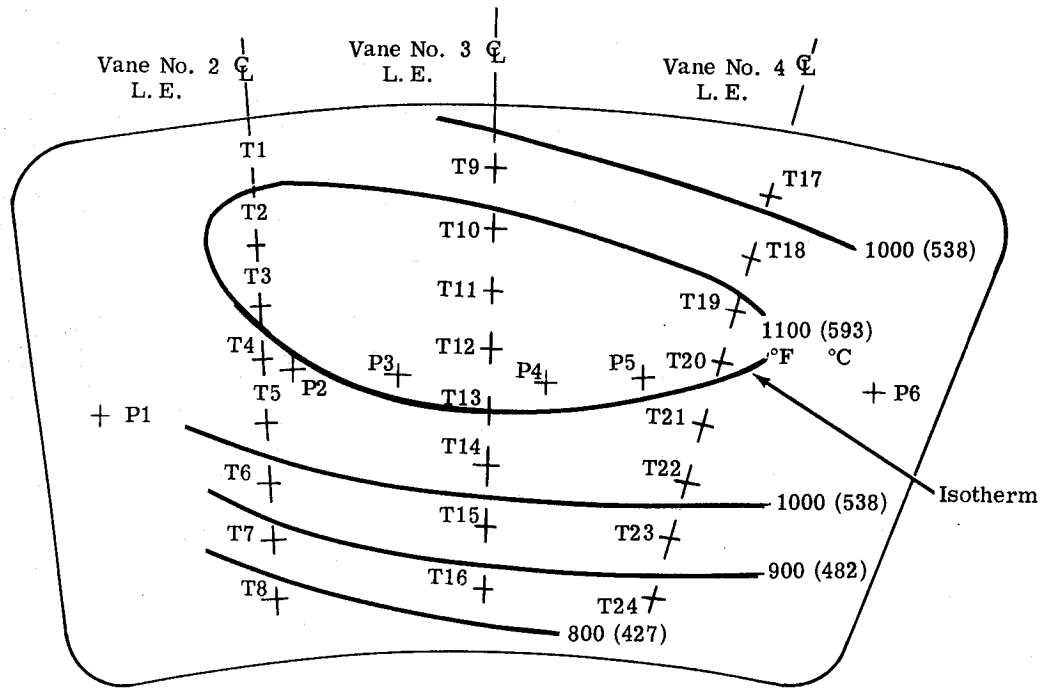

Location	Temperature °F (°C)
T1	1100 (593)
T2	1130 (610)
T3	1110 (599)
T4	1090 (588)
T5	1050 (566)
T6	980 (527)
T7	860 (460)
T8	770 (410)
T9	1040 (560)
T10	1120 (604)
T11	1140 (616)
T12	1140 (616)
T13	1110 (599)
T14	1050 (566)
T15	965 (518)
T16	890 (477)
T17	970 (521)
T18	1050 (566)
T19	1110 (599)
T20	1110 (599)
T21	1080 (582)
T22	1030 (554)
T23	950 (510)
T24	875 (468)

Location	Total pressure in. Hg abs (N/cm^2 abs)
P1	201.7 (68.3)
P2	201.9 (68.4)
P3	201.7 (68.3)
P4	201.7 (68.3)
P5	201.9 (68.4)
P6	202.0 (68.4)

7034-54A

Figure 38A. Measured gas temperature profiles at inlet to cascade looking upstream (low gas temperature portion of cycle).

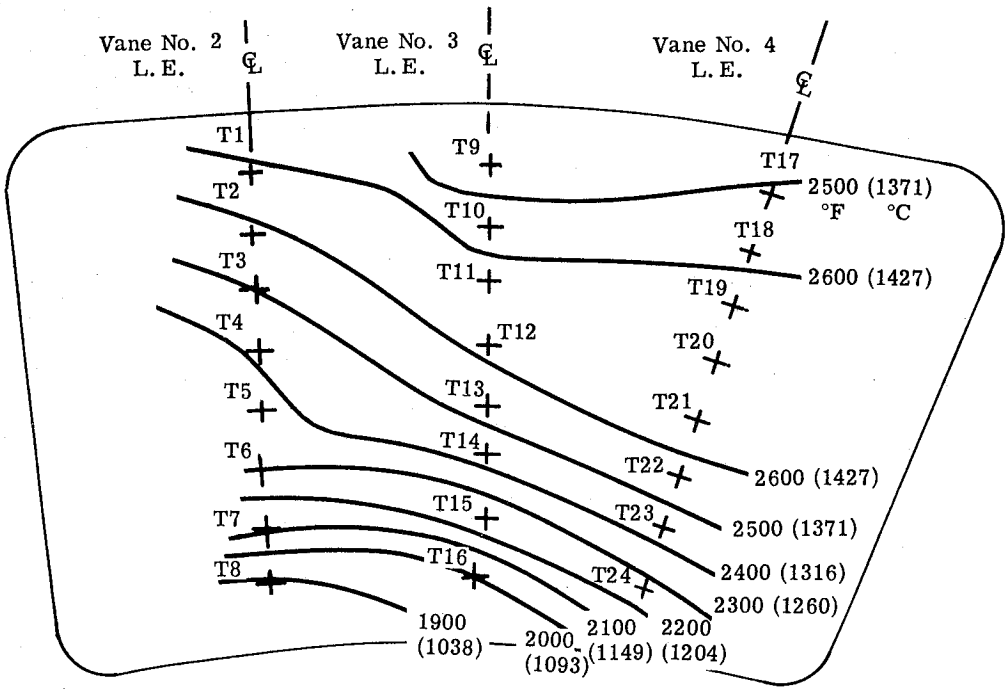

Location	Temperature °F (°C)
T1	2640 (1449)
T2	2500 (1371)
T3	2500 (1371)
T4	2410 (1321)
T5	2380 (1304)
T6	2300 (1260)
T7	2120 (1160)
T8	1860 (1016)
T9	2440 (1338)
T10	2560 (1404)
T11	2630 (1443)
T12	2625 (1441)
T13	2540 (1393)
T14	2410 (1321)
T15	2220 (1216)
T16	2000 (1093)
T17	2510 (1377)
T18	2580 (1416)
T19	2630 (1443)
T20	2660 (1460)
T21	2650 (1454)
T22	2570 (1410)
T23	2430 (1332)
T24	2270 (1242)

7034-54B

Figure 38B. Measured gas temperature profiles at inlet to cascade looking upstream (high gas temperature portion of cycle).

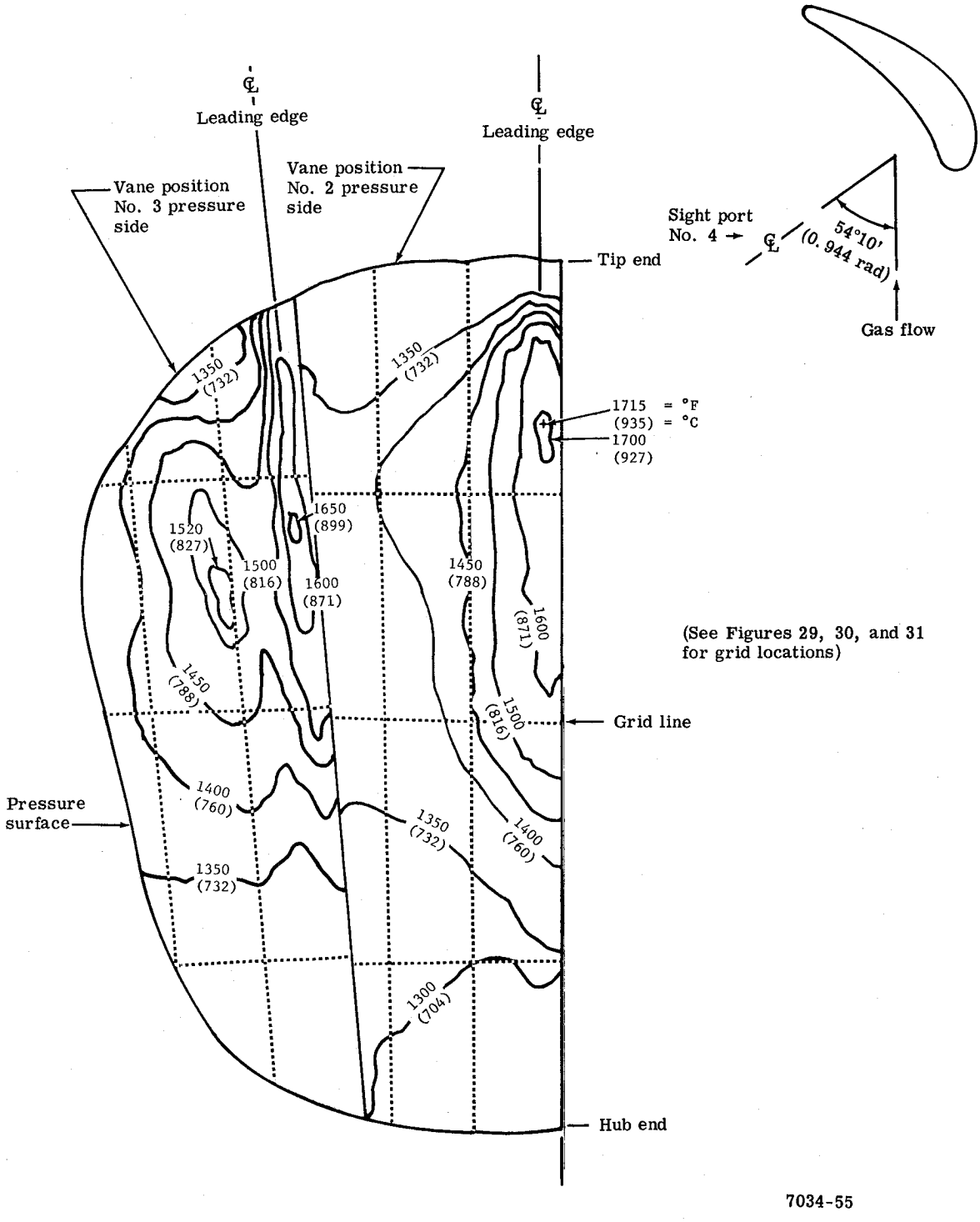

Figure 39. Airfoil surface temperature distributions as observed through sight port No. 4.

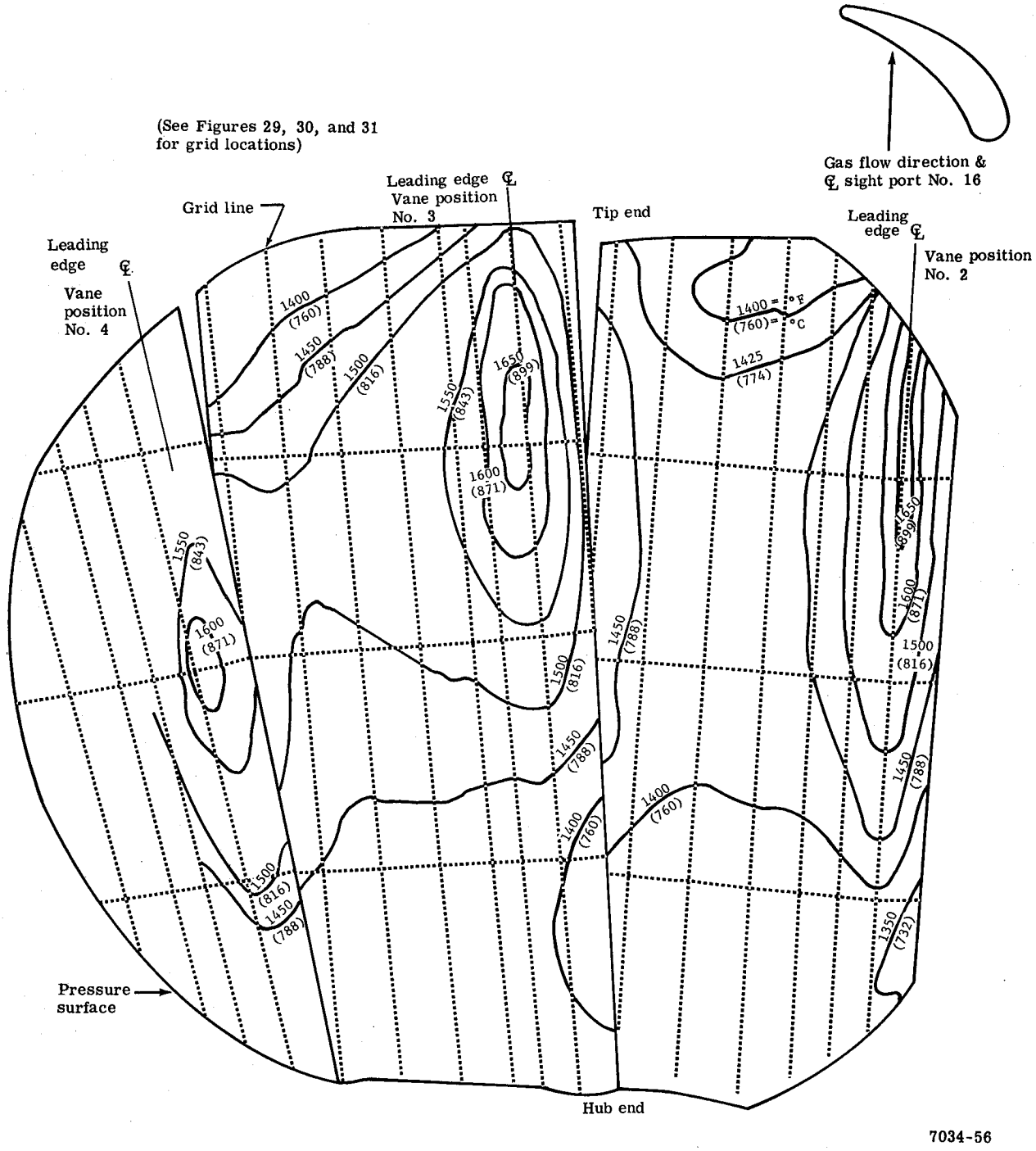

Figure 40. Airfoil surface temperature distributions as observed through sight port No. 16.

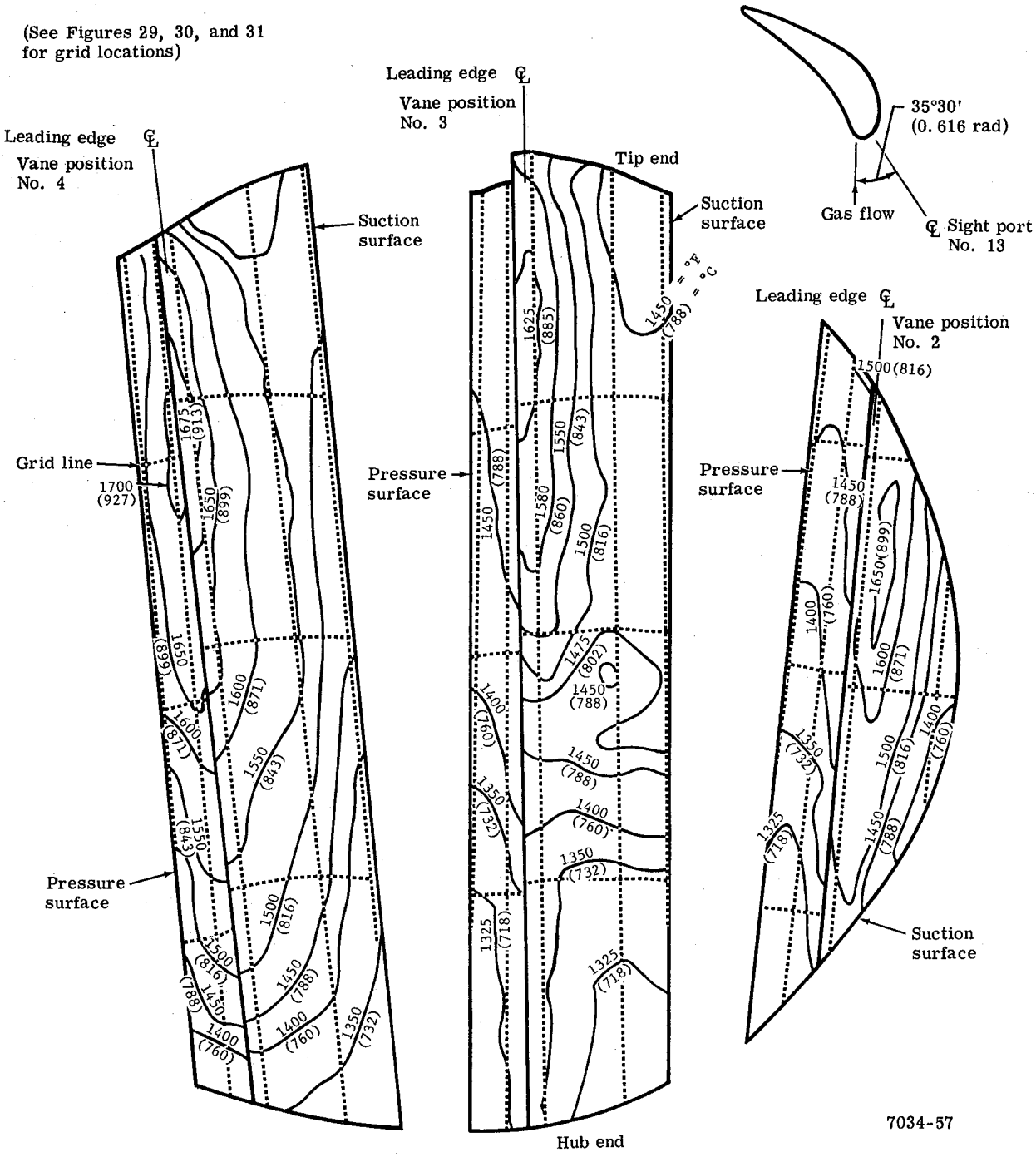

Figure 41. Airfoil surface temperature distributions as observed through sight port No. 13.

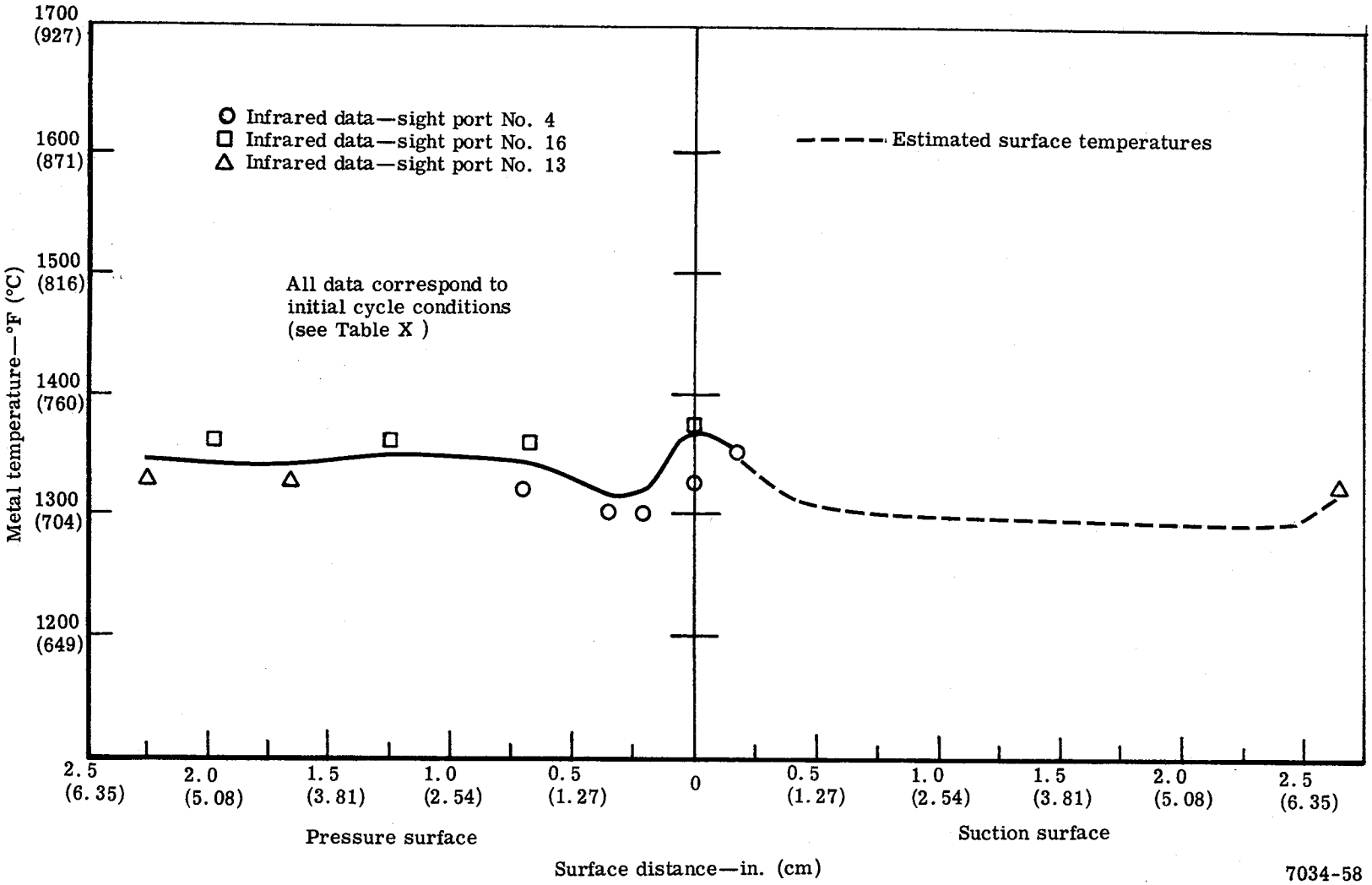

Figure 42. Measured chordwise temperature distribution for test vane No. 2, 1/4-span location.

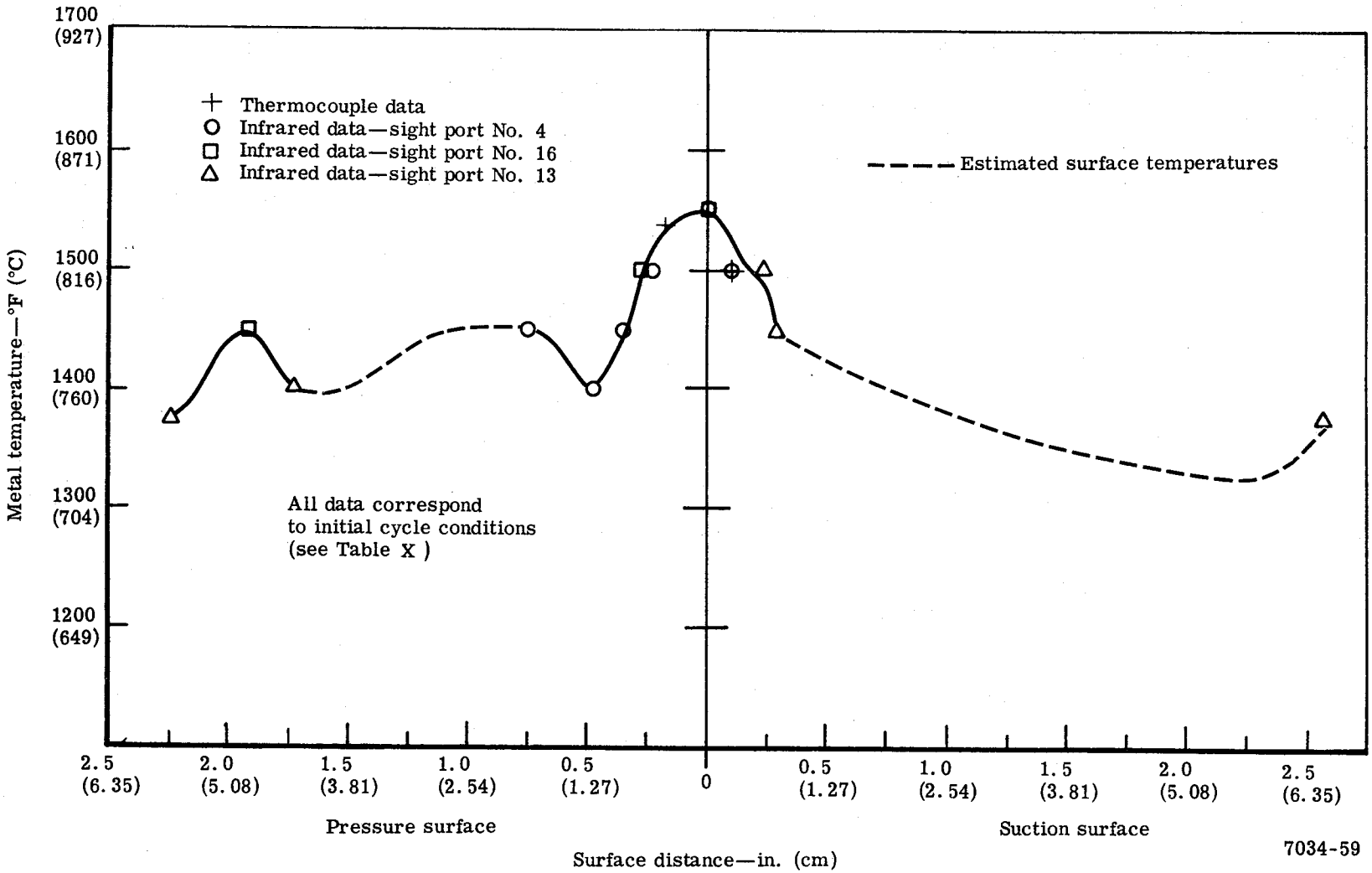

Figure 43. Measured chordwise temperature distribution for test vane No. 2, midspan location.

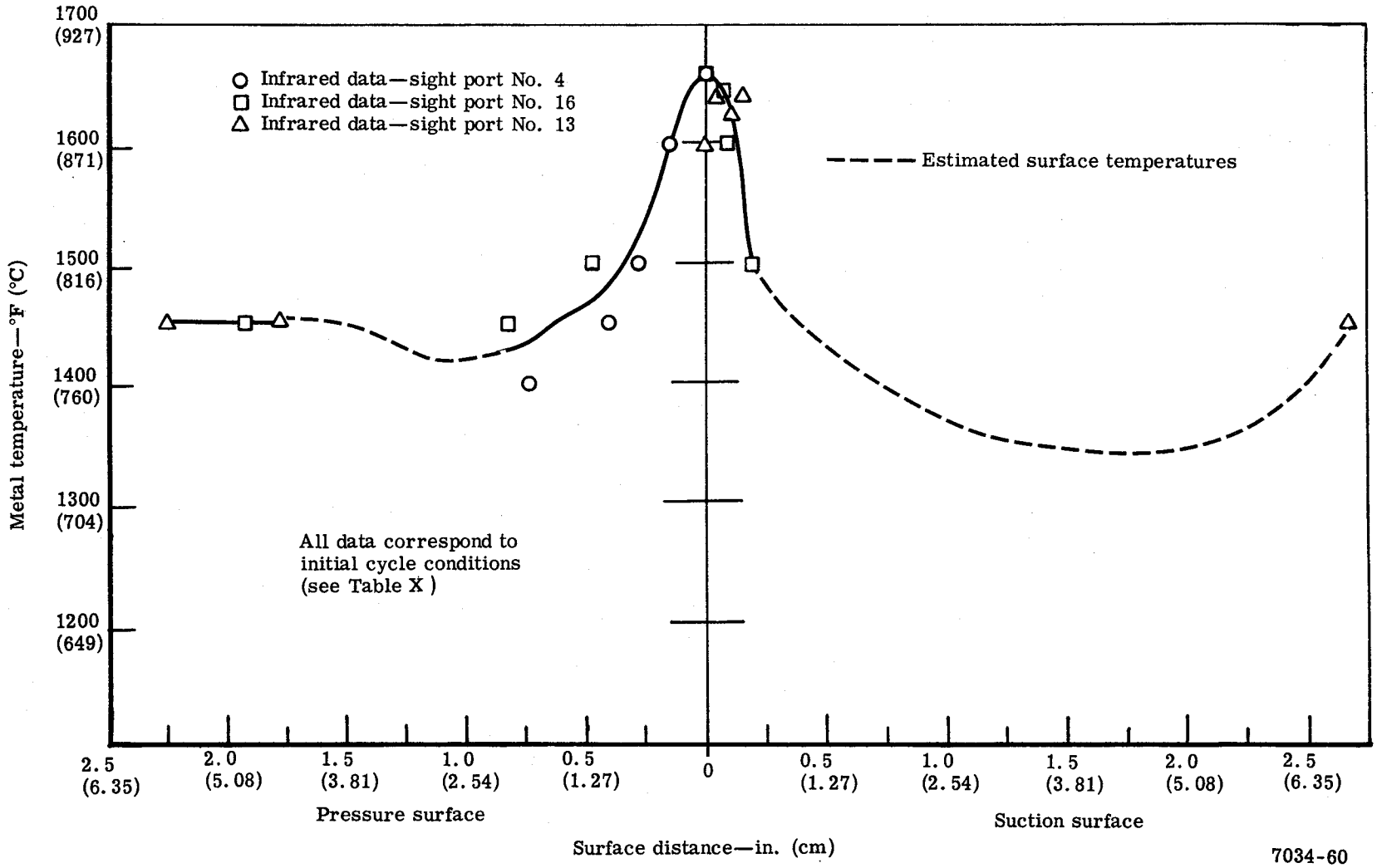

Figure 44. Measured chordwise temperature distribution for test vane No. 2, 3/4-span location.

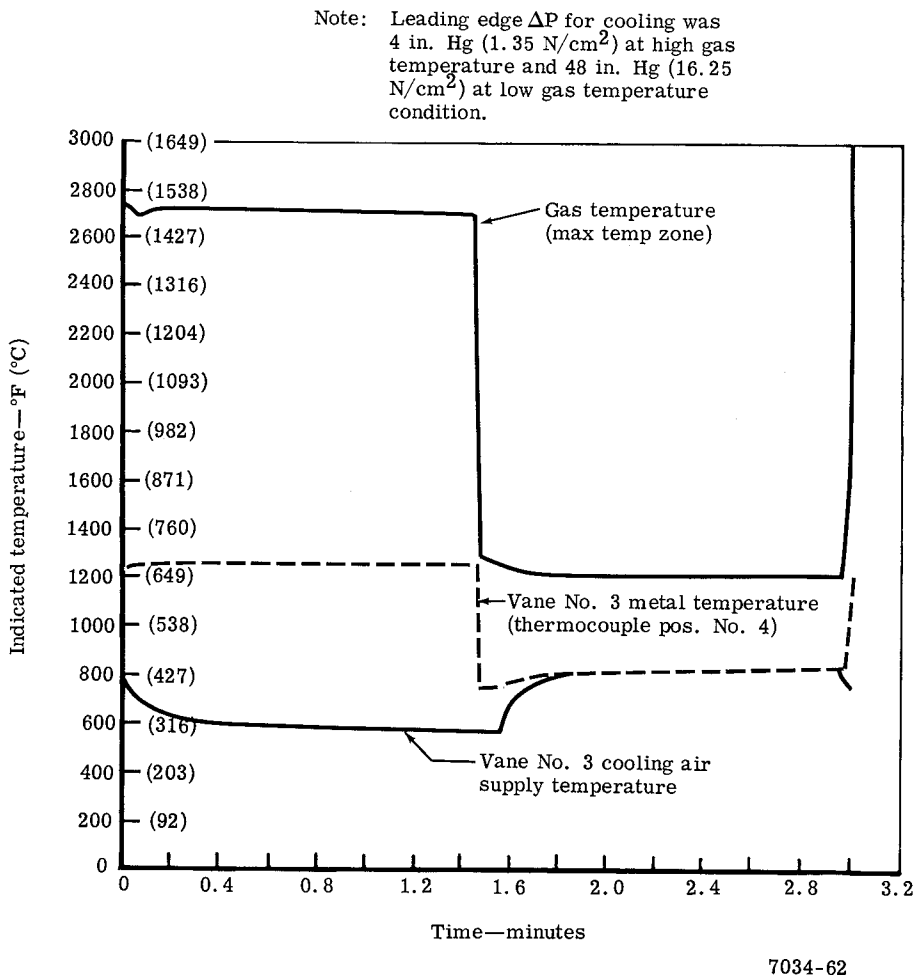

Figure 45. Cyclic temperature characteristics, test vane No. 3.

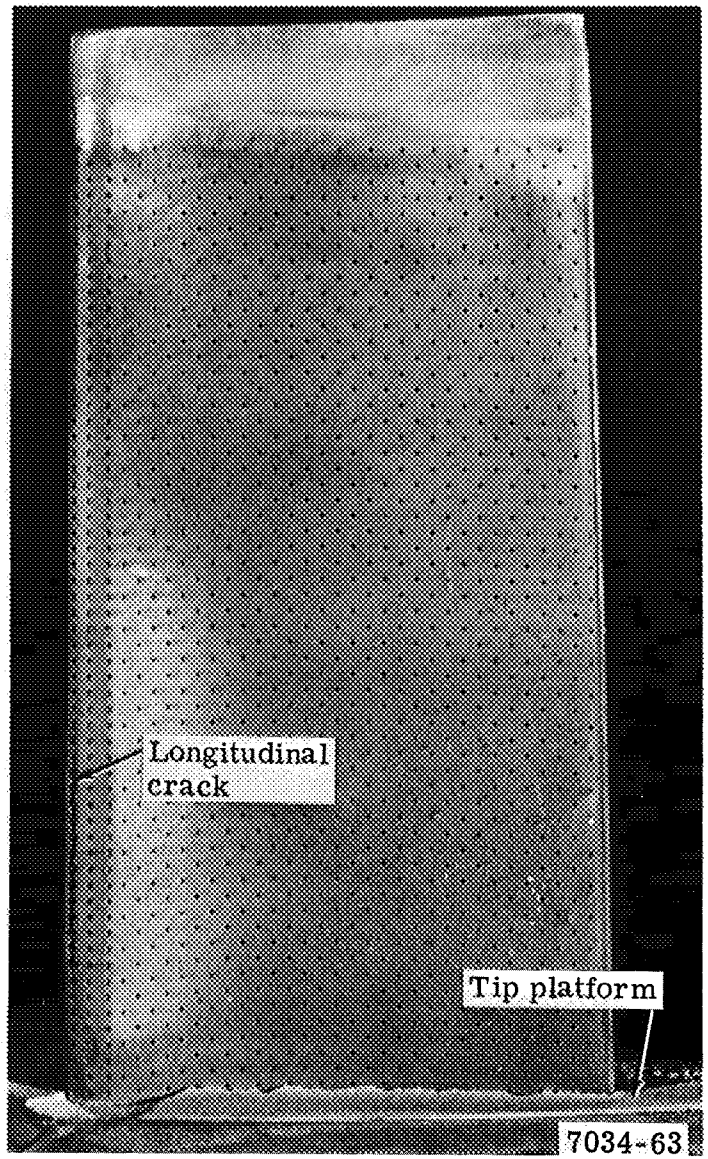

Figure 46. Pressure side view of test vane No. 2 after 110 cycles.

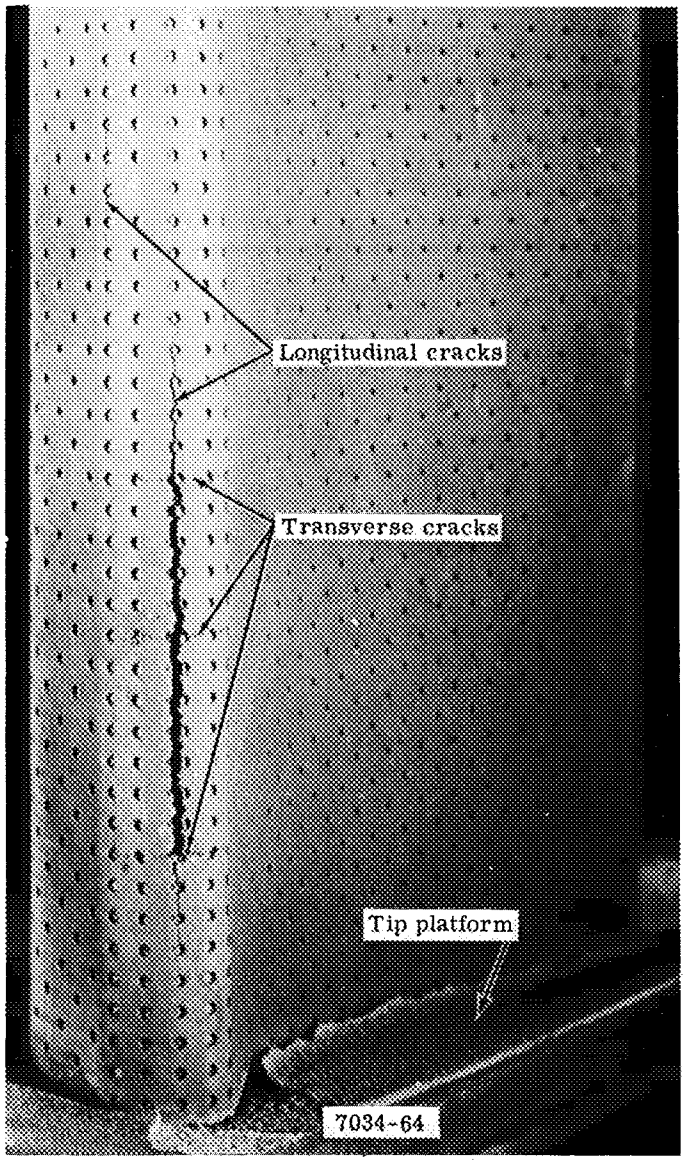

Figure 47. Leading edge cracks in test vane No. 2 after 110 cycles.

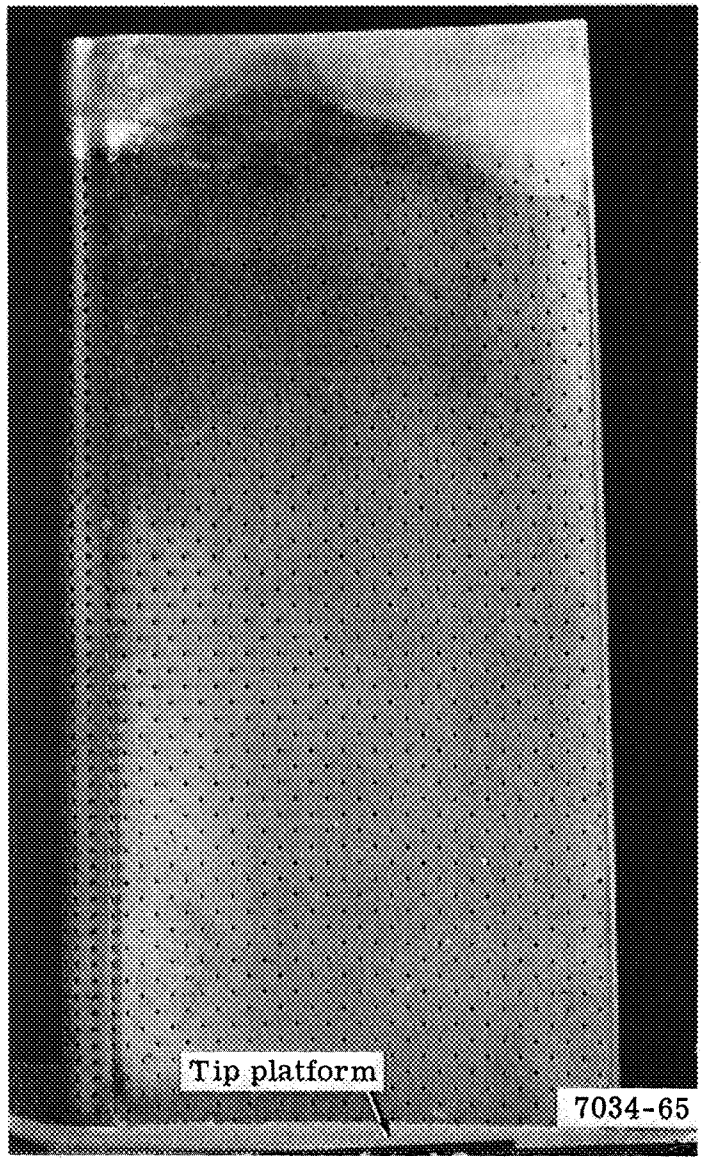

Figure 48. Pressure side view of test vane No. 3 after 110 cycles.

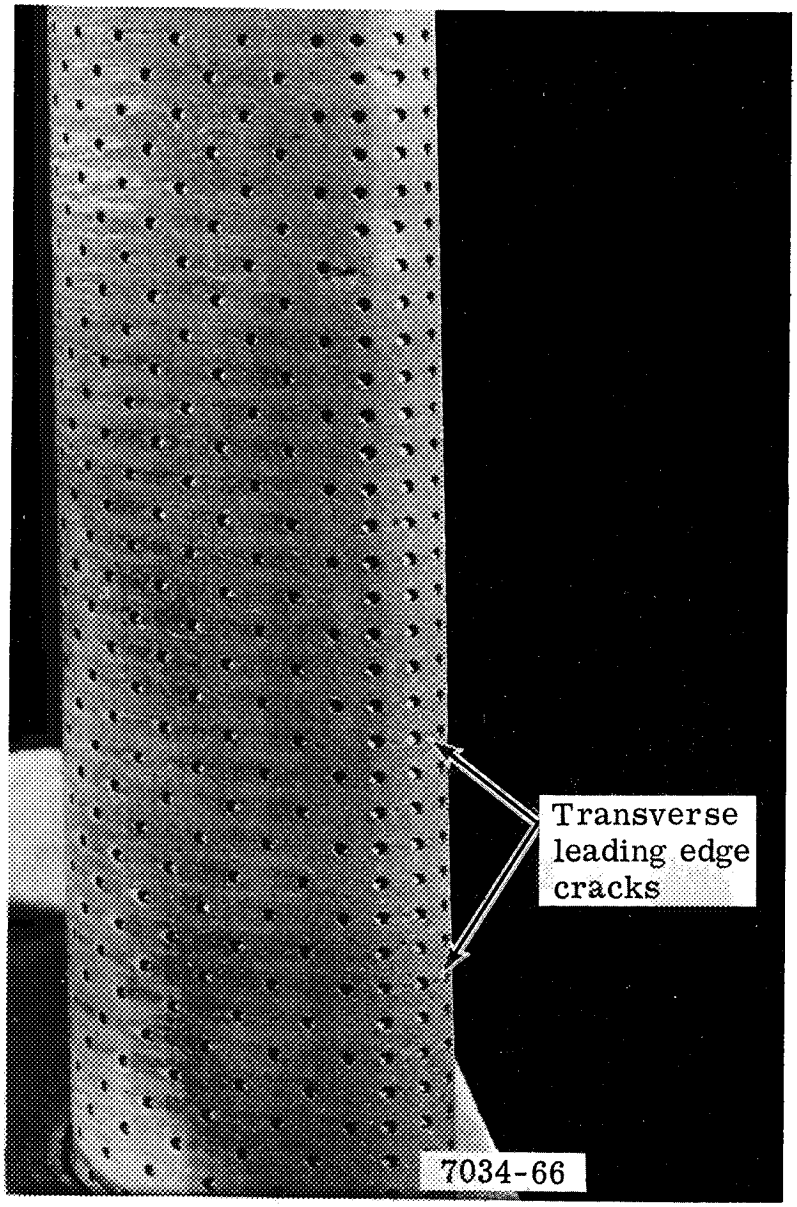

Figure 49. Leading edge and suction side view of test vane No. 3 after 110 cycles.

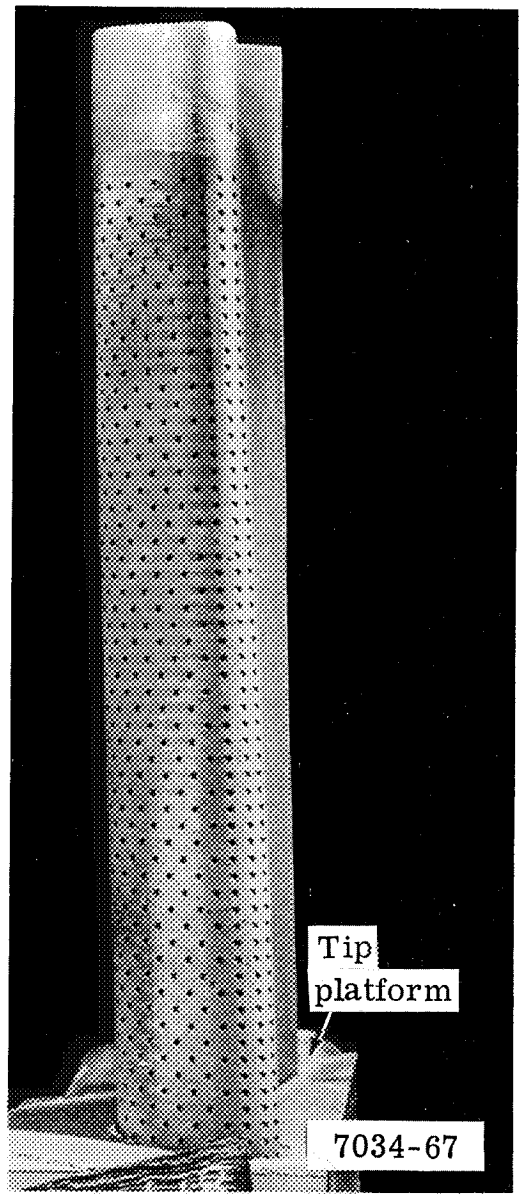

Figure 50. Leading edge view of test vane No. 4 after 110 cycles.

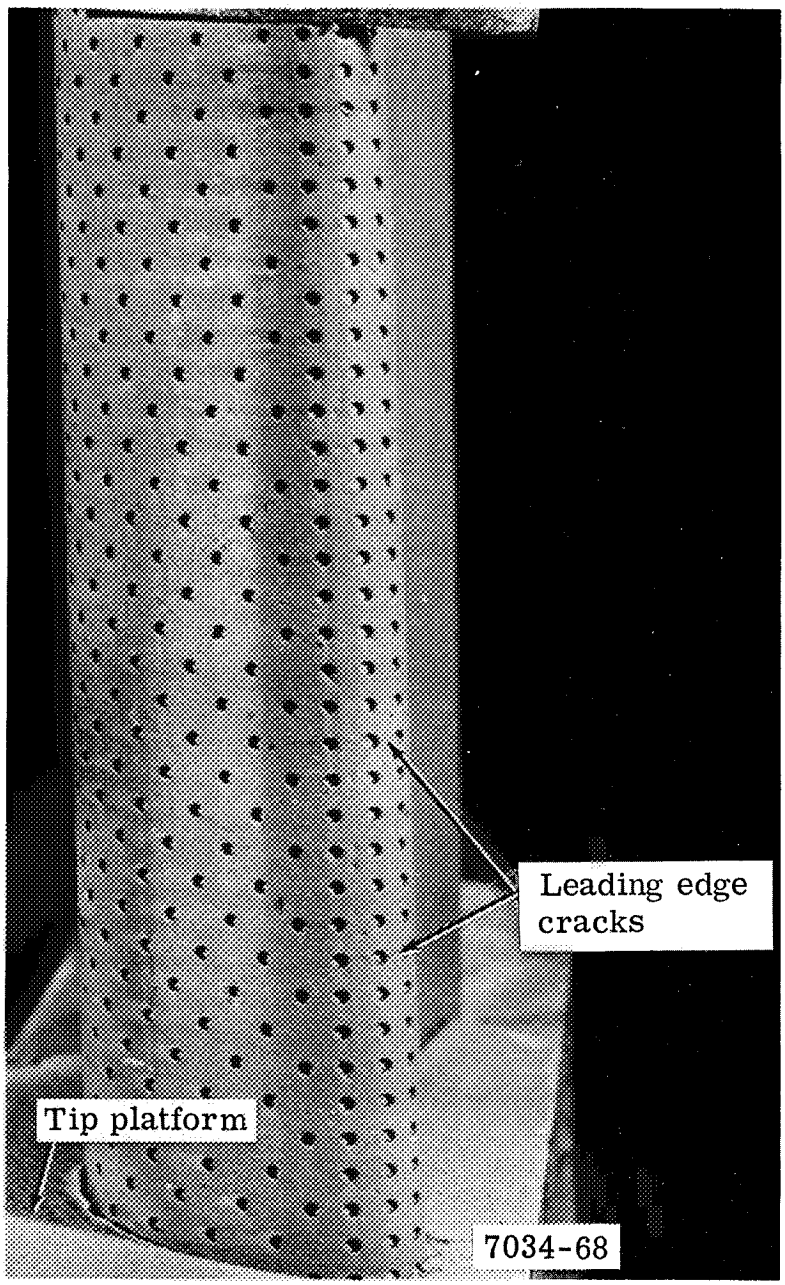

Figure 51. Leading edge and suction side view of test vane No. 4 after 110 cycles.

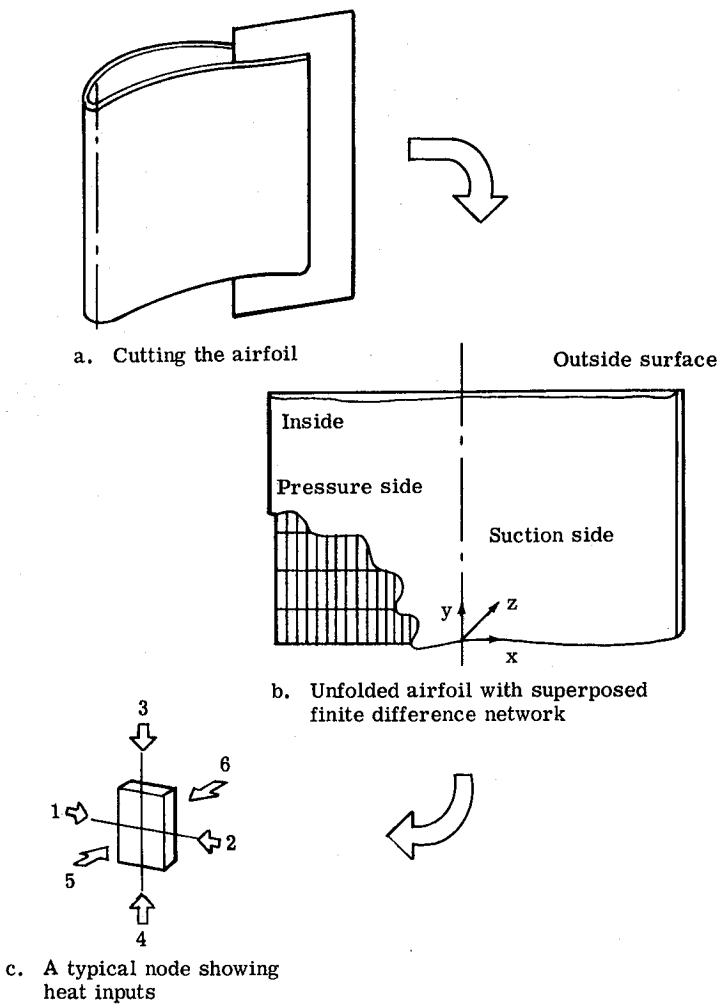

Figure 52. Two-dimensional representation of air-cooled turbine airfoil.

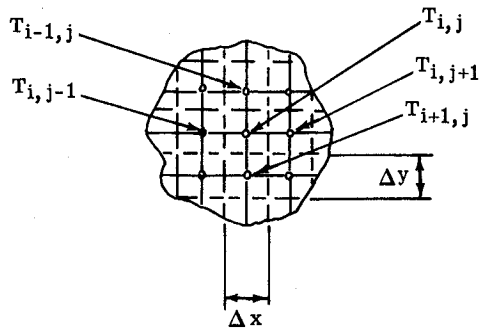

Figure 53. Typical node pattern.

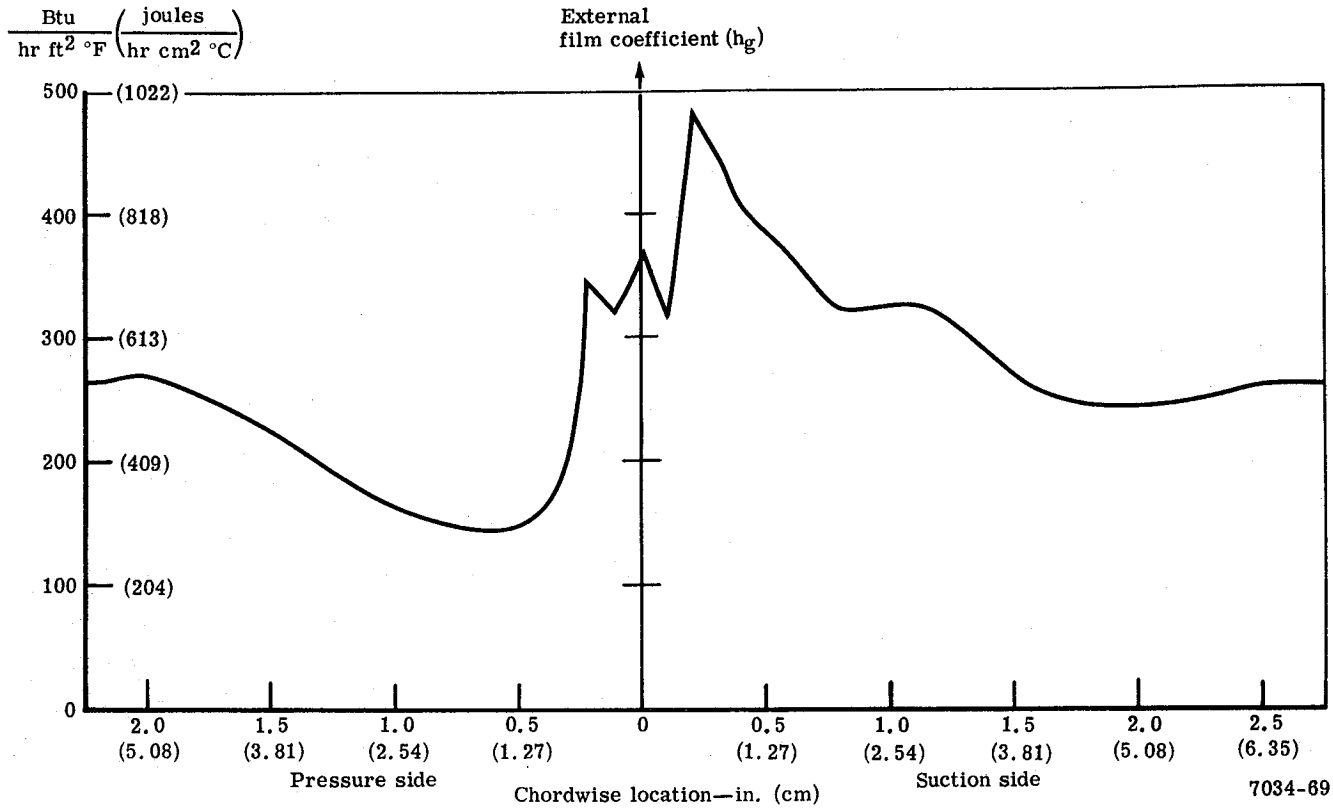

Figure 54. Predicted external film coefficient distribution for test vane No. 2.

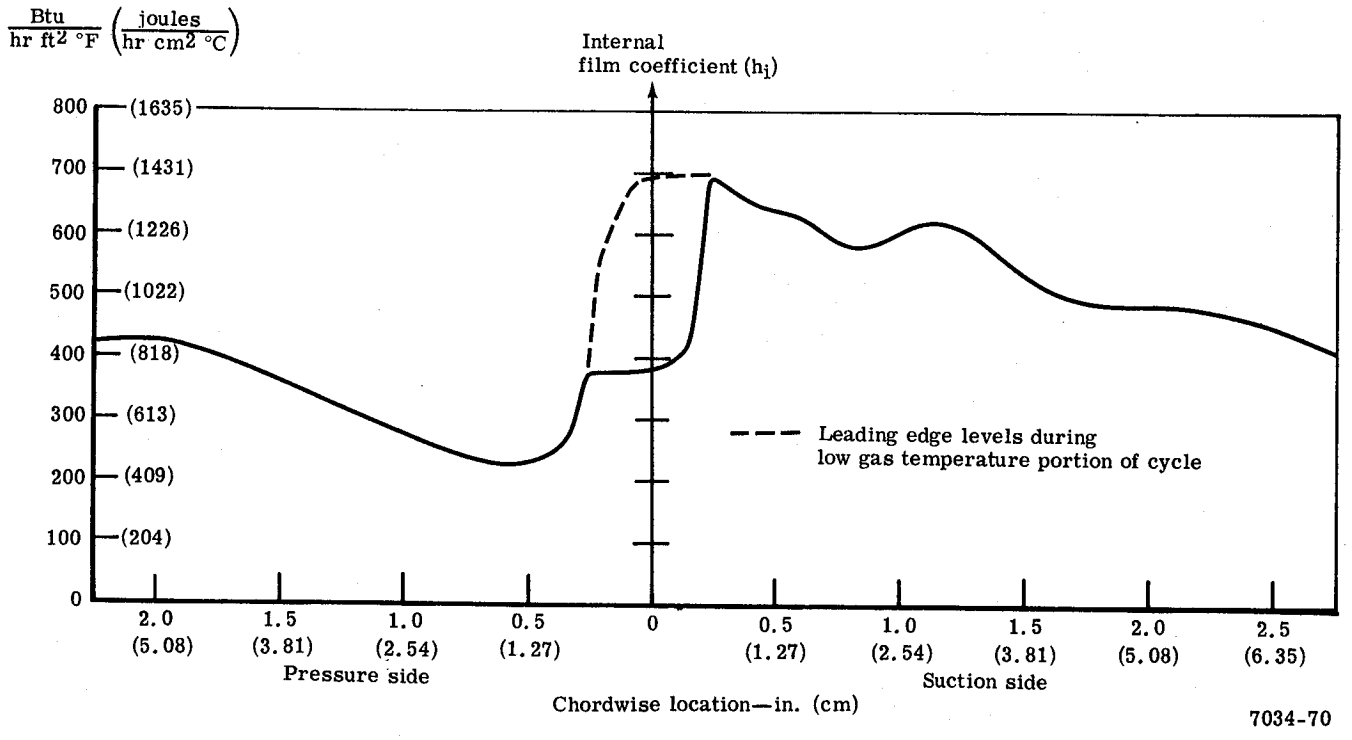

Figure 55. Estimated internal film coefficient distribution for test vane No. 2.

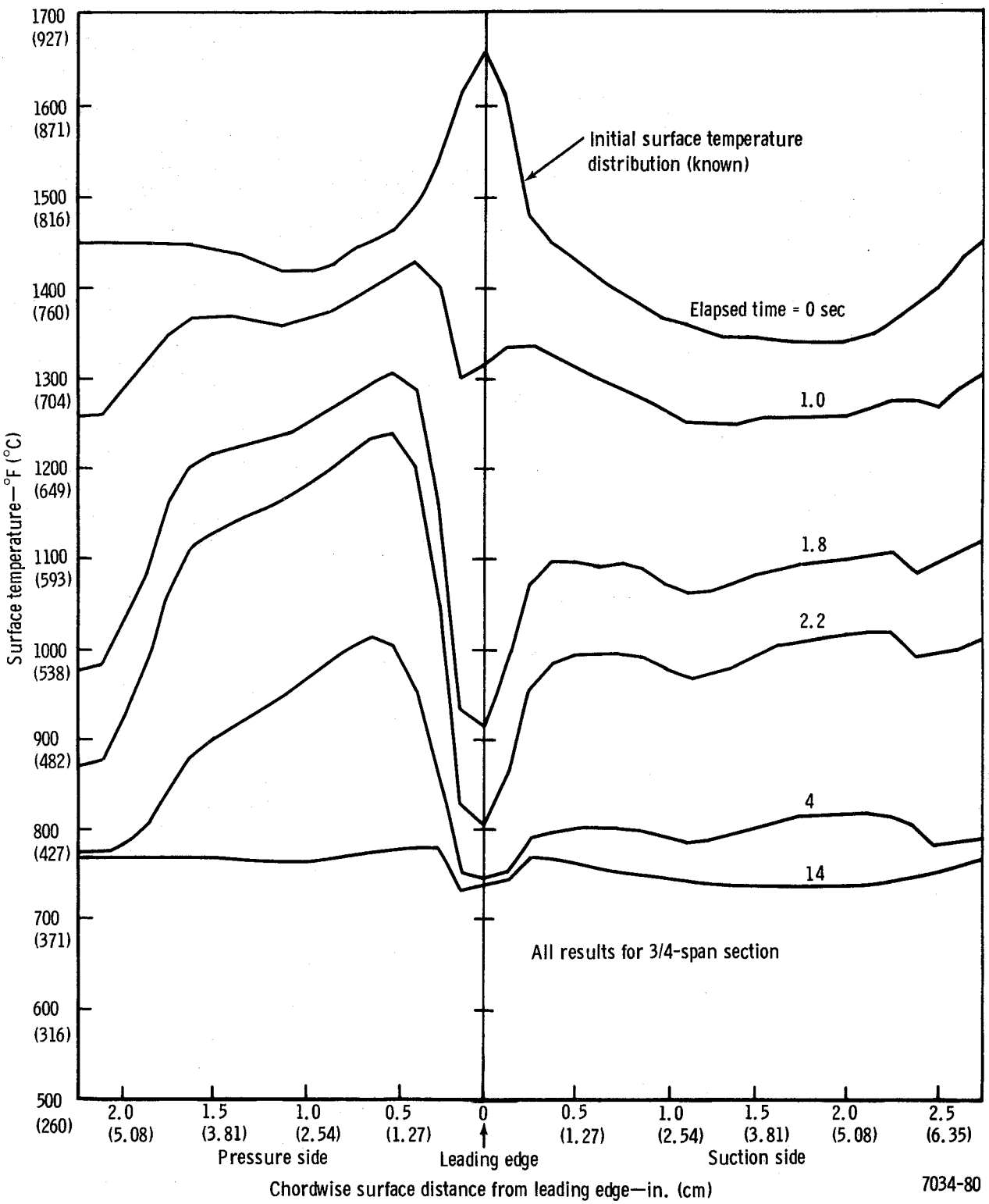

Figure 56. Predicted transient chordwise surface temperature distribution for rapid decrease in gas temperature (test vane No. 2).

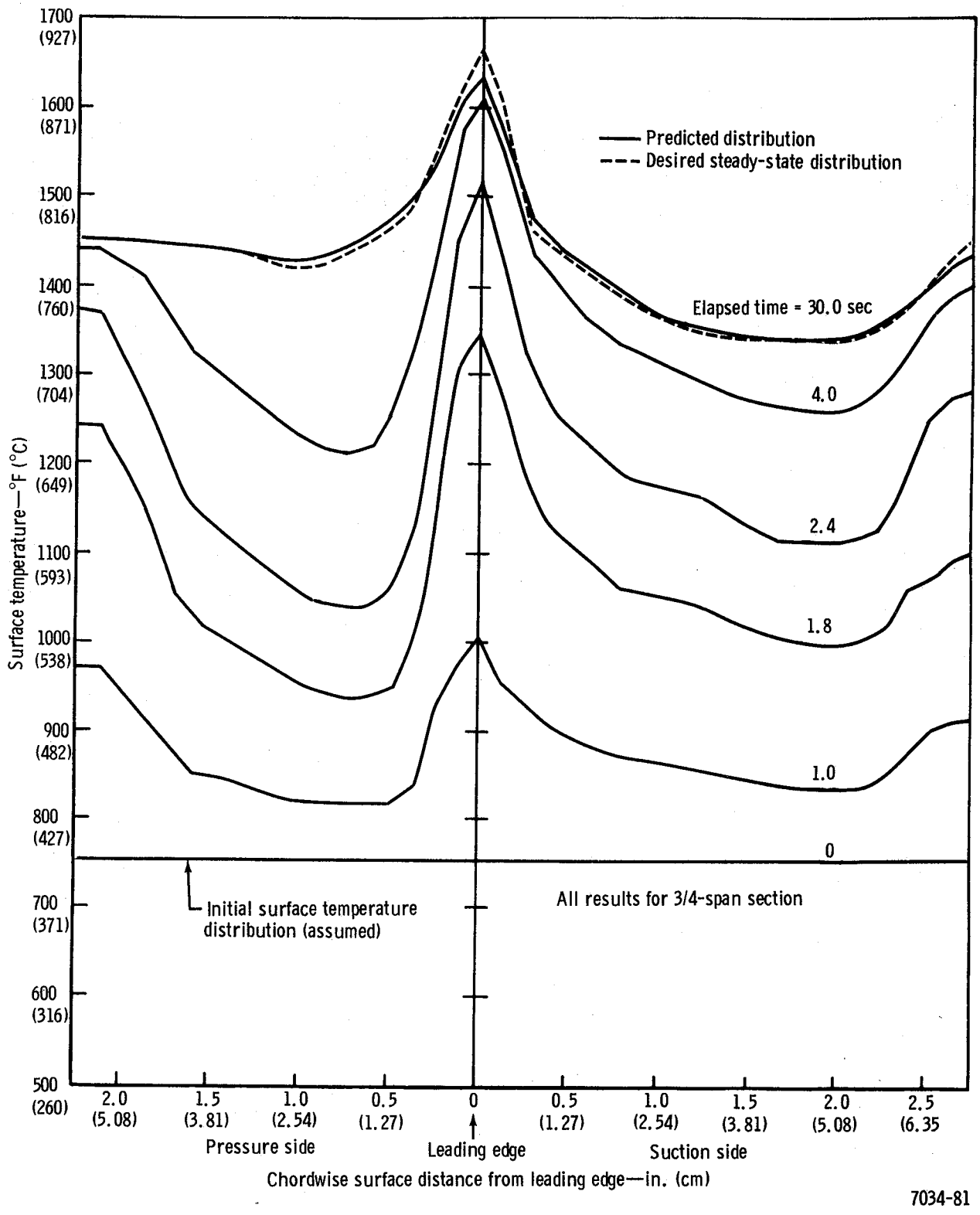

Figure 57. Predicted transient chordwise surface temperature for rapid increase in gas temperature (test vane No. 2).

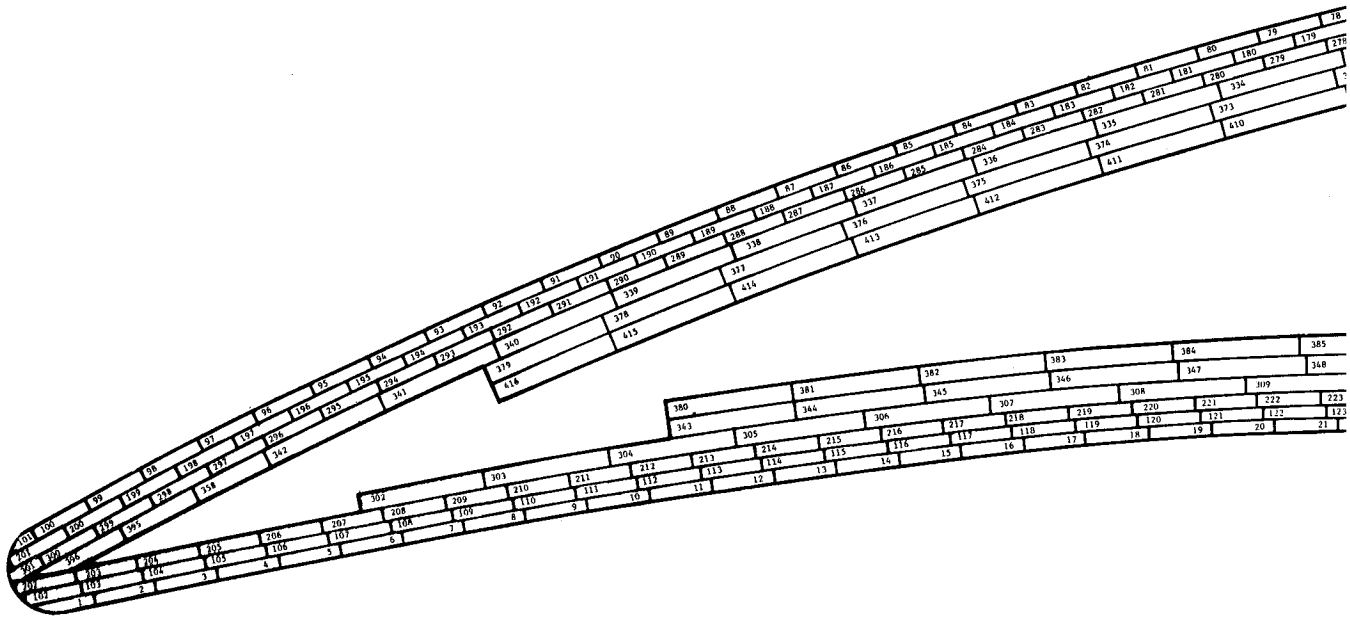

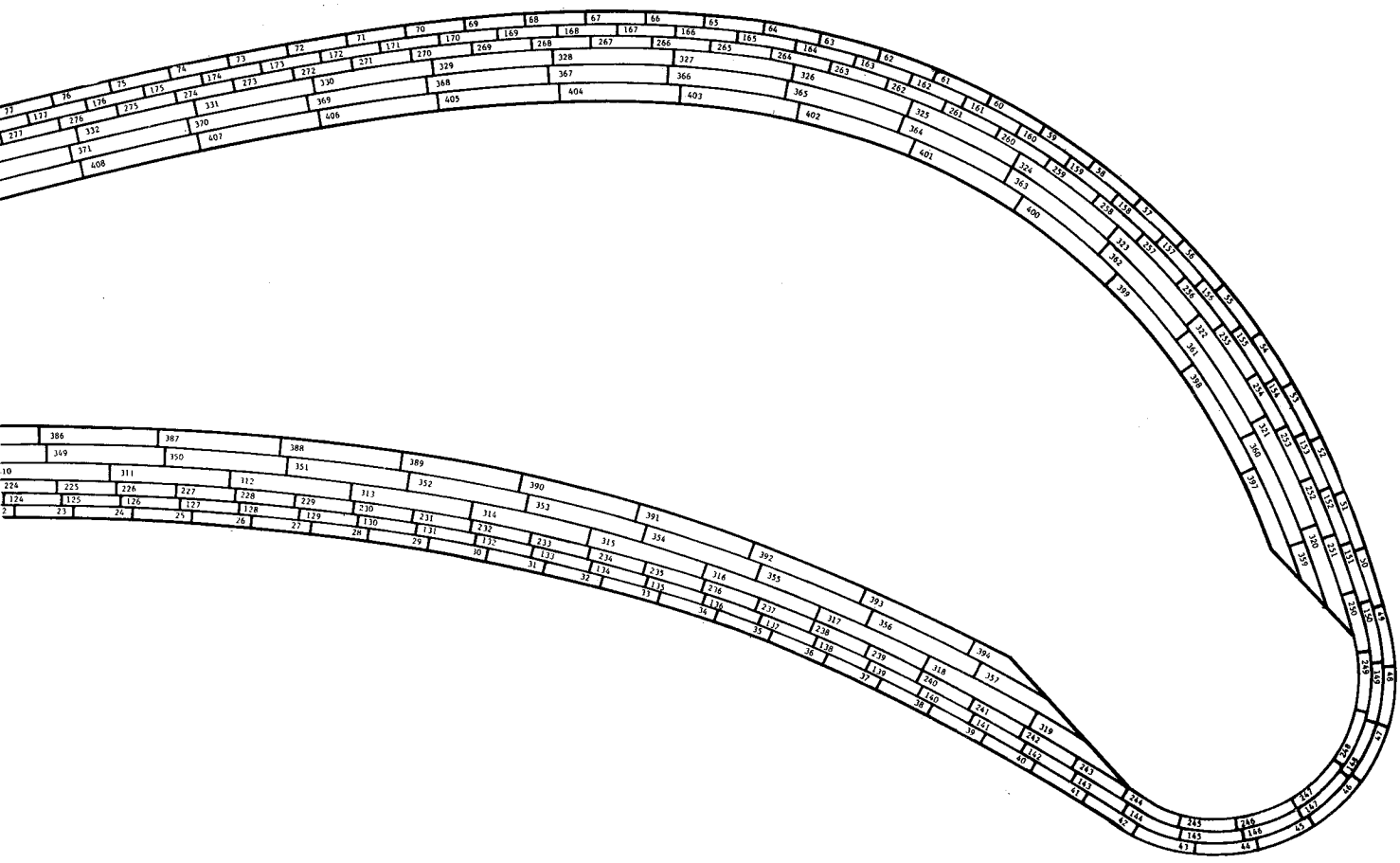

Figure 58. Modeling of airfoil cross section for computer program.

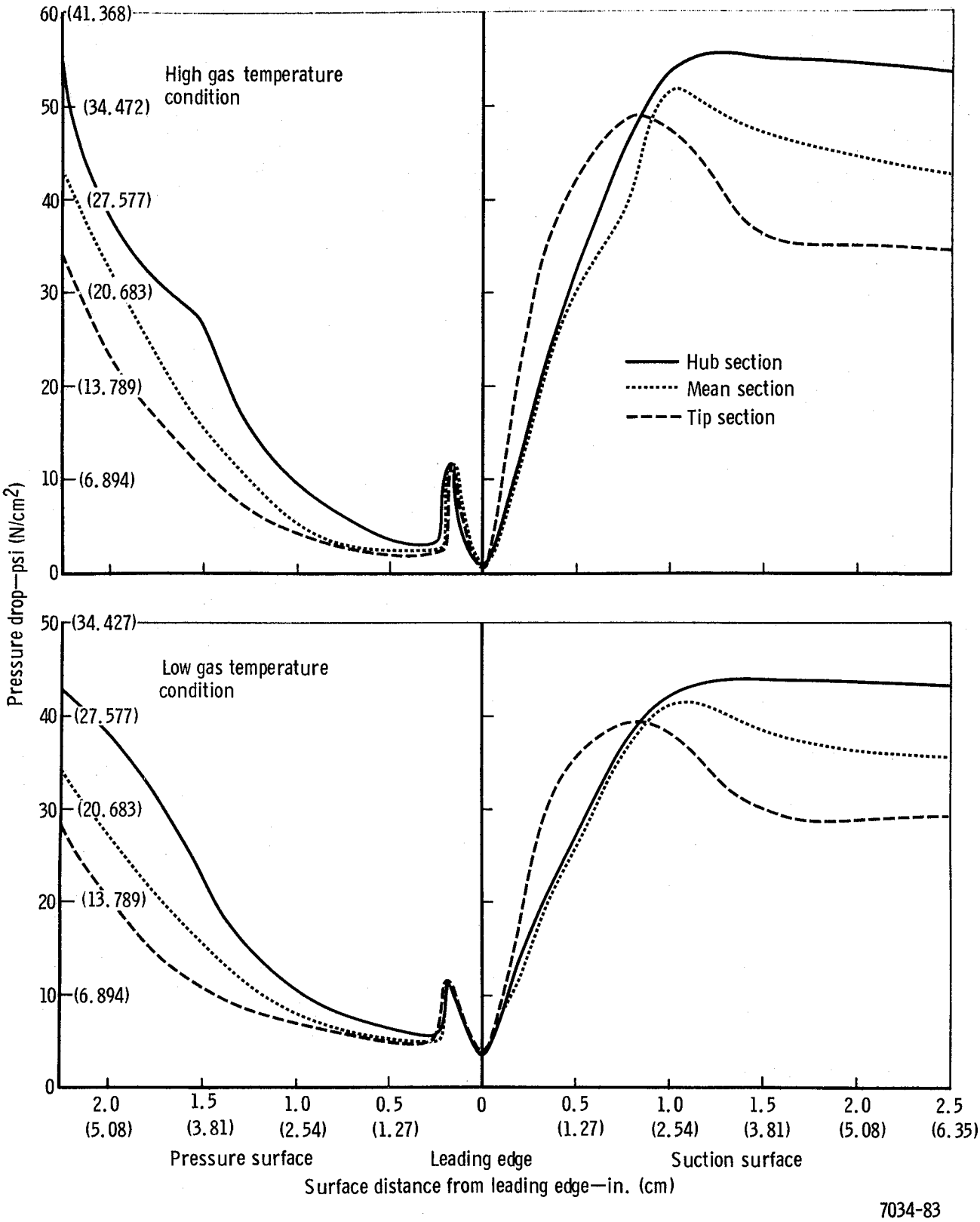

Figure 59. Pressure drop across airfoil wall at both thermal conditions.

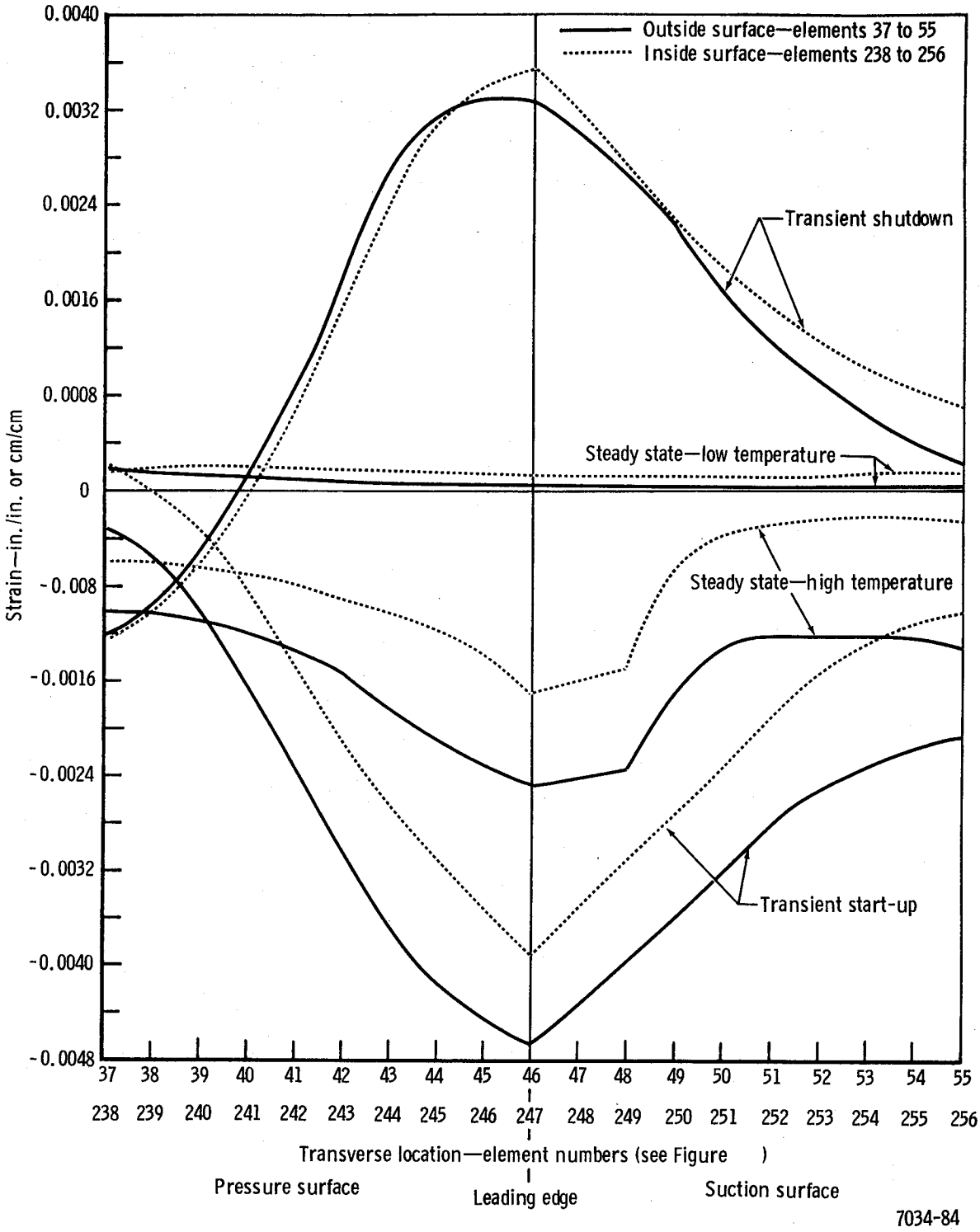

Figure 60. Total strain near leading edge for critical temperature distributions (strains are for cycle No. 5).

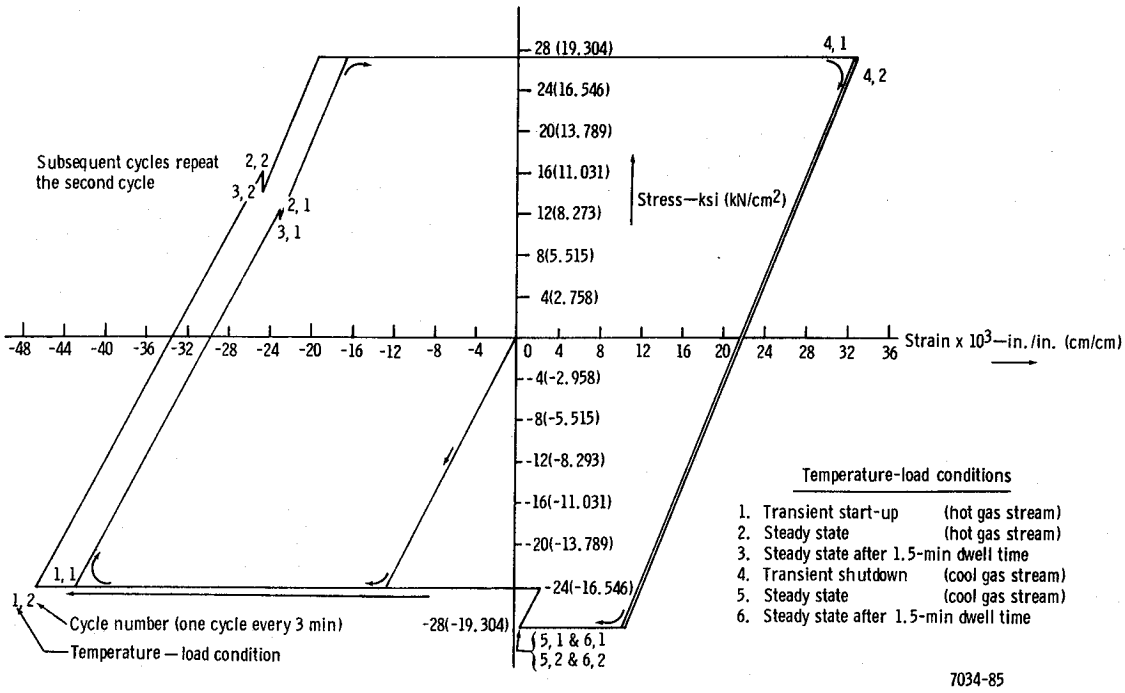

Figure 61. Stress-strain history of critical element at the leading edge.

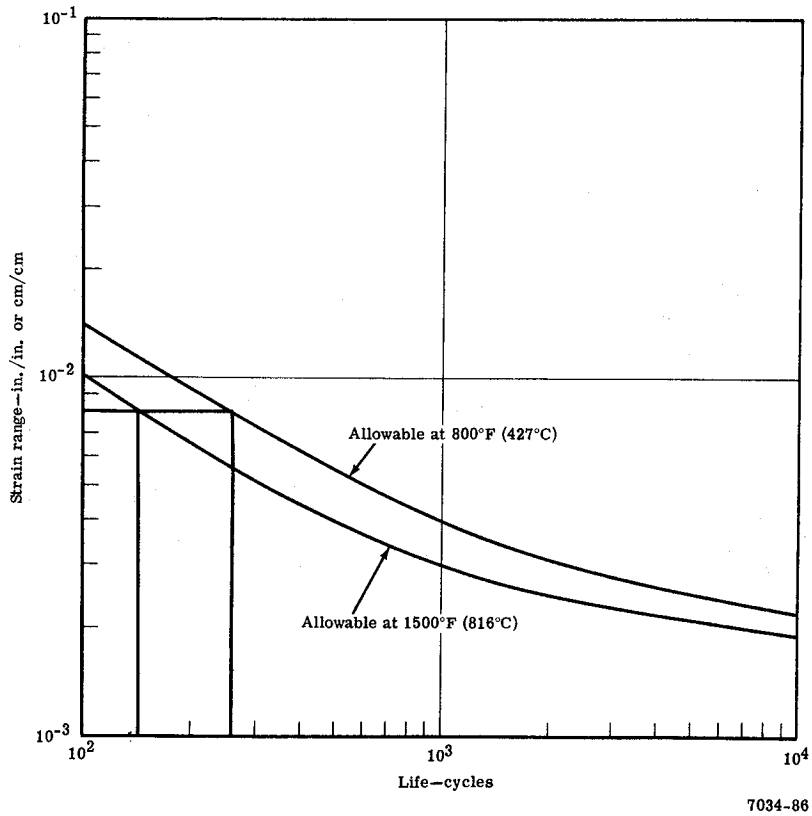

Figure 62. Strain range vs life (in 3-min cycles).

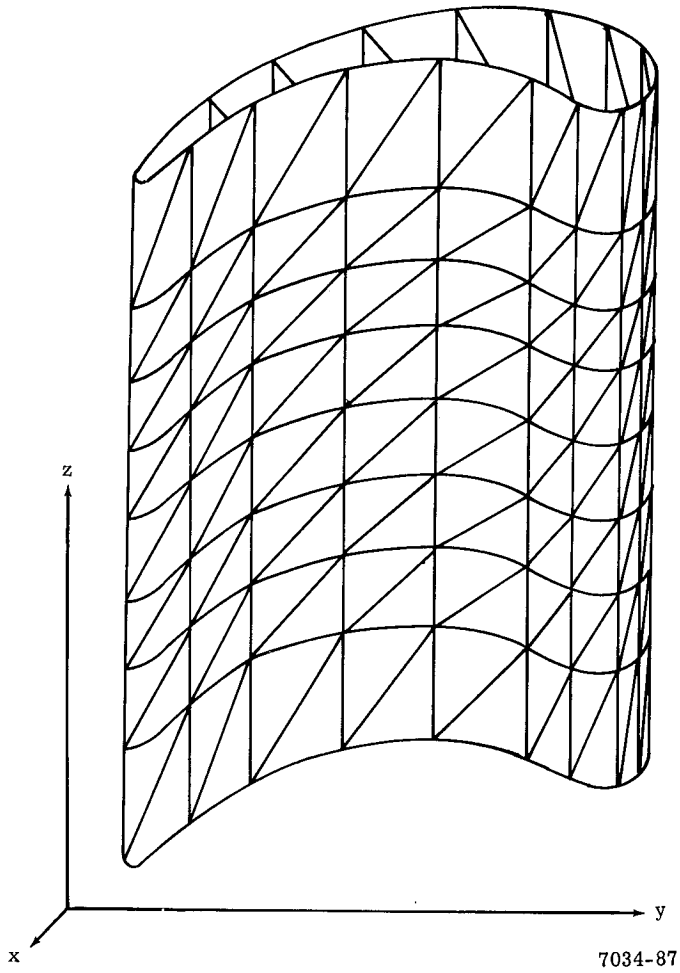

Figure 63. Modeling of airfoil for second computer program.

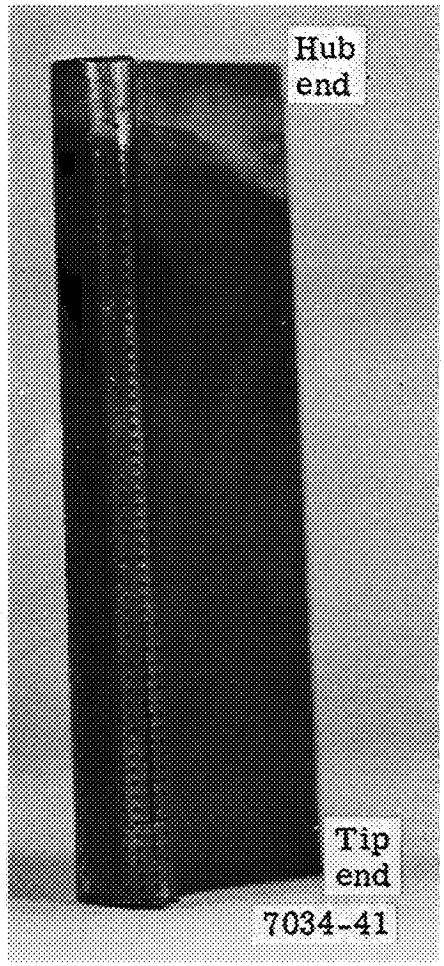

Figure 64. Leading edge of test vane No. 2 (magn: 1X).

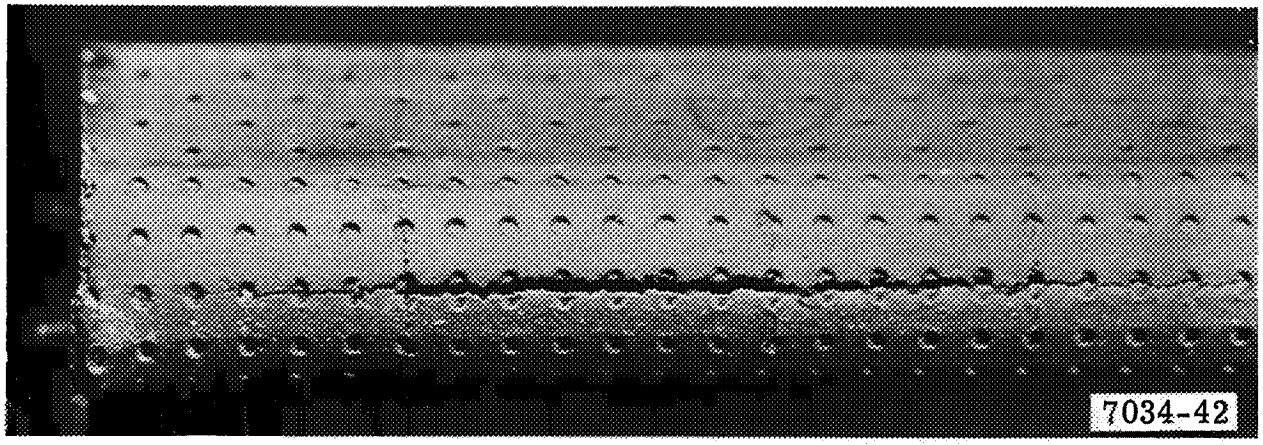

Figure 65. Photomacrograph of leading edge of test vane No. 2 (magn: 4X).

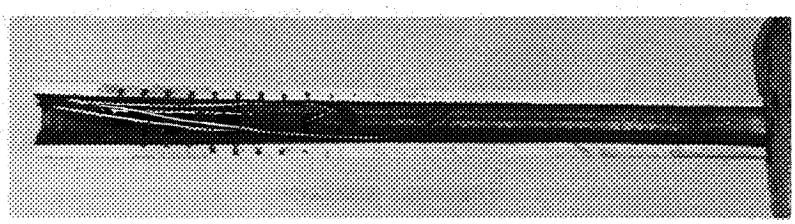

Magn: 1X

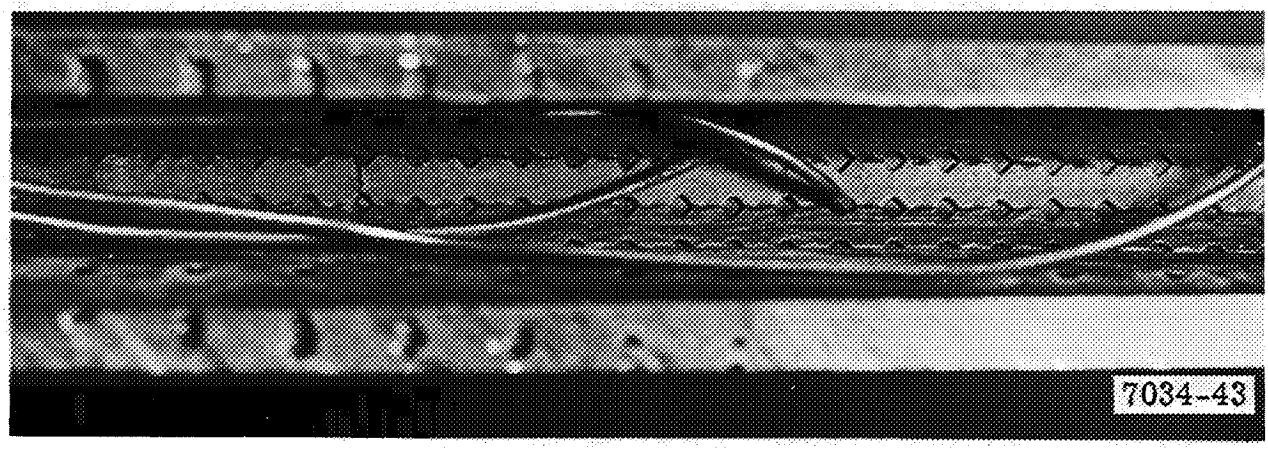

Magn: 4X

Figure 66. Photomacrograph of inside leading edge of test vane No. 2.

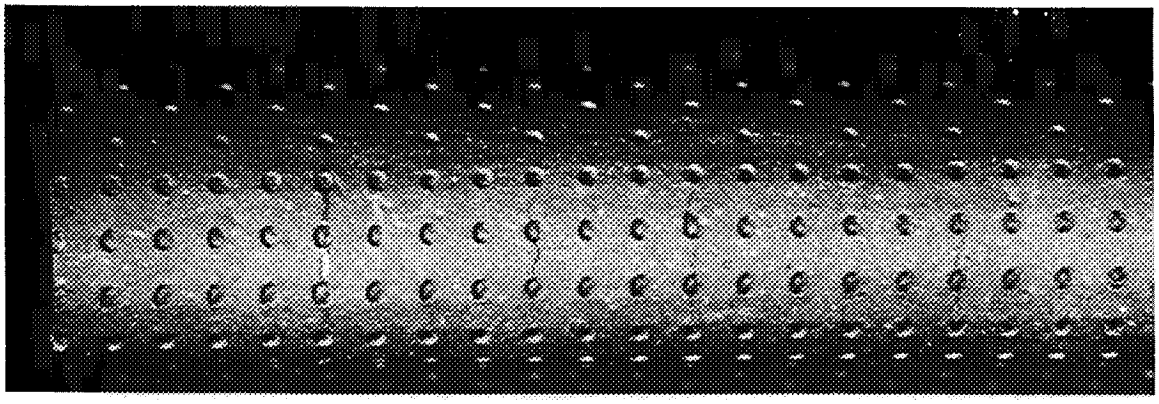

External surface

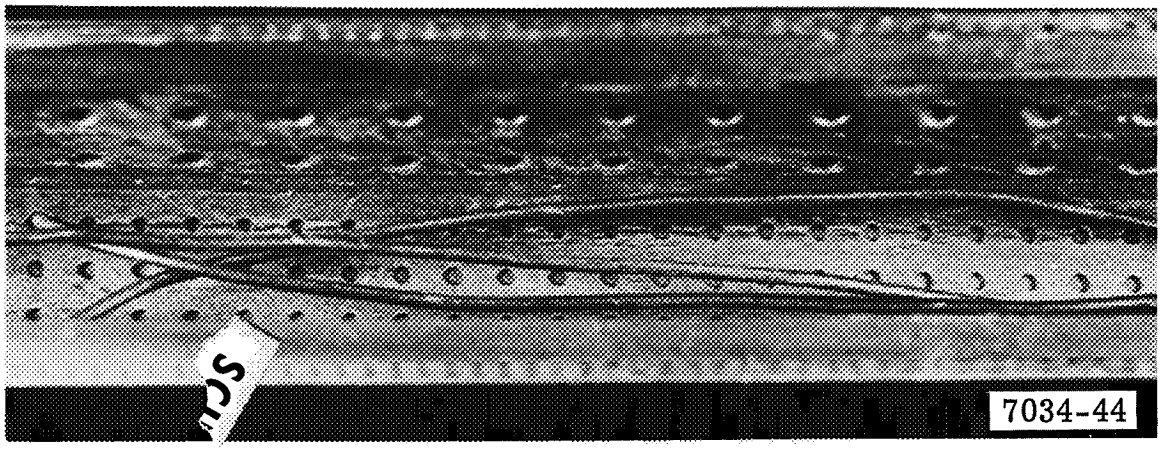

Internal surface

Figure 67. Photomacrographs of leading edge of test vane No. 3 (magn: 4X).

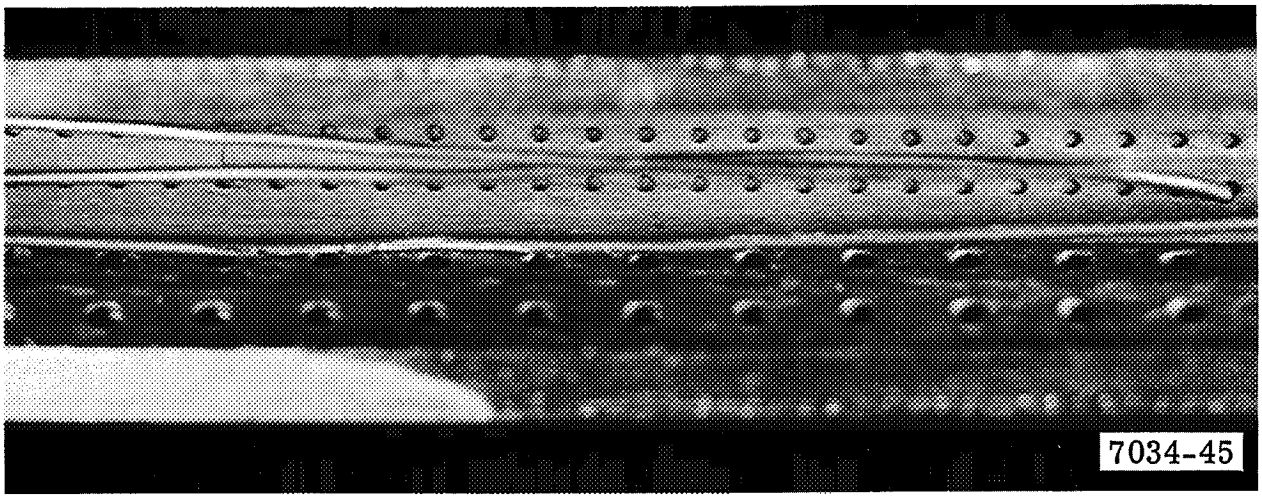

Figure 68. Photomacrograph of inside leading edge of test vane No. 4 (magn: 4X).

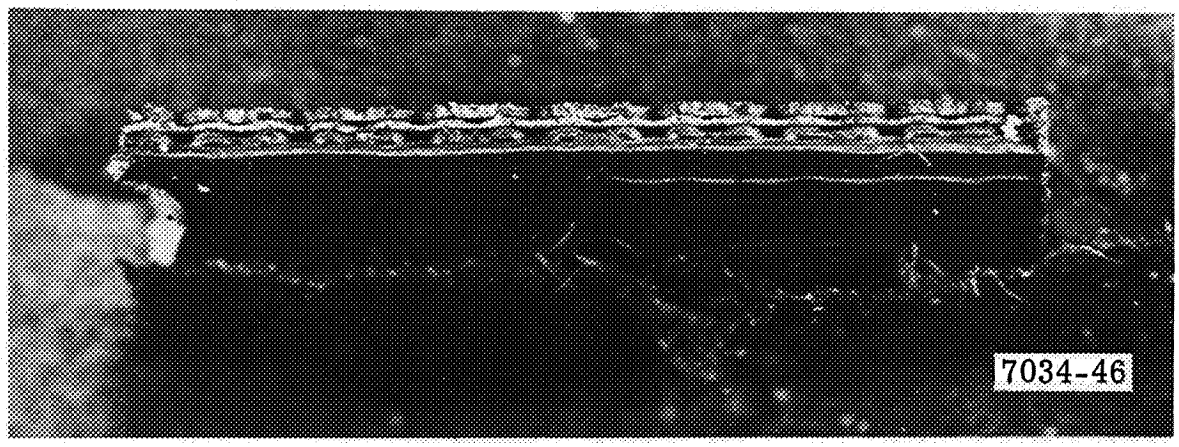

Internal surface

Figure 69. Photomacrograph of failure surfaces of test vane No. 2 (magn: 9X).

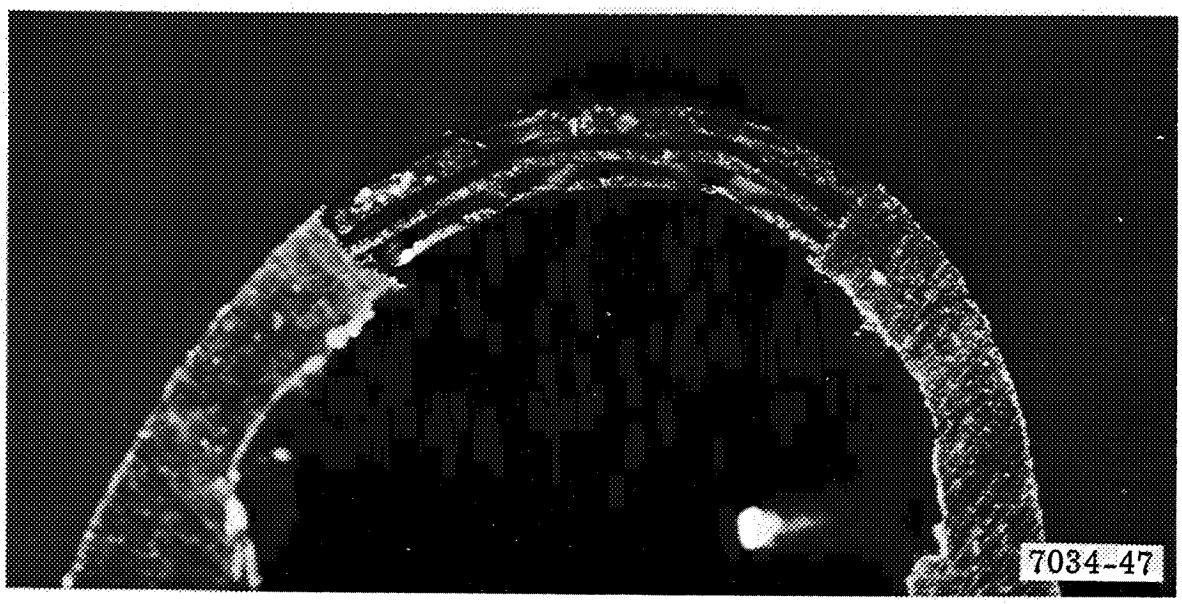

Figure 70. Photomacrograph of failure surfaces of test vane No. 3 (magn: 15X).

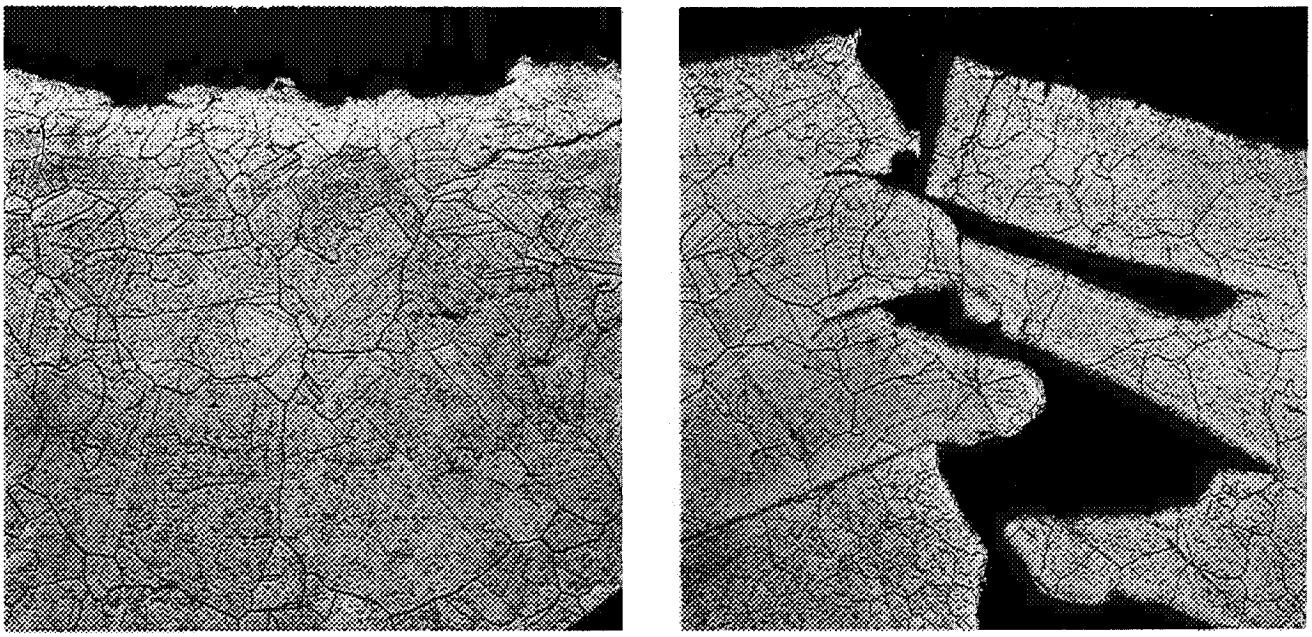

7034-48

Figure 71. Photomicrographs of longitudinal failure sections in test vane No. 2 (magn: 100X).

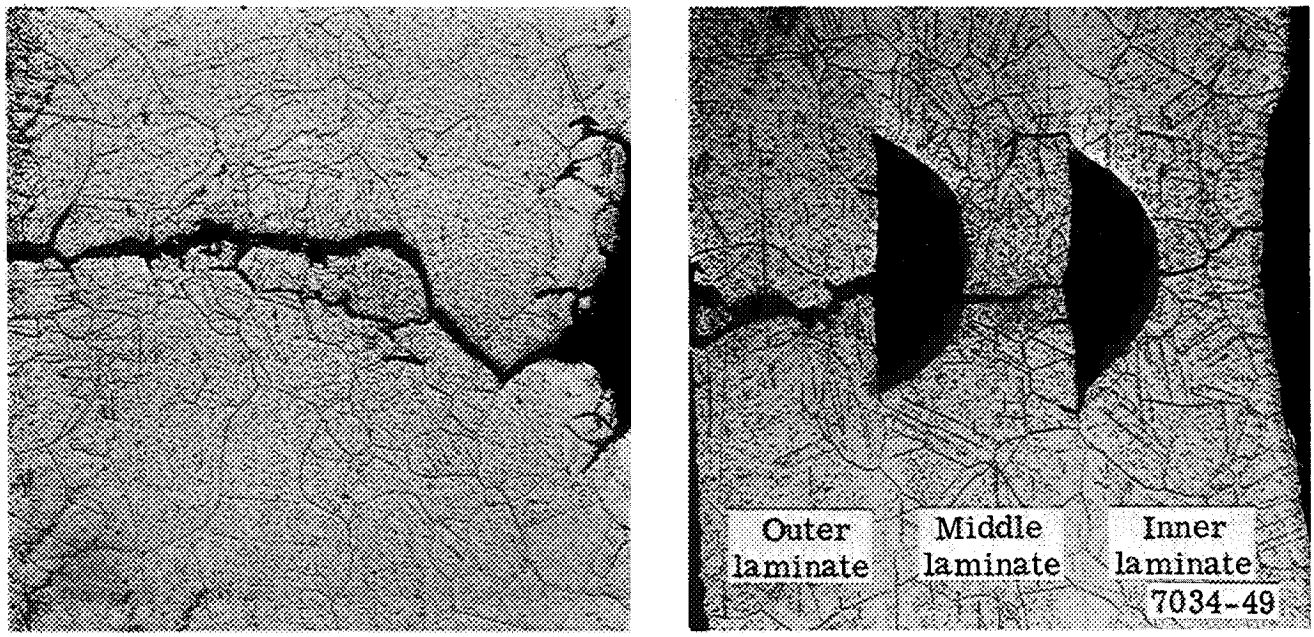

7034-49

Figure 72. Photomicrographs of transverse failure sections in test vanes No. 2 and 4 (magn: 100X).

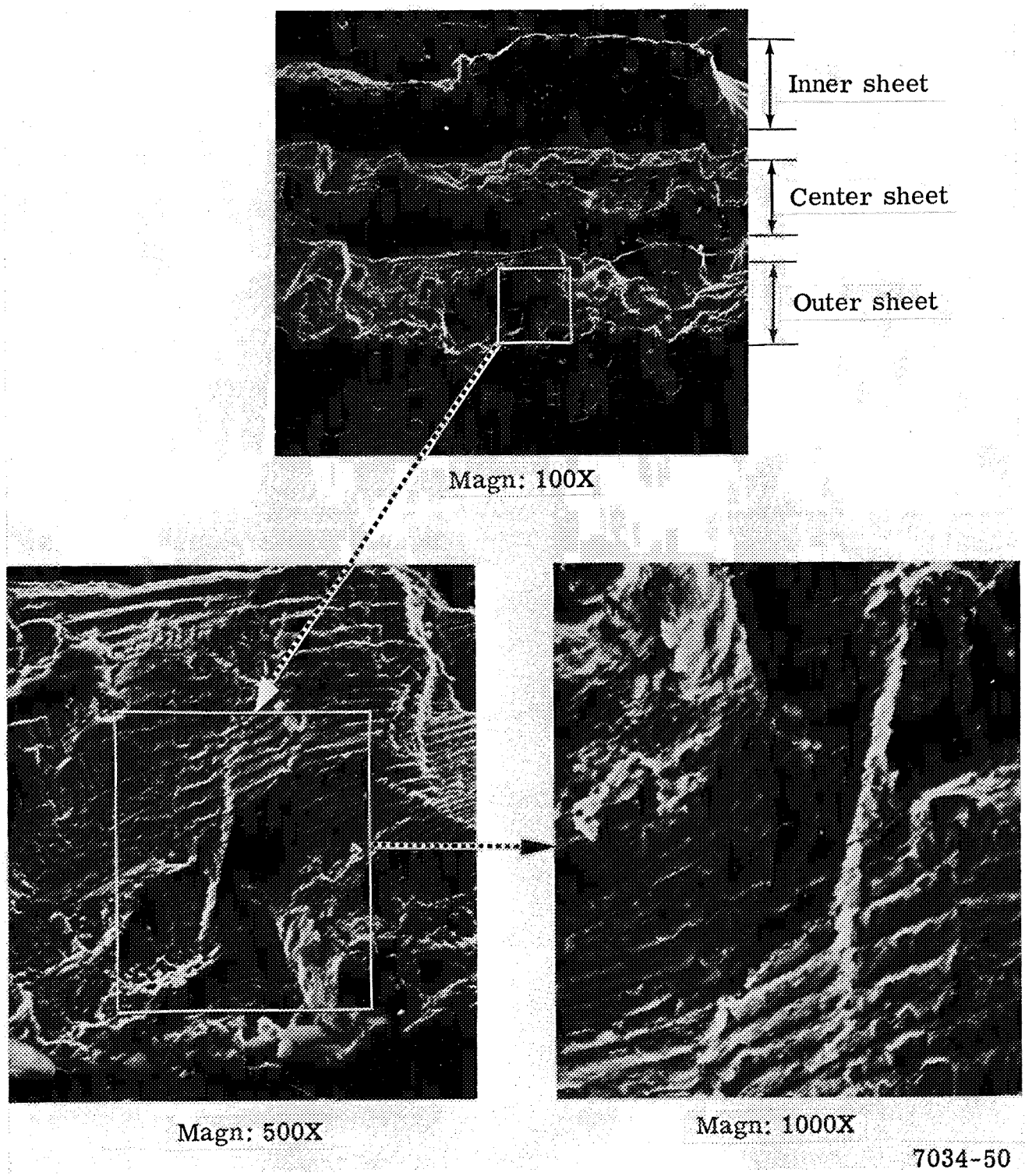

Figure 73. Electron scanning micrographs of longitudinal failure surfaces of test vane No. 2.

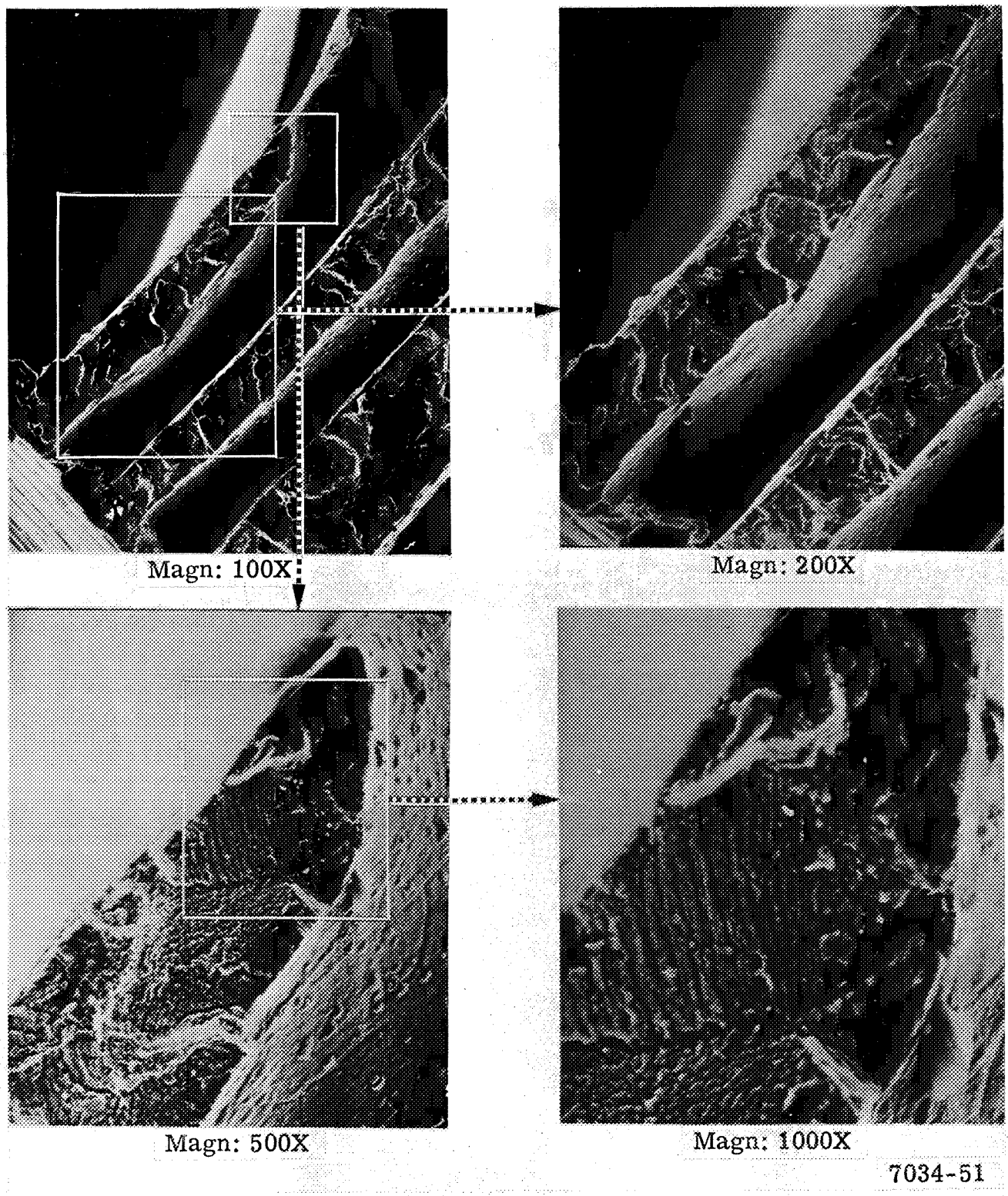

Figure 74. Electron scanning micrographs of transverse failure surfaces of test vane No. 3.

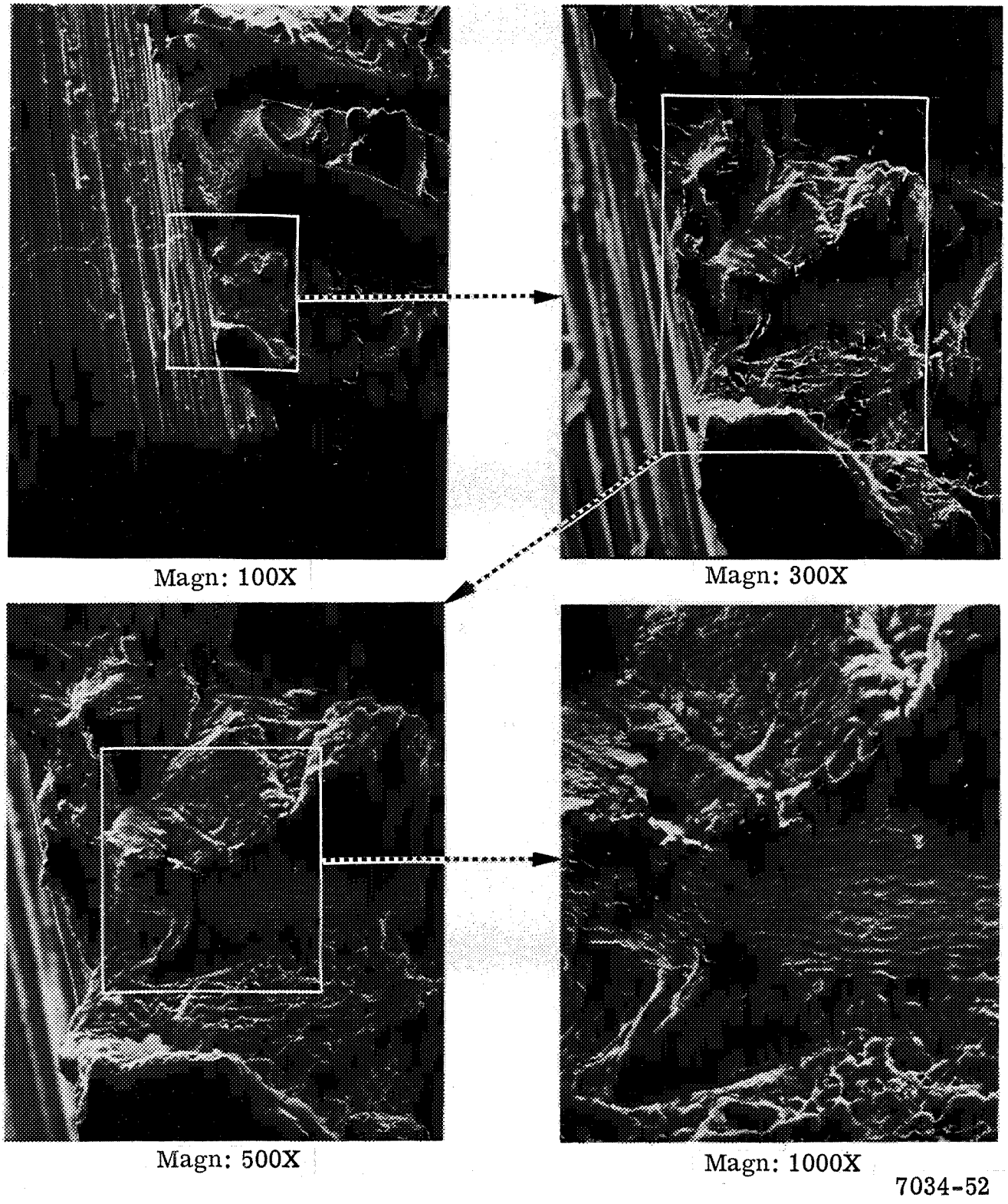

Figure 75. Scanning electron fractographs of transverse failure surfaces of test vane No. 4.

APPENDIX

DERIVATION OF ALLOWABLE STRAINS

The strain range/cyclic life relationships shown in Figure 62 were derived from experimental low cycle fatigue data for Lamilloy and sheet specimens fabricated from Hastelloy X. The relevant laboratory fatigue test data (fully reversed strain cycling) for "slant" and "normal" Lamilloy are shown in Figure 76. The distinction lies in the geometric arrangement of the surface holes which will produce either tangential surface injection ("slant" Lamilloy) or injection normal to the surface ("normal" Lamilloy).

The test data shown in Figure 76 could not be used directly in the vane life prediction analysis for several reasons:

- The hole spacing and diameter of the laboratory test specimens differed from those in the test vane (different stress concentration characteristics). These geometry differences are indicated in Table XIII.
- The frequency of loading the laboratory test specimens (5 cycles/min) differed from that in the cascade test (1 cycle every three minutes).
- Low cycle fatigue data for "normal" Lamilloy (representative of the cascade test vane) were not available at the desired 1500°F (816°C) temperature level.
- No low cycle fatigue data were available for Lamilloy at 800°F (427°C).

Consequently, the desired life curves (Figure 62) were established by making appropriate modifications to the available test data of Figure 76. The basis for modifying the test data is presented separately for the 1500°F (816°C) and 800°F (427°C) temperature levels in the following paragraphs.

TABLE XIII. DIFFERENCES BETWEEN LABORATORY TEST SPECIMENS AND CASCADE VANE.

	Laboratory test specimen	Cascade test vane
Hole spacing	0.096 in. (0.244 cm)	0.068 in. (0.173 cm)
Hole diameter	0.020 in. (0.051 cm)	0.023 in. (0.058 cm)
Geometric concentration factor (K_t)	2.38[12]	2.04[12]
Fatigue/stress concentration factor (K_f)	1.54*	1.41**
Frequency of loading	5 cycles/min	1 cycle/3 min

*K_f of 1.54 required to degrade 1500°F (816°C) solid sheet data in order to approximate Curve A, Figure 77.

**$K_f = (1.54-1)\frac{(2.04-1)}{(2.38-1)} + 1 = 1.41$

1500°F (816°C) FATIGUE LIFE PROJECTIONS

To establish the life of "normal" Lamilloy at 1500°F (816°C), the temperature level effect was first assumed to be the same for the two types of Lamilloy. Thus, the experimentally determined "normal" Lamilloy life at 1700°F (927°C) was increased by the ratio of "slant" Lamilloy life at 1500°F (816°C) to "slant" Lamilloy life at 1700°F (927°C) for any given strain level. This projection from experimental data then established the result shown as Curve A in Figure 77. With the projected "test data" for "normal" Lamilloy at 1500°F (816°C) thus established, additional corrections were made for differences in stress concentration (hole size and spacing differences) and in frequency of loading. The latter corrections had the net effect of shifting Curve A slightly to the right, producing Curve B in Figure 77.

Curve B was established with the aid of a computer program capable of modifying low cycle fatigue data to account for differences between laboratory test specimens and the specific component of interest (in this case, cascade test vane No. 2). In general, these differences can include size, surface finish, stress raisers, loading frequency, mean strain level, and material property scatter. To obtain the specific result desired here (Curve B, Figure 77), available experimental LCF data for a solid (unperforated) sheet at 1500°F (816°C) was first "degraded" until a good approximation of Curve A in Figure 77 was obtained. More specifically, the approximation to Curve A (hereafter referred to as Curve A' but not shown) was obtained by applying a lumped concentration factor of 1.54 to the 1500°F (816°C) solid sheet data. The same computer program was then used to correct Curve A' to account for the geometry and loading frequency differences which existed between the test specimens (approximated by Curve A') and the actual test vane. These differences, summarized in Table XIII, resulted in a predicted shift in Curve A' (to the right). The percentage shift in Curve A' at each strain level was then assumed to apply equally to Curve A which, when corrected, was plotted as the upper curve (Curve B) in Figure 77. Curve B is identical with the 1500°F (816°C) result shown in Figure 62.

800°F (427°C) FATIGUE LIFE PROJECTIONS

To obtain a life curve for 800°F (427°C) where no low cycle fatigue data were available, the Method of Universal Slopes was used. Initially, Curves 1 and 2 in Figure 78 were constructed based on the following conditions:

	1500°F (816°C)	800°F (427°C)
Tensile strength*	51 ksi (35.2 kN/cm^2)	76.8 ksi (53.0 kN/cm^2)
Modulus of elasticity*	22,370 ksi (15,423 kN/cm^2)	24,445 ksi (16,853 kN/cm^2)
Reduction in area (%)	45	58.8

$K_f = q (K_t - 1) + 1 = 1.42$

$K_t = 2.04$

$q = 0.4$ (notch sensitivity factor)[12]

A degradation of 20% in strength was assumed for the surface finish.

*Source: DDAD Materials Engineering Department.

However, comparison of Curve 1 with the results shown in Figure 77 reveals that the Universal Slopes prediction is very optimistic relative to the projected experimental trends (Curve B). Consequently, to construct an 800°F (427°C) curve which is consistent with the 1500°F (816°C) result previously established (Curve B), Curve 1 was degraded until it coincided with Curve B at 1000 cycles, producing Curve 1'. The same degradation factor was applied to Curve 2, producing Curve 2'. The final 800°F (427°C) S-N curve was then constructed by assuming that it coincides with Curve 2' at 1000 cycles and differs from it elsewhere by the same percentage that Curve B differs from Curve 1'. The final result is shown as Curve C, which is identical with the 800°F (427°C) curve in Figure 62.

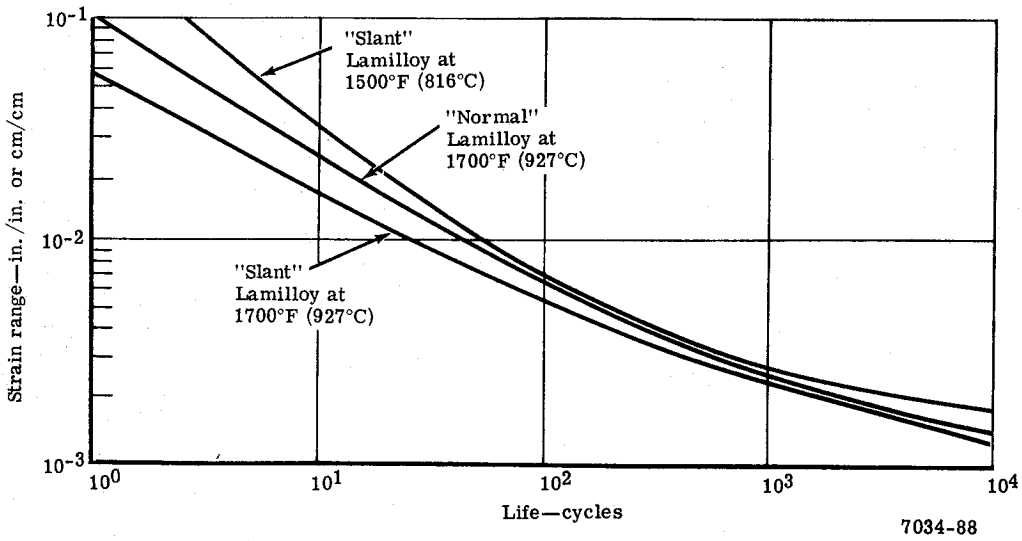

Figure 76. Experimental low cycle fatigue data for Lamilloy specimens.

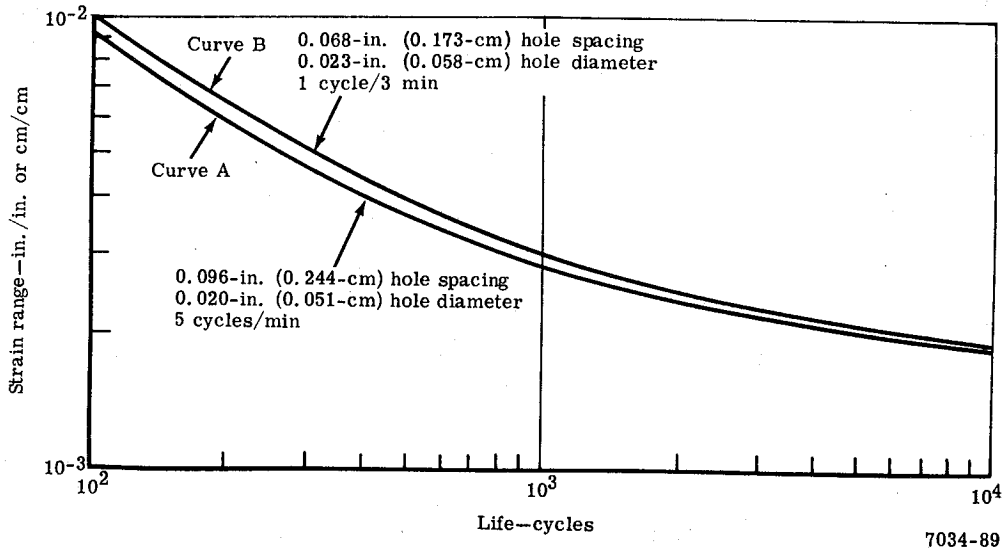

Figure 77. Projected low cycle fatigue life curves for 1500°F (816°C).

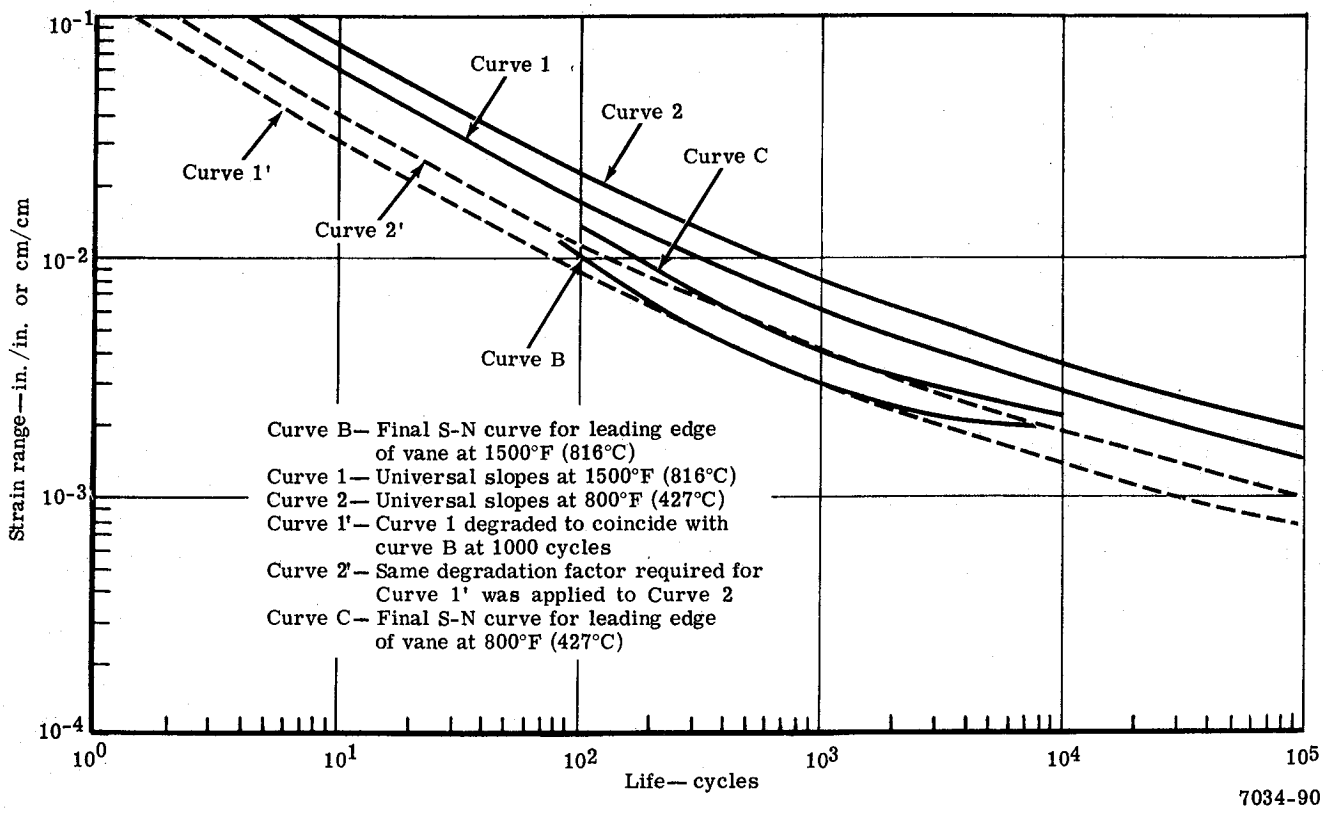

Figure 78. Projected low cycle fatigue life for 1500 and 800°F (816 and 427°C).

DISTRIBUTION LIST

	ADDRESSEE		NO. OF COPIES
1.	NASA-Lewis Research Center 21000 Brookpark Road Cleveland, Ohio 44135		
	Attention: Report Control Office	MS 5-5	1
	Technology Utilization Office	MS 3-19	1
	Library	MS 60-3	2
	Fluid System Components Div.	MS 5-3	1
	W. L. Stewart	MS 77-2	1
	J. Howard Childs	MS 60-4	1
	L. W. Schopen	MS 77-3	1
	Dr. E. L. Warren	MS 60-6	15
	J. B. Esgar	MS 60-5	1
	R. H. Kemp	MS 49-1	1
	F. S. Stepka	MS 60-6	1
	R. O. Hickel	MS 60-6	1
	Dr. D. Spera	MS 49-1	1
	H. H. Ellerbrock	MS 60-4	1
	L. E. Macioce	MS 60-6	1
	Dr. J. Livingood	MS 60-6	1
	J. Lucas	MS 6-1	1
	Dr. B. Lubarsky	MS 3-3	1
2.	NASA Scientific & Technical Information Facility P. O. Box 33 College Park, Maryland 20740 Attention: NASA Representative RQT-2448		6
3.	Department of the Army U.S. Army Aviation Material Laboratory Fort Eustis, Virginia 23604 Attention: John White		1
4.	NASA Headquarters 600 Independence Avenue, S.W. Washington, D. C. 20546 Attention: N. F. Rekos (RLC)		1
5.	Stellite Division Cabot Corporation 1020 West Park Avenue Kokomo, Indiana 46901 Attention: Miss D. E. Kirtley		1

DISTRIBUTION LIST (Cont.)

	ADDRESSEE	NO. OF COPIES
6.	Wright-Patterson AFB, Ohio 45433 Attention: Mr. J. Richens AFAPL (APTC) Dr. A. Wennerstrom (ARF)	 1 1
7.	Air Force Office of Scientific Research Propulsion Research Division USAF Washington, D.C. 20025	1
8.	Department of the Navy Bureau of Naval Weapons Washington D.C. 20025 Attention: Robert Brown, RAPP14	1
9.	Department of the Navy Bureau of Ships Washington, D.C. 20360 Attention: G. L. Graves	1
10.	NASA-Langley Research Center Langley Station Technical Library Hampton, Virginia 23365 Attention: Mark R. Nichols John V. Becker	 1 1
11.	United Aircraft Corporation Pratt & Whitney Aircraft Division Florida Research & Development Center P. O. Box 2691 West Palm Beach, Florida 33402 Attention: R. A. Schmidtke	 1
12	United Aircraft Library, UAC Research Bldg. 400 Main Street East Hartford, Connecticut 06108 Attention: G. Andreini John Goncar	 2 2
13.	Northern Research & Engineering Corporation 219 Vassar Street Cambridge, Massachusetts 02139 Attention: K. Ginwala	 1

DISTRIBUTION LIST (Cont.)

	ADDRESSEE	NO. OF COPIES
14.	General Electric Company - Flight Propulsion Division 930-1000 Western Avenue West Lynn, Massachusetts 01905 Attention: Dr. C. W. Smith - Library Bldg. 2-40M	1
15.	Curtiss-Wright Corporation Wright Aeronautical Division Wood-Ridge, New Jersey 07075 Attention: S. Lombardo	1
16.	Air Research Manufacturing Company The Garrett Corporation, Arizona Division 402 South 36th Street Phoenix, Arizona 85934 Attention: Robert O. Bullock	1
17.	Air Research Manufacturing Company The Garrett Corporation 9851 Sepulveda Boulevard Los Angeles, California 90009 Attention: Mr. R. D. Mueller	1
18.	AVCO Corporation Lycoming Division 550 South Main Street Stratford, Connecticut 06497 Attention: C. W. Bolton Charles Kuintzle	1 1
19.	Continental Aviation & Engineering Corporation 12700 Kercheval Avenue Detroit, Michigan 48215 Attention: Eli H. Benstein Howard C. Welch	1 1
20.	International Harvester Company, Solar 2200 Pacific Highway San Diego, California 92112 Attention: P. A. Pitt Mrs. L. Walper	1 1

DISTRIBUTION LIST (Cont.)

	ADDRESSEE	NO. OF COPIES
21.	Goodyear Atomic Corporation Box 268 Piketon, Ohio 45661 Attention: Department No. 423 for: C. O. Longebrake	1
22.	George Deriderian AIR 53622 B Department of Navy Bureau of Navy Washington, D. C. 20360	1
23.	The Boeing Company Commercial Airplane Division P. O. Box 3707 Seattle, Washington 98124 Attention: G. J. Schott MS 80-66	1
24.	The Boeing Company Missile and Information Systems Division 224 N. Wilkinson Street Dayton, Ohio 45402 Attention: Warren K. Thorson	1
25.	Wall Colmonoy Corporation 19345 John R. Street Detroit, Michigan 48233 Atteniton: R. L. Peaslee	1
26.	The Bendix Corporation Research Laboratories Division 20900 - 10-1/2 Mile Road Southfield, Michigan 48076 Attention: A. R. Spencer	1
27.	Battelle Memorial Institute 505 King Avenue Columbus, Ohio 43201 Attention: Defense Metals Information Center Robert T. Niehoff	1

DISTRIBUTION LIST (Cont.)

	ADDRESSEE	NO. OF COPIES
28.	Bendix Filter Division 434 West 12 Mile Road Madison Heights, Michigan 48071 Attention: J. Padden	1
29.	Air Force Materials Laboratory Wright-Patterson Air Force Base, Ohio 45433 Attention: MAAM, Mr. Hughes MAMP, Mr. Hendricks	1 1
30.	Douglas Aircraft Company 3855 Lakewood Blvd. Long Beach, California 90801 Attention: Technical Information Center, CL-250 For J. E. Merriman	1
31.	General Motors Corporation Detroit Diesel Allison Division P. O. Box 894 Indianapolis, Indiana 46206 Attention: G. E. Holbrook J. N. Barney H. E. Helms Library	1 1 1
32.	Engineering Library TRW Inc. 23555 Euclid Avenue Cleveland, Ohio 44117 Attention: Elizabeth Barrett, Librarian J. Edward Taylor, Director Product Development Jet and Ordnance Division	1 1
33.	Westinghouse Electric Corporation Small Steam and Gas Turbine Engineering B-4 Lester Branch P. O. Box 9175 Philadelphia, Pennsylvania 19113 Attention: S. M. DeCorso J. J. Watt	1 1
34.	General Electric Company Flight Propulsion Division Cincinnati, Ohio 45215 Attention: Technical Information Center N/32 Jack W. Clark M-78	1 1